ABSTRACT

ELECTRONIC, THERMOELECTRIC AND OPTICAL PROPERTIES OF VANADIUM OXIDES: VO_2, V_2O_3 AND V_2O_5

by
Chiranjivi Lamsal

Correlated electrons in vanadium oxides are responsible for their extreme sensitivity to external stimuli such as pressure, temperature or doping. As a result, several vanadium oxides undergo insulator-to-metal phase transition (IMT) accompanied by structural change. Unlike vanadium pentoxide (V_2O_5), vanadium dioxide (VO_2) and vanadium sesquioxide (V_2O_3) show IMT in their bulk phases. In this study, we have performed one electron Kohn-Sham electronic band-structure calculations of VO_2, V_2O_3 and V_2O_5 in both metallic and insulating phases, implementing a full ab-initio simulation package based on Density Functional Theory (DFT), Plane Waves and Pseudopotentials (PPs). Electronic band structures are found to be influenced by crystal structure, crystal field splitting and strong hybridization between O2p and V3d bands. “Intermediate bands”, with narrow band widths, lying just below the higher conduction bands, are observed in V_2O_5 which play a critical role in optical and thermoelectric processes. Similar calculations are performed for both metallic and insulating phases of bulk VO_2 and V_2O_3. Unlike in the metallic phase, bands corresponding to “valence electrons” considered in the PPs are found to be fully occupied in the insulating phases.

Transport parameters such as Seebeck coefficient, electrical conductivity and thermal (electronic) conductivity are studied as a function of temperature at a fixed value of chemical potential close to the Fermi energy using Kohn-Sham band structure approach coupled with Boltzmann transport equations. Because of the layered structure

and stability, only V_2O_5 shows significant thermoelectric properties. All the transport parameters have correctly depicted the highly anisotropic electrical conduction in V_2O_5. Maxima and crossovers are also seen in the temperature dependent variation of Seebeck coefficient in V_2O_5, which can be consequences of "specific details" of the band structure and anisotropic electron-phonon interactions. For understanding the influence of phase transition on transport properties, we have also studied transport parameters of VO_2 for both metallic and insulating phases. The Seebeck coefficient, at experimental critical temperature of 340K, is found to change by 18.9 μV/K during IMT, which lies within 10% of the observed discontinuity of 17.3 μV/K.

Numerical methods have been used to analyze the optical properties of bulk and thin films of VO_2, V_2O_3, and V_2O_5, deposited on Al_2O_3 substrates, from infrared to vacuum ultraviolet range (up to 12 eV). The energies corresponding to the peaks in the reflectivity-energy (R-E) spectra are explained in terms of the Penn gap and the degree of anisotropy is found to be in the order of $V_2O_3 < VO_2 < V_2O_5$. The effective number of electrons participating in the optical transitions is described using the "sum rule". The optical absorption is found to occur followed by the transitions of d electrons as well as the transitions from O2p to V3d states.

In the Honeywell microbolometer structure, the bolometer sensing element has been chosen to be VO_x, with x equal to 1.8, along with other layers of Si_3N_4, air, Al and Si. The room temperature spectral emissivity of such a layered structure is analyzed using Multi-Rad, a simulation package that utilizes thin film optics in the form of matrix method of multilayers. Calculations show that the Si_3N_4 layer provides the much desired linear performance of the VO_x based bolometer.

ELECTRONIC, THERMOELECTRIC AND OPTICAL PROPERTIES OF VANADIUM OXIDES: VO_2, V_2O_3 AND V_2O_5

by
Chiranjivi Lamsal

A Dissertation
Submitted to the Faculty of
New Jersey Institute of Technology and Rutgers the State University of New Jersey
in Partial Fulfillment of the Requirements for the Degree of
Doctor of Philosophy in Applied Physics

Federated Department of Physics

January 2015

.

APPROVAL PAGE

ELECTRONIC, THERMOELECTRIC AND OPTICAL PROPERTIES OF VANADIUM OXIDES: VO_2, V_2O_3 AND V_2O_5

Chiranjivi Lamsal

Dr. N. M. Ravindra, Dissertation Advisor — Date
Professor of Physics and Director of Materials Science and Engineering Program, NJIT

Dr. Anthony Fiory, Committee Member — Date
Consultant (Former Research Professor of Physics), NJIT

Dr. Cristiano Dias, Committee Member — Date
Assistant Professor of Physics, NJIT

Dr. Keun Hyuk Ahn, Committee Member — Date
Associate Professor of Physics, NJIT

Dr. Martin Schaden, Committee Member — Date
Associate Professor of Physics, Rutgers–Newark

BIOGRAPHICAL SKETCH

Author: Chiranjivi Lamsal

Degree: Doctor of Philosophy

Date: January 2015

Undergraduate and Graduate Education:

- Doctor of Philosophy in Applied Physics,
  New Jersey Institute of Technology and Rutgers the State University of New Jersey, Newark, NJ, 2015

- Master of Science in Physics,
  Southern Illinois University, Carbondale, IL, 2010

- Master of Science in Physics,
  Tribhuvan University, Kathmandu, Nepal, 2002

Major: Applied Physics

Publications and Presentations:

Lamsal, C., Ravindra, N.M. (2013). Optical Properties of Vanadium Oxides-An Analysis. *Journal of Materials Science, 48,* 6341-6351.

Lamsal, C., Ravindra, N.M. (2014). Simulation of Spectral Emissivity of Vanadium Oxides (VO_x)-Based Microbolometer Structures. *Emerging Materials Research, 3,* 194-202.

Lamsal, C., Mishra, D.R. & Ravindra, N.M. (2014). Equilibrium Configuration of $(H_2O)_n$, for n = 1-3. *Nanomaterials and Energy, 3,* 129-138.

Lamsal, C., Ravindra, N.M. (2014). Ab Initio Calculations of Thermoelectric Properties and Structures of Vanadium Oxides. A manuscript under preparation.

Lamsal, C., Ravindra, N.M. (2014). Vanadium Oxides for Energy and Security Applications. In: Dwivedi, Y., Rai S.B. & Singh, J.P. (Eds.), *Spectroscopic Techniques for Security, Forensic and Environmental Applications,* pages 195-220. Hauppauge, New York: Nova Science Publishers.

Lamsal, C., Chen, D. & Ravindra, N.M. (2012). Optical and Electronic Properties of AlN, GaN and InN: An Analysis. *Supplemental Proceedings: Materials Processing and Interfaces, 1,* 701-713. Hoboken, New Jersey: John Wiley & Sons, Inc.

Lamsal, C., Ravindra, N.M. (October 2014). Thermoelectric Properties of Vanadium Oxides. Pittsburg, PA: Materials Science & Technology.

Lamsal, C., Ravindra, N.M. (February 2014). Optical, Electrical and Electronic Properties of Vanadium Oxides – An Analysis. San Diego, CA: TMS Annual Meeting & Exhibition.

Lamsal, C., Ravindra, N.M. (October 2013). Optical and Electrical Properties of Vanadium Oxides – An Analysis. Montréal, Canada: Materials Science & Technology.

Leuty, G., Lamsal, C., Nehring, J. & Tsige, M. (March 2009). Temperature Dependent Adsorption Dynamics of Binary Mixtures of Halomethanes on Graphite and α-Quartz Surfaces. Pittsburgh, PA: APS March meeting.

Lamsal, C., Leuty, G., Nehring, J. & Tsige, M. (March 2009). Halomethane Adsorption on Graphite and Silica Surfaces. Pittsburgh, PA: APS March meeting.

Lamsal, C., Leuty, G. & Tsige, M. (May 2009). Adsorption of Binary Mixtures of Halomethanes on Solid Substrates. Carbondale, IL: 41st Midwest Theoretical Chemistry Conference (MWTCC).

Dedicated to my Parents:

Hem Kant Lamsal and Moti Devi Lamsal

ACKNOWLEDGMENTS

I would like to express my sincere gratitude to Dr. N. M. Ravindra, as an advisor, for his invaluable insights, guidance, support and inspiration during the entire course of this research. His encouragement at all times has been of immense value. Besides the role of an advisor, he has played a very crucial role of guardianship since the beginning of this research without which my research would not take this form and size.

I am very thankful to Dr. Anthony Fiory, Dr. Cristiano Dias, Dr. Keun Hyuk Ahn of New Jersey Institute of Technology (NJIT) and Dr. Martin Schaden of Rutgers–Newark for serving as members in my dissertation committee and providing me with suggestions and comments after reading the manuscript thoroughly.

I am especially thankful to Dr. Fadi Deek, Provost and Senior Executive Vice President of NJIT, whose arrangement for financial support, follow-up and encouragement remained as a backbone and led me to the writing of this thesis. He will remain associated with my PhD degree throughout my life. I thank the MTSE Program and Mr. Tony Howell, Director, Educational Opportunity Program at NJIT for the financial support that enabled me to focus on my research. I acknowledge with thanks the input from Ms. Clarisa Gonzalez, Associate Director of Graduate Studies and Dr. Sotirios Ziavras, Associate Provost for Graduate Studies in formatting and improving the presentation in this doctoral thesis.

I would like to thank research group members: Vijay Kasi Somayajula, Sarang Muley, Amirhossein Rajabi, El Mostafa Benchafia and Sanjay Pandya for their support in various aspects during my stay in New Jersey.

I am highly indebted to my Father, Hem Kant Lamsal and my Mother, Moti Devi Lamsal for their endless encouragement, support, sacrifice and blessing throughout my life. I would like to express my gratitude to my siblings Ambika (Lamsal) Acharya, Bishnu Lamsal and Dhruba Lamsal for their unconditional help and encouragement. I would like to thank my in-laws Radha Devi Sigdel, Kishor Sigdel and Arundati (Kharel) Sigdel for their moral support and help during my stay at NJIT. I would like to thank my wife, Laxmi (Sigdel) Lamsal for her encouragement, support and superior understanding during my work time, early morning to night, in addition to looking after our children, Arnav Lamsal and Charvy Lamsal.

TABLE OF CONTENTS

TABLE OF CONTENTS
(Continued)

Chapter **Page**

TABLE OF CONTENTS
(Continued)

LIST OF TABLES

LIST OF FIGURES

LIST OF FIGURES
(Continued)

Figure **Page**

LIST OF FIGURES
(Continued)

LIST OF FIGURES
(Continued)

Figure **Page**

LIST OF SYMBOLS

©	Copyright
TMO	Transition Metal Oxide
TCR	Temperature Coefficient of Resistivity
T_c	Critical Temperature
IMT	Insulator Metal Transition
V-O	Vanadium-Oxide
1D	One-Dimensional
2D	Two-Dimensional
CDW	Charge Density Wave
3D	Three-Dimensional
T_p	Peierls Temperature
IR	Infra-Red
HF	Hartree-Fock
DFT	Density Functional Theory
QMC	Quantum Monte-Carlo
E_b	Band-Width
k	Wave Vector
VO_2	Vanadium Dioxide
V_2O_3	Vanadium Sesquioxide
V_2O_5	Vanadium Pentoxide
KS	Kohn-Sham

LIST OF SYMBOLS
(Continued)

GGA	Generalized Gradient Approximation
L(S)DA	Local (Spin) Density Approximation
PP	Pseudo-Potential
USPP	Ultra-Soft Pseudopotential
LAPW	Linear Augmented-Plane-Wave
PAW	Projector Augmented Wave
BZ	Brillouin Zone
IBZ	Irreducible Brillouin Zone
FD	Fermi-Dirac
FFT	Fast Fourier Transform
GS	Ground State
SCF	Self-Consistent Field
NSCF	Non Self-Consistent Field
MP	Monkhorst-Pack
BFGS	Broyden-Fletcher-Goldfarb-Shanno
DOS	Density of States
M	Metal
I	Insulator
UHB	Upper Hubbard Band
LHB	Lower Hubbard Band
AFI	Anti-Ferromagnetic Insulating

LIST OF SYMBOLS
(Continued)

BTE	Boltzmann Transport Equation
RTA	Relaxation Time Approximation
τ_m	(Momentum) Relaxation Time
TE	Thermoelectric
σ	Electrical Conductivity
S	Seebeck Coefficient
K	Thermal (Electronic) Conductivity
μ	Chemical Potential
$\in(\omega)$	Dielectric Function
$\tilde{n}(\omega)$	Complex Refractive Index
n	Refractive Index
k	Extinction Coefficient
E	Electric Vector
R	Reflectivity
$\in_\infty$	High-Frequency Dielectric Constant
$\epsilon(0)$	"Zero-Frequency" Dielectric Constant
ε_0	Static Dielectric Constant
f_i	Phillips Ionicity
E_g	Band Gap Energy
E_h	Homopolar Energy Gap
C	Heteropolar Energy Gap

LIST OF SYMBOLS
(Continued)

E_F	Fermi Energy
E_p	Penn Gap
ω	Angular Frequency
n_{eff}	Effective Number of Electrons per Atom Participating in Optical Transitions over a given Frequency Range
CMB	Cosmic Microwave Background
MWIR	Mid Wave Infrared
LWIR	Long Wave Infrared
EM	Electro-Magnetic
λ	Wave-Length
K_B	Boltzmann Constant
T	Temperature
MEMS	Micro-Electro-Mechanical System
ROIC	Read-Out Integrated Circuit
R_v	Voltage Responsivity
G	Thermal Conductance
Å	Angstrom
ΔH	Enthalpy of Formation
°C	Degree Centigrade
ε-scaling	Ratio of Emissivity at Different Thicknesses to Emissivity at Thickness of 0.05μm, at λ = 16.5 μm

CHAPTER 1

INTRODUCTION

1.1 General Considerations

The state of a material, whether metallic or insulating, provides a clear and fundamental insight on its electric and electronic properties. Transition-metal oxides (TMOs) have unique physical, electronic, thermal, optical, chemical and magnetic properties [1]; they are ideal for the study of insulating and metallic states due to their diverse nature of electrical properties even within the material with similar structure [2]. A large number of TMOs can be categorized under good insulator, metal and yet a third class, which has low resistivity at room temperature similar to conventional metals but a negative temperature coefficient of resistivity (TCR) similar to semiconductor. These materials with "contradictory" properties are insulating/semiconducting at low temperatures but are metallic at higher temperatures above a critical temperature (T_c). Such Insulator-Metal Transitions (IMT) have also been observed in most of the vanadium-oxide (V-O) compounds over a wide range of temperatures depending on the O/V ratio [3].

The ground state electronic configuration of vanadium is $[Ar]3d^3 4s^2$. Being a d-transition metal, vanadium has different oxidation states that are capable of existing in both single as well as mixed valence states on forming oxides. The vanadium oxides such as VO, V_2O_3, VO_2 and V_2O_5 exist in a single oxidation state whereas many others, for instance: V_3O_5, V_4O_7, V_6O_{11}, V_6O_{13}, V_7O_{13}, V_8O_{15} etc., remain in mixed (two) valence state. However, these oxides can be categorized under the so-called Magnéli (V_nO_{2n-1}) and Wadsley ($V_{2n}O_{5n-2}$) homologous series. In this study, we focus on V_2O_3 (n=2) and VO_2 (n=∞) which are the two end members of Magnéli phases and V_2O_5 (n=∞), the end

member of Wadsley phases. Vanadium ions in VO_2 and V_2O_3 have $V^{4+}(d^1)$ and $V^{3+}(d^2)$ electronic structures whereas V_2O_5 has V^{5+} ion with no 3d electrons.

In transition metal oxides, the s band associated with the transition metal ions and the p band associated with the oxygen ions are pushed away from the Fermi level by ~ ±5eV and only d orbitals are close to it [2] and are of significant importance. Since the metal d orbitals form the conduction band, we expect some electrons in this band except with (d^0) configuration. Due to the small width of the d-conduction band in these oxides, electrons are seriously influenced by other interactions [4]. Octahedral coordination geometry in vanadium oxides creates a crystal-field (or ligand-field) which, in turn, splits the fivefold degenerate d orbitals into different sets of degenerate orbitals- for instance, low lying triply degenerate t_{2g} orbitals and higher lying doublet e_g in VO_2 as shown in Figure 1.1.

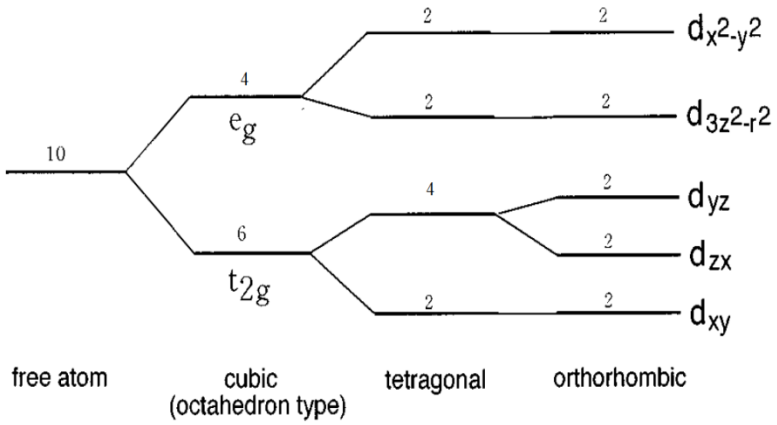

Figure 1.1 Crystal-field splitting of 3d orbitals under cubic, tetragonal, and orthorhombic symmetries. The numbers cited near the levels are the degeneracy including spins [5].

The crystal field splitting energy for 3d-series ions in oxides has value of 1-2 eV [4], which increases as cation oxidation state increases [6]. For spin 1/2 transition metal

oxides such as VO_2 to convert into a spin 1/2 insulator, an additional splitting of the higher lying doublet is required along with strong correlations [7]. Electron-electron correlations influence the electronic structure of a material [8].

Within conventional band theory-which treats the electrons as extended plane wave, insulators are defined as materials having completely filled valence band and an empty conduction band separated by a sizeable energy gap [9]. However, the TMOs undergoing IMT have incompletely filled 3d bands. deBoer and Verwey [10] explained this lack of conductivity, in the insulating phase, as an effect of the potential barrier existing between any two transition metal ions in the crystal as shown in Figure 1.2.

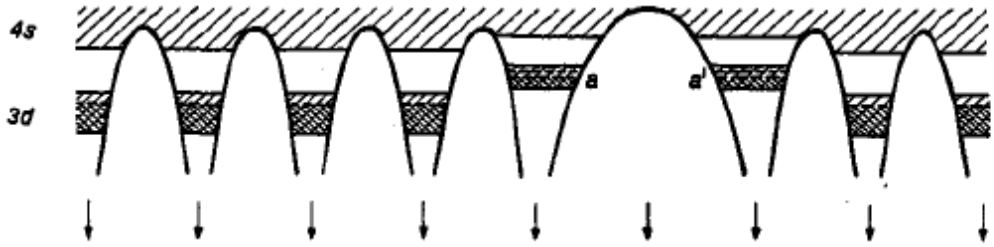

Figure 1.2 Schematic representation of the 3d and 4s bands in a substance like NiO. The arrows, pointing down, indicate the position of cations except the arrow between a and a', which is a vacant lattice point [10].

For the case where the electronic band width is small, it is possible that the correlation energy is sufficiently larger than the kinetic energy of the electrons and the electron remains localized. In other words, electrons are considered to be localized if the excited state is short lived as compared to the time that the electron would take tunneling through the barrier to reach it [11]. For an electron localized around an ion in ionic crystals, it is possible for the electron to be bound in the potential well resulting from the

lattice polarization due to its own presence and thus forming a “quasiparticle” known as a polaron. In contrast to large polarons, we call a polaron "small” when lattice deformation does not extend beyond nearest neighbors. The transfer of such charge carrier occurs only in response to appropriate motions of the neighboring atoms [12]. In fact, in small-polaron model, a self-trapped electron participates in conduction by phonon assistance from site to site in the form of uncorrelated hopping as thermal fluctuation momentarily brings about a configuration equivalent to initial distorted site. Thus, two steps are clearly involved in this process: the polarization arrangement with identical initial and final states and tunneling during the coincidence event. The small-polaron theory has been used to describe conduction mechanism in TMOs [11].

The transfer of a quantum particle from site to site can be described by two basic mechanisms: hopping and tunneling – which refer, respectively, to the transfer over a barrier due to thermal activation and transfer between two levels of same energy due to the overlap of the wavefunctions on the sites [13]. A schematic representation of these two mechanisms is shown in Figure 1.3.

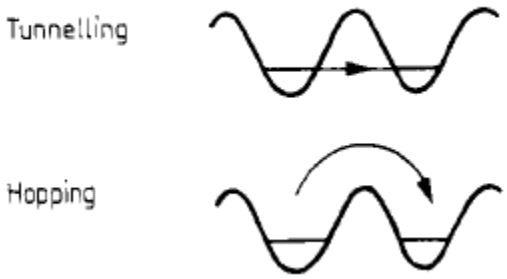

Figure 1.3 Transfer of a quantum particle across a potential barrier between two identical localized sites [13].

The mechanism of hopping can be explained by Arrhenius law $\log\boldsymbol{\sigma T \sim 1/T}$ derived from random walk theory. However, an "equivalent" relation $\log\boldsymbol{\sigma \sim 1/T}$ has been used frequently in the literature, for the ease of simplicity, to fit with the experimental data. It has been found that the activation energy required to surmount the barrier, the barrier height, obtained using either form is the same within errors in many cases [14]. The corresponding rule for tunneling appears empirically in the form $\log\boldsymbol{\sigma \sim T}$, a prediction of Tredgold model [15] for tunneling of quantum particle through a potential barrier of varying thickness caused by the lattice vibrations.

In transition metal oxides, d electrons are spatially confined in partially filled orbitals and are considered to be strongly interacting or "correlated" because of Coulombic repulsion between two d electrons of opposite spin on the same ion. In other words, the two conduction electrons with antiparallel spin at the same bonding site repel each other with strong Coulomb force so as to keep them mutually separated and hence spatially localized in individual atomic orbitals rather than behaving as delocalized Bloch functions. According to Mott and Peierls [16], electron-electron correlation could be the origin of the insulating behavior observed in TMOs. Obviously, the high potential barriers observed between the two atoms in a TMO are highly opaque for the electrons to pass through. However, the low transparency of the potential barrier cannot merely describe the observed conductivity in TMOs. Peierls [16] noted the solution of the problem as follows: "if the transparency of the potential barriers is low, it is quite possible that the electrostatic interaction between the electrons prevents them from moving at all. At low temperatures, the majority of the electrons are in their proper places in the ions. The minority which have happened to cross the potential barrier find

therefore all the other atoms occupied, and in order to get through the lattice have to spend a long time in ions already occupied by other electrons. This needs a considerable addition of energy and so is extremely improbable at low temperatures." Hence, low transparency and electron-electron correlation contribute to the electrical properties of TMOs and the conductivity at low temperature is proportional to a "high power" of the initial transparency.

1.2 Insulator-Metal Transitions (IMT): Mott, Hubbard, and Peierls Mechanism

Hartree-Fock band approximation, with the inclusion of crystal field splitting, failed to explain the insulating state of TMOs due to the neglect of electronic correlation. Later, Mott [17, 18] showed that electron-electron correlation can produce insulating states in any material, provided the lattice constant exceeds a critical value. He further suggested that metallic state always exist in these materials as excited state. Conduction in such an insulator is limited due to the formation of pairs of an electron and a hole, an exciton, which are bound to each other via a Coulomb interaction. However, above a critical concentration of excitons, the screened Coulomb interaction becomes so weak that a sharp transition occurs from no free carriers to larger number of carriers. This requires a high energy state which, in general, is hard to attain at ordinary temperature [2].

Hubbard presented a more quantitative, but still semi-quantitative, description of Mott transition introducing the effects of correlation on the Hamiltonian [19],

$$\mathbf{H} = \sum_{\mathbf{i,j}} \sum_{\boldsymbol{\sigma}} \mathbf{T_{ij}} \mathbf{C^{+}_{i\sigma}} \mathbf{C_{j\sigma}} + \mathbf{U} \sum_{\mathbf{i}} \mathbf{n_{i\uparrow}} \mathbf{n_{i\downarrow}} \qquad (1.1)$$

where, $\boldsymbol{n_{i\sigma} = C^{+}_{i\sigma} C_{i\sigma}}$ is the number operator for an electron in the state $\boldsymbol{i, \sigma}$; $\boldsymbol{T_{ij}}$ is fourier transform of the Bloch energies $\in (\boldsymbol{k})$; U is the average intra-ionic Coulomb repulsion. The first term represents the hopping motion of the electrons from atom to atom and the second term describes the repulsion of two electrons on the same atom. This model is simple in that it replaces the long range Coulomb potential by delta-function repulsion. Two configurations, with and without electrons on the same atom, separated by the onsite Coulomb repulsion U, are called the upper and lower Hubbard band in solids. We will have an insulating state if the repulsive term dominates over the hopping term. However, the energy gap due to electronic correlation shrinks continuously as the ratio of band-width (E_b) to U increases and becomes zero at a critical ratio when an insulator to metal transition occurs. This is not a sharp transition as predicted by Mott and is a consequence of neglecting inter-atomic Coulomb term, in Hubbard model, a term responsible for screening effect in Mott transition. It seems feasible that a large number of free carriers can effectively screen U and, thereby, reduce its value. It is doubtful that screening of such an intra-atomic quantity can be significant [2]. At the same time, an insulator–metal transition can be obtained if the effect of neglecting interatomic Coulomb interaction somehow compensates with an effective screening of U. Even though various explanations [20] have been proposed for the Mott-Hubbard transition, none of them has been clearly proved to prevail. Since the metallic and insulating states do not coexist, a continuous phase transition seems more probable; a discontinuous transition could simply be an artifact of the approximation scheme.

Another mechanism, encountered in literature, in interpreting the IMT in V-O system is Peierls type [21, 22]. It was Peierls [23] who first pointed out that a one-

dimensional (1D) metal coupled to the underlying lattice shows instability at low temperatures. In the absence of electron-electron or electron-phonon interaction, the ground state (at T=0K) of the coupled system has a periodic array of atoms with lattice constant a. In the presence of an electron-phonon interaction, the ground state is a condensate of electron-hole pairs accompanied by periodic lattice distortion of period 2a. The condensate is called charge-density wave (CDW) characterized by charge density $\boldsymbol{\rho}(\boldsymbol{r})$ associated with the collective mode formed by the electron-hole pairs [24],

$$\boldsymbol{\rho}(\boldsymbol{r}) = \boldsymbol{\rho_0} + \boldsymbol{\rho_1} \cos\ (2\,\boldsymbol{k_F}.\boldsymbol{r} + \boldsymbol{\varphi}) \tag{1.2}$$

where, $\boldsymbol{\rho_0}$ is the unperturbed electron density, $\boldsymbol{\varphi}$ is the phase of the condensate and Fermi wave vector $(\boldsymbol{k_F}) = \frac{\boldsymbol{\pi}}{\boldsymbol{a}}$. CDWs are mainly a 1D phenomenon. However, despite its occurrence in 2D- or 3D-band structures, most of the discussions are based on idealized one dimensional model.

A schematic representation of Peierls distortion, in 1D metal with half-filled band, is shown in Figure 1.4. This distortion opens up a gap at the Fermi level and, for small distortion, the configuration of the distorted system is energetically favorable [24]. At finite temperature T, the electron-phonon interaction is screened by the electrons that are excited across the gap and narrow the energy gap [25]. Consequently, the lattice distortion is reduced and a second order transition occurs at the so called Peierls temperature (T_p). The material shows metallic properties above T_p but becomes semiconducting below T_p. However, the attempts to interpret IMT in V-O systems, based on Peierls mechanism, have also been criticized [26].

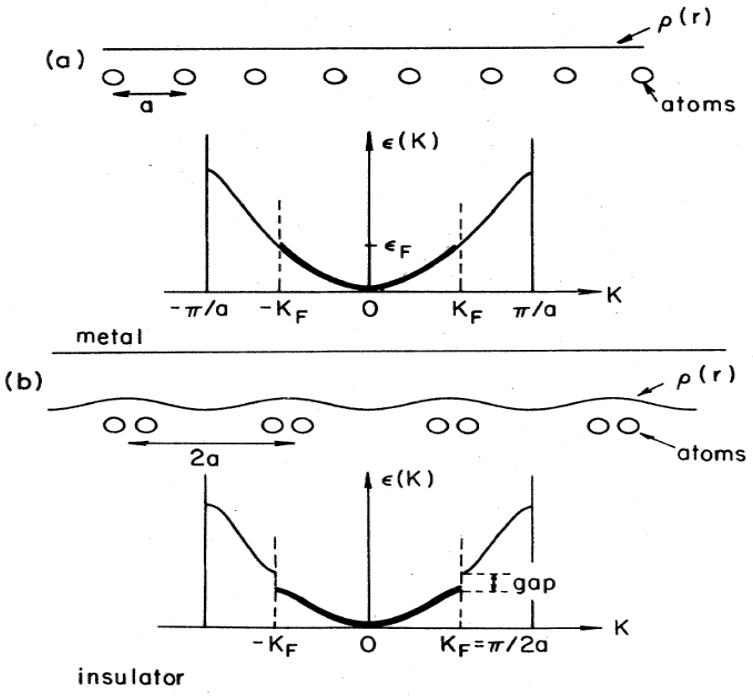

Figure 1.4 Peierls distortion (a) undistorted metal (b) Peierls insulator [24].

1.3 Literature Review

Correlated electrons are responsible for the extreme sensitivity of materials for small change in external stimuli such as pressure, temperature or doping [27]. VO_2 is one of the widely studied materials which undergoes IMT at 340K [28], while V_2O_3 and V_2O_5 show the transitions at 160K [29] and 530K [30], respectively. These phase transitions are reversible [31] and are accompanied by drastic change in crystallographic, magnetic, optical and electrical properties. During structural transition, atoms undergo displacement with redistribution of electronic charge in the crystal lattice and hence the nature of interaction changes [32]. Below T_c, VO_2 and V_2O_3 have monoclinic structure [33, 34] and V_2O_5 has orthorhombic structure [35]. At temperatures higher than T_c, they have crystal structures that are different from their low temperature counterparts [33, 36]. Similarly, the phase transition leads to change in electrical conductivity up to 10 orders of

magnitude [37], while optical and magnetic properties show discontinuity. Recently, the phase transition in bulk V_2O_5 has become a controversial issue even though the studies on its thin film show IMT; various transition temperatures have been reported for these materials in the literature [38, 39]. Kang et al. [39] have also concluded that V_2O_5 films undergo IMT without structural phase transition. Furthermore, the precise mechanism of IMT is still a matter of debate [40] and no theoretical understanding has been realized to predict the transition temperature [41].

The vanadium oxides are chromogenic materials and can change their optical properties due to some external stimuli in the form of photon radiation (photochromic), change in temperature (thermochromic) and voltage pulse (electrochromic); the change becomes discontinuous during IMT. Such properties can be exploited to make coatings for energy-efficient "smart windows" [42], and electrical and optical switching devices [43]. Thin films of VO_2 and V_2O_3 have been found to show good thermochromism in the infrared region [44, 45]. While maintaining the transparency to visible light, a smart window modulates infrared irradiation from a low-temperature transparent state to a high-temperature opaque state [46]. The two oxides, VO_2 and V_2O_5, can change their optical properties in a persistent and reversible way in response to a voltage [47]. V_2O_5 exhibits exceptional electrochromic behavior because it has both anodic and cathodic electrochromism, different from VO_2 which has only anodic electrochromism, and is also an integral part in band structure effects [47]. These electrochromic materials have four main applications: information displays, variable-reflectance mirrors, smart windows and variable-emittance surfaces.

The V-O systems are widely applicable in technology such as memory devices and temperature sensors [48]. The memory aspect of the material is evidenced from the pronounced hysteresis present in the phase transition [49]. Normally, the range of operation of a device lies outside the hysteresis region. Some bolometric devices are operational within the hysteretic transition [50]. Bolometers are thermal infrared (IR) detectors and can be used in infrared imaging applications such as thermal camera, night vision camera, surveillance, mine detection, early fire detection, medical imaging, and detection of gas leakage. A bolometer requires a material with high temperature coefficient of resistance (TCR) and a small 1/f noise constant [51]. Pure, stoichiometric single-crystals of VO_2 and V_2O_5 have high TCR but are difficult to grow. Furthermore, the latent heat involved in IMT is highly unfavorable for the bolometric performance [52]. Since T_c of V_2O_3 is far below room temperature, the resistance and hence the level of noise is low which makes V_2O_3 a good candidate for the fabrication of efficient micro-bolometers. Cole et al. [53] have shown that the thin films of all the three oxides, combined together, can produce a desired material with high TCR and optimum resistance for bolometer fabrication.

TMOs, among others, are the best candidates for the cathode materials for rechargeable Li-ion batteries. Due to the layered structure of V_2O_5, it has decent ionic storage capacity. The cathode material currently being used, coarse-grained Li_xCoO_2, has a practical energy density < 500 Wh/kg which is far less than a theoretical energy density of ~1100Wh/kg for lithiated V_2O_5 [54]. Panasonic has commercialized the use of V_2O_5 as a cathode material in rechargeable Li-ion batteries for low energy applications (button cells). The energy density of this product is 100-140 Wh/L and has been found to be

insensitive to overcharging [55]. TMOs, being stable at high temperature along with their tunable transport properties and well established synthesis techniques, are gaining attention for their thermoelectric properties [56]. V_2O_5 is known to have hopping transport mechanism, with anisotropic n-type electrical conduction. The Seebeck coefficient varies slowly with temperature indicating the applicability of V_2O_5 as a thermistor [57].

Clearly, phase transition in VO_2 is of high technological interest. IMT occurs near to room temperature and T_c can be tuned optically, thermally, electrically [58] and with doping [37]. The phase transition in VO_2 has been used to achieve frequency-tunable metamaterials in the near-infrared range [59, 60]. Recently, Kyoung et al. [61] have extended the study to terahertz range proposing an active terahertz metamaterial, a gold nano-slot antenna on a VO_2 thin film, which transforms itself from transparent to complete extinct at resonance when the VO_2 film undergoes thermo or photoinduced phase transition. Cavalleri et al. [33] showed that the phase transition can be photoinduced within hundreds of femtoseconds which can be an underlying principle for an ultrafast switch.

Vanadium dioxide (VO_2) [44, 62] and vanadium sesquioxide (V_2O_3) [63, 64] are the model systems used to study IMT in correlated electron systems. V_2O_5 is the most stable among the other two and exhibits highly anisotropic optoelectronic properties [39, 65]. While the study of vanadium-oxide systems is an exciting field of research due to its significant technological applications, the phase transition, high sensitivity to microscopic details and anisotropic nature make the study more difficult. In general, the conventional band theory, which treats the electrons as extended plane waves, can

explain the metallic behavior of a material but fails to account for the localized electrons [66]. In transition metal oxides, the d electrons are partially localized and partially itinerant [67] and, during IMT, an electron changes its behavior from localized to itinerant. Even though the Mott-Hubbard transition (strong electron-electron interactions) and the Peierls mechanisms (electron-phonon interactions) are considered to be responsible for IMT, no general consensus has been reached amongst the scientific community [68]. Coping with such a transition problem, which involves understanding the "competition" between kinetic (wavelike) and correlation (particle like) terms in the electronic level, is still an exciting field of research and is the heart of electronic many body problems.

CHAPTER 2

FIRST PRINCIPLES ELECTRONIC STRUCTURE METHODS

Ab initio calculations are becoming widely popular in studying electronic structures and various physical properties (e.g., ground state energy, dipole moment, polarizability, vibrational frequencies and nuclear quadrupole moment) of many-electron systems [69-72]. The first principles approaches can be classified into three main categories: the Hartree-Fock (HF), the density functional theory (DFT) and the quantum Monte-Carlo (QMC) approaches [70]. The Hartree-Fock self-consistent method is based on the one-electron approximation in which the motion of each electron, in the effective field of all the other electrons, is governed by a one-particle Schrödinger equation. In this approximation, the "Hartree-Fock" energy of many-electron system having N-electrons can be written as,

$$E^{(0)} + E^{(1)} = E^{HF} \tag{2.1}$$

where,

$$E^{(0)} = \left\langle \Psi^{(0)} \mid \hat{H}_0 \mid \Psi^{(0)} \right\rangle = \sum_i \varepsilon_i \tag{2.2}$$

is the expectation value of sum of the one-electron Fock operators and is known as the lowest energy eigenvalue of the unperturbed system. Similarly, the expectation value of first order perturbed Hamiltonian $\hat{H}'$ over the unperturbed state $\Psi^{(0)}$ of the system is written as,

$$E^{(1)} = \left\langle \Psi^{(0)} \mid \hat{H}' \mid \Psi^{(0)} \right\rangle \tag{2.3}$$

which is the first order perturbation energy correction to the unperturbed energy $E^{(0)}$.

The Hartree-Fock wave function satisfies the antisymmetry requirement and it includes the correlation effects arising from the pairs of electrons of the same spin. However, the motions of the electrons of the opposite spin remain uncorrelated in this approximation. The methods beyond the HF approximation, which deal with the phenomenon associated with many-electron system, are known as electron correlation methods. One of the approaches to electron correlation is the Møller-Plesset (MP) perturbation method which adds higher excitations to the HF approximation as a non-iterative correction utilizing techniques from many-body perturbation theory [71, 73].

Another first principles approach, to calculate the electronic structure of many-electron systems, incorporating electron correlation, is the density functional theory (DFT). In this theory, exchange-correlation energy is expressed, at least formally, as a functional of the resulting electron density distribution, and the electronic states are solved self-consistently as in the HF approximation [70]. In the HF approximation, the exchange interaction is treated exactly but the dynamic correlation, arising due to Coulomb repulsion, between the electrons is neglected. The density functional theory, in principle, is exact but, in practice, both exchange and dynamic correlation effects are treated approximately [74].

2.1 Modern Density Function Theory: Kohn-Sham Approach

The history of Density Function Theory (DFT) begins with Thomas-Fermi approach in the 1920s [75, 76]. The theory was given subsequent extensions until 1964, when Hohenberg and Kohn [77] proved a theorem that the ground state energy (E) of a many-electron system, from Schrödinger equation, is a unique functional of electron density, $E[\rho\,(r,\theta,\varphi)]$. By introducing orbitals, ϕ_i, Kohn and Sham formulated a set of equations called Kohn-Sham (KS) equations,

$$\left[-\frac{\hbar^2}{2m}\boldsymbol{\nabla}^2 - \sum_A Z_A \frac{e^2}{|\mathbf{r}-\mathbf{R_A}|} + e^2\int\frac{\rho(\mathbf{r}')}{|\mathbf{r}-\mathbf{r}'|}d\mathbf{r}' + U_{XC}(\mathbf{r})\right]\phi_i = \varepsilon_i\phi_i \qquad (2.4)$$

1 2 3 4

where,

first term, E_k = Kinetic energy acting on orbital,

second term, V_{nuc}= Nuclear attraction potential acting on orbital,

third term, $V_H[\rho]$ = Columbic interaction of electron in orbital, ϕ_i, with other electrons in the molecule (Hartree potential),

fourth tem, $U_{XC}[\rho]$ = exchange electron correlation potential.

Unlike Schrödinger equation (which depend on N-electrons' 3N coordinates), the Kohn-Sham equations depend on electron density, $\rho\,(r,\theta,\varphi)$, which, in turn, depend on orbital,

$$\rho\,(r,\theta,\varphi) = \sum_i |\phi_i|^2 \qquad (2.5)$$

Hartree potential includes a self-interaction term since the orbital that is being described in KS is also a part of the electron density, which is unphysical. U_{XC} needs to be constructed in such a way that the self-interaction contained in the Columbic interaction could be removed. Since the true form of exchange correlation is not yet known, this term needs to be approximated in some way – the major approximation involved in DFT. However, the orbital concept in KS equation gives 99% of the kinetic energy right; thus, the accurate density is obtained except for a small contribution from exchange correlation.

The most widely used approximations to exchange-correlation within DFT are Local Density Approximation (LDA) and Generalized Gradient Approximation (GGA). LDA was proposed by Kohn and Sham in 1965 based on the concepts developed in the Thomas Fermi Dirac theory. The main aspect of LDA is to treat a general inhomogeneous electronic system as locally homogeneous. This functional is known exactly but use of such a uniform electron gas cannot represent the electron density of a molecular system accurately. In order to study magnetic properties, Local Spin Density Approximation (LSDA) can be used which basically generalizes LDA to include electron spin. Within L(S)DA, wide bands of s and p orbitals are addressed well but the correlations of electrons in narrow bands (d and f bands) are weakly described, in general. GGA, on the other hand, uses the information about local electron density and the local gradient in the electron density [78]. Depending on the way information is used from the electron density and its local gradient, a large number of L(S)DA/GGA functionals have been developed.

In order to solve the KS equation, we need to define Hartree potential which depends on electron density. The electron density, in turn, depends on orbital, ϕ_i, which are only known after solving KS equation. To solve this "chicken-egg" problem, we adopt an iterative method as indicated in the flow chart (Figure 2.1) and obtain self-consistent solution (solution obtained from the iterations until the convergence is reached). The closer is the starting wave function to the true function, the lesser are the SCF iterations required in the calculations.

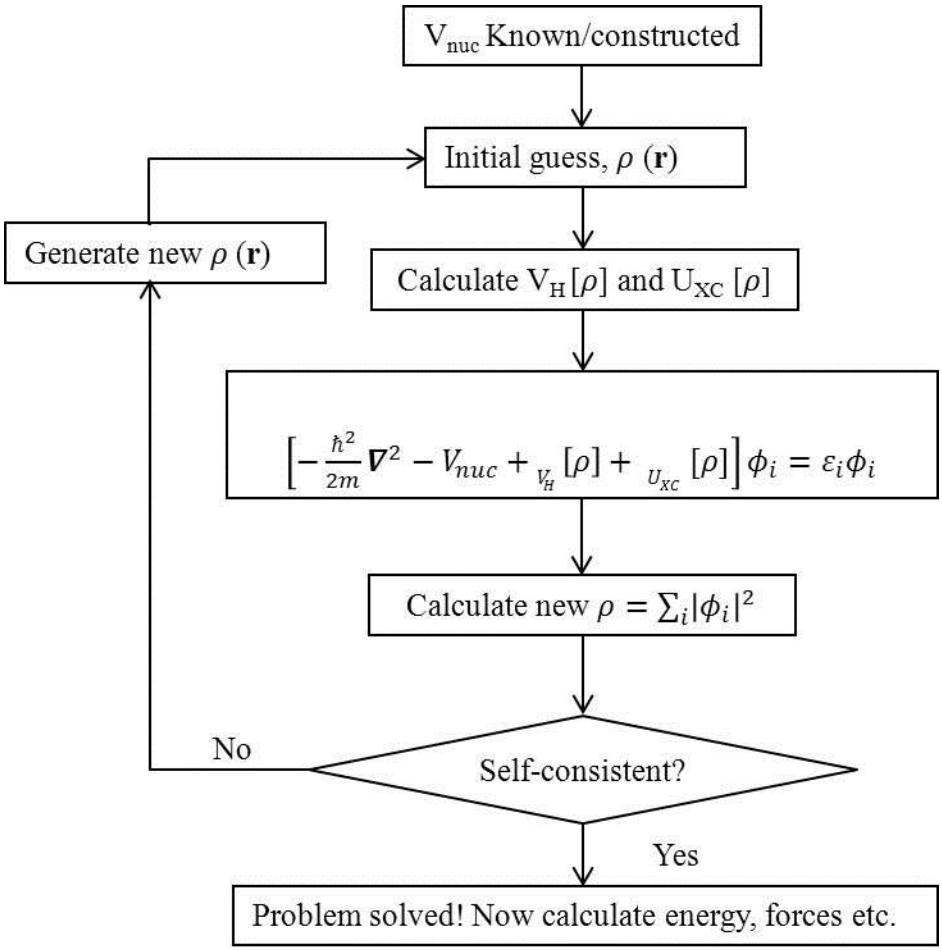

Figure 2.1 Solving the KS equations for a set of fixed nuclear positions.

2.2 Basis Sets

An isolated system (atoms/molecules/clusters) does not interact with others and hence no boundary condition is required. A material can be thought of being made of unit cell by repeating it indefinitely in all directions. In computer simulations, a unit cell along with a set of boundary conditions is used to approximate such a periodic system. The solution of Kohn-Sham equation, for such a periodic system, must satisfy Bloch's theorem; the Kohn-Sham orbital, $\phi_i(\mathbf{r})$, can be written in terms of two factors as,

$$\phi_i(\mathbf{r}) = e^{i\mathbf{k}.r}\, u_i(\boldsymbol{r}) \tag{2.6}$$

where, $e^{i\mathbf{k}.r}$ is called plane wave and the function $u_i(\boldsymbol{r})$ is such that it is periodic in space with the same periodicity of the unit cell of the system. It is the Bloch theorem that makes the problem easier to solve in reciprocal space than in real space. Further, the periodicity of $u_i(\boldsymbol{r})$ allows us to write it in terms of a set of plane waves as (Fourier expansion of periodic function),

$$u_i(\boldsymbol{r}) = \frac{1}{\sqrt{\Omega}} \sum_G C_{i,G}\, e^{iG.\boldsymbol{r}} \tag{2.7}$$

where, Ω is the volume of the unit cell of the lattice, $\mathbf{k}$ is the wave vector in the first Brillouin zone, G is the reciprocal lattice vector. Hence, the orbital can be written as,

$$\phi_i(\boldsymbol{r}) = \frac{1}{\sqrt{\Omega}} \sum_{G} C_{i,G}\, e^{i(\boldsymbol{k}+\boldsymbol{G}).\boldsymbol{r}} \tag{2.8}$$

The most natural choice of basis sets for studying periodic system would be plane wave basis sets. Equation (2.8) consists of infinite number of plane waves in the sum and in real calculation, we need to truncate it to some finite number.

With the orbital of the form (2.8), the kinetic energy is written as,

$$\mathrm{E} = \frac{\hbar^2}{2\,\mathrm{m}} |\mathrm{k} + \mathrm{G}|^2 \tag{2.9}$$

Since solutions with lower energies are more physically important, we can truncate the infinite sum (2.8) to a value E_{cut} such that $\frac{\hbar^2}{2\,\mathrm{m}} |\mathrm{k} + \mathrm{G}|^2 \leq E_{cut}$ (It is just a tradition to express this cutoff in energy units).

2.3 Pseudopotential

For the true nuclear potential, wave functions corresponding to the core electrons exhibit sharp peaks as shown in Figure 2.2. In order to address this fast spatial variation, we need a large number of plane waves. In other words, the plane waves associated with tightly bound core electrons in atoms oscillate in the short length scale (also, valence wavefunctions have wiggles: n-1 nodes near nucleus, n being principle quantum number) and involve large energy cutoffs. Since the chemical and physical properties of a material mainly depend on less-tightly-bound electrons of the outer shells rather than tightly bound core electrons, core electrons can be treated as a big system with the nucleus.

Hence, instead of using exact potential, we use an effective potential called pseudo potential (i.e., to replace potentials 1 through 4 in equation 2.4) which is pre-calculated in an atomic environment and kept frozen during the calculation. In other words, the use of pseudopotential avoids the situation of taking into account the core electrons in the plane wave expansion, which would otherwise require higher energy cut-off energy. Pseudopotentials are used in electronic structure calculation with great success, reasonable accuracy and a much more time efficient manner.

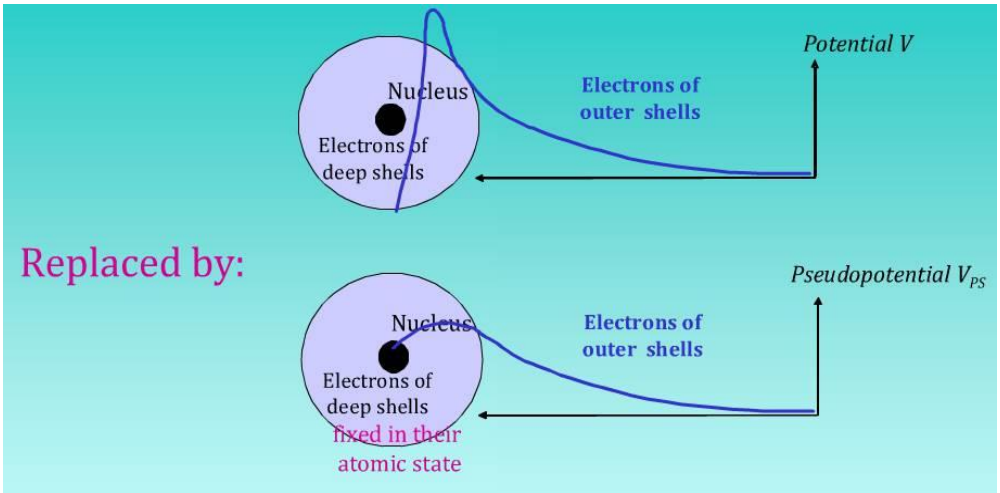

Figure 2.2 A typical comparison of exact potential with pseudopotential [79].

All-electron (exact) potential and pseudopotential are same beyond a particular distance from the nucleus, called cutoff or core radius. A particular pseudopotential defines the atom, number of electrons treated as valence/core electrons, type of exchange correlation functional and minimum energy cutoff required in a calculation. Since the pseudopotentials are not unique, we are free to choose a form that simplifies the calculation and the interpretation of the resulting electronic structure [80].

Pseudopotentials can be soft and hard depending on the cutoff energies considered; hard potentials require high cut off energies while the soft ones require low cutoff energies. Mostly used pseudopotentials are norm-conserving and ultra-soft pseudopotentials. The norm-conserving pseudopotential was first introduced by Hamann, Schlüter, and Chiang [81] based on ab initio atomic calculations. The norm conservation criterion generally produces hard pseudopotential. However, it is not always necessary that the norm of pseudo-wave and all-electron wave functions coincide [82]. On the other hand, the ultra-soft pseudopotentials (USPPs) which require substantially lower cutoff energies are based on the work of Vanderbilt [83]. In practice, cutoff radius in USPP is chosen very large, well beyond the maximum of the radial wave function; sharp peaks in the pseudo-wave function are replaced by smoother wave functions. However, it has a disadvantage of requiring a large number of empirical parameters during the construction process.

Blöchl introduced another frozen core approach that generalizes both the linear augmented-plane-wave (LAPW) method and the pseudopotential method "in a natural way" [84]. Later, Kresse and Joubert [85] implemented the Projector Augmented Wave (PAW) method in the plane wave calculations. Even though all electrons are not treated explicitly in the PAW formalism, it is sometimes referred to as an all-electron method in a sense that valence electronic states are kept orthogonal to the core wave functions. Some of the disadvantages of USPPs can be avoided with this PAW method.

2.4 Integral over the First Brillouin Zone

Many quantities such as electron density, total energy etc. involve integrating i^{th} band of a function, $f_i(\boldsymbol{k})$, over the possible values of **k** in the first Brillouin Zone (BZ) as,

$$\overline{f_i} = \frac{1}{\Omega_{BZ}} \int_{BZ} d\boldsymbol{k}\, f_i\,(\boldsymbol{k}) \tag{2.10}$$

However, in principle, we need infinite number of **k** points and the integral should be replaced by sum over a finite number of k-points: BZ Sampling.

$$\overline{f_i} = \frac{1}{\mathrm{N}_k} \sum_{k} f_i(\boldsymbol{k}) \tag{2.11}$$

The sum over the k-points in the Brillouin Zone can be reduced to the sum in the Irreducible part of the Brillouin Zone (IBZ), by employing all symmetry operations of the Bravais lattice to individual k-point (This will highly reduce the computational time). We can calculate the "weight", w_k, for each k-point in the IBZ by the following relation,

$$w_k = \frac{\text{Number of symmetry connected k} - \text{points}}{\text{Total number of k} - \text{points in the BZ}} \tag{2.12}$$

Then sum over the BZ becomes sum over the IBZ,

$$\overline{f_i} = \sum_{k}^{IBZ} w_k\, f_i(\boldsymbol{k}) \tag{2.13}$$

There are mainly two commonly used approximations for the sum over irreducible part of the BZ: (Linear) tetrahedron method and special k-points approaches. Special k-points

scheme has now been widely used in the calculations, which are Chadi-cohen k-points, Cunningham k-points and Equidistance or Monkhorst-Pack grids schemes.

When the general shape of a function, to be integrated, is unknown, the most straight forward approach is to construct equidistant grid. Monkhorst and Pack (MP) [86] developed a method for obtaining sets of special points in the Brillouin zone. The points in the k-space are written as a linear combination of lattice vectors in k-space: $\boldsymbol{k} = n_1\boldsymbol{b_1} + n_2\boldsymbol{b_2} + n_3\boldsymbol{b_3}$, where $(q_1 \times q_2 \times q_3)$ grid has the coordinates: $n_i = \frac{2p_i - q_i - 1}{2q_i}$, $p_i = 1, \ldots, q_i;\ i = 1, 2, 3.$

2.5 Metals – Fermi Surface Sampling

In metals, the Fermi surface separates the occupied electronic states from the unoccupied ones. In other words, the functions to be integrated in k-space show a discontinuity at the Fermi surface as indicated by "Θ-function"/step function,

$$\overline{f_i} = \sum_{k}^{IBZ} w_k \, f_i(\boldsymbol{k}) \, \Theta(\varepsilon_i(\boldsymbol{k}) - \varepsilon_F) \tag{2.14}$$

where, the step function is defined as $\Theta(\varepsilon_i(\boldsymbol{k}) - \varepsilon_F) = {}^{1,\ if\ \varepsilon_i(\boldsymbol{k}) < \varepsilon_F}_{0,\ if\ \varepsilon_i(\boldsymbol{k}) > \varepsilon_F}$. This imposes a serious complication in calculating integrals and hence special efforts have to be made to address this issue; otherwise, a very large number of k points are required to reach the convergence in the calculations. On the other hand, the Fermi level is adjusted to satisfy the normalization condition: $\sum_{\boldsymbol{k}\in\boldsymbol{BZ}} N_k w_k = N$, during self-consistency; for k-points near to the Fermi-surface, the coarse grid can lead to the highest occupied bands entering or

exiting the sums from one iteration step to the next. This introduces instability in the finite sum during the self-consistent procedure.

The remedy to this problem is to replace the step function by a smoother function $f(\{\varepsilon_i(\boldsymbol{k})\})$ which allows partial occupancies at the Fermi level. This, basically, "smears out" the discontinuity by forcing the function being integrated to be continuous and hence such approaches are called smearing methods. One of the commonly used smearing functions is the Fermi-Dirac (FD) function,

$$f(\{\varepsilon_i(\boldsymbol{k})\}) = \frac{1}{e^{\frac{(\varepsilon_i(k)-\varepsilon_F)}{\sigma}}+1};\ \sigma = k_B T \tag{2.15}$$

The broadening energy parameter, σ, should be adjusted to avoid instability in the SCF convergence procedure and hence regarded as one of the convergence parameters. Clearly the F-D function approaches step function in the limit T tends to zero. However, the broadening parameter cannot be related to electronic Fermi temperature unless the system is at really finite electronic temperature (finite temperature extension of Kohn-Sham theory by Mermin [87]): in general, it is just a technical issue. Several other smearing functions have been introduced to approximate the step function such as Gaussian smearing function, Method of Methfessel-Paxton and "cold" smearing of Marzari-Vanderbilt. Besides the smearing techniques, a method of tetrahedron is also used in which BZ is divided into tetrahedra, interpolate the function within these tetrahedra and then perform integration.

2.6 ABINIT

ABINIT is a full ab-initio, free to use, simulation package based on density functional theory, pseudopotentials and plane waves. In such plane wave based electronic structure calculations, Fast Fourier transforms (FFTs) are used, which are proved to be an efficient algorithm to transform functions (wave functions/electron densities) from real space to their reciprocal space counterparts. ABINIT mainly computes charge density, total energy and electronic structure of a periodic system based on Kohn-Sham density functional approach. In the usual ground state (GS) calculation or structural relaxation, the potential has to be determined self consistently. Several choices for the selection of algorithm for SCF are possible in ABINIT. In our calculations, using ABINIT (version 7.6.3) [88, 89], we chose the default integer for Self-Consistent-Field cycle: iscf=17 which refers to Pulay mixing of the density [90], the algorithm for accelerating convergence in SCF procedure. ABINIT requires parameters such as atomic species and their position within a particular structure as its input variables – the atoms are placed in a unit cell, which is built by taking the symmetries of the system into consideration. Band occupation scheme has to be specified during the calculations, which is basically the smearing technique: “cold smearing” of Marzari (bump minimization) [91] is chosen for metallic case (occopt=4) but default value (occopt=1) is taken elsewhere. The temperature of smearing is taken to be 0.01 Hartree (tsmear = 0.01 Ha) as suggested, for d-band metals, in ABINIT website (the convergence calculation with respect to this parameter should be checked; large value leads to the convergence at wrong value and small value requires a large number of k-points). Monkhorst-Pack Grid was chosen for Brillouin zone sampling and a convergence test was done to determine the density of k-

mesh. Another convergence test was also performed to truncate the plane wave expansion, which was found to be 40 Hartree (ie ecut= 40 Ha).

PAW potential used in our calculations are those with the smallest pseudopotential radii, generated using a program called AtomPaw [92, 93], for both vanadium (V) and oxygen (O), obtained from Case Western Reserve University, which were well tested with previously confirmed data; the choice of valence bands was such that no "ghost" or "phantom" bands appeared in the band structures; minimum volume of the unit cell, bulk modulus, and the derivative of the bulk modulus were examined [94]. In oxygen, electrons in the first shell (n=1) were treated as core electrons while in vanadium, the electrons in first and second shell (n=1 and 2) were treated as core electrons. Approximation to exchange-correlation used in the calculations is Local Density Approximation (LDA) with the functional of Perdew and Wang (PW92) [95]. We have an advantage of using LDA in our calculations in that they have the tendency of having smaller radii for their pseudopotential spheres which is consistent with relatively tightly packed vanadium oxide (VO_x: x=1.5, 2 and 2.5) structures.

2.7 Vanadium Oxides: Symmetries and Structure

A crystal structure can be constructed uniquely from its lattice defined by lattice vectors, $\mathbf{R_i}$, and its basis defined by lattice basis vectors, $\mathbf{r_i}$. A basis vector in the unit cell can be expressed as a linear combination of the lattice vectors. For a unit cell having p number of atoms we can write,

$$\mathbf{r_i} = x_i\mathbf{R_1} + y_i\mathbf{R_2} + z_i\mathbf{R_3}; i = 1, 2, 3, \dots, p \qquad (2.16)$$

where, relative coordinates x_i, y_i, z_i (with $|x_i|, |y_i|, |z_i| < 1$) are used to locate atoms in the unit cell. Here, the lattice and basis are connected to each other by the symmetry elements of the crystal structure. In ABINIT, the unit cell of a crystal structure is defined using acell/rprim (rprim, in general, defines the unit lattice vectors which are then scaled by acell variable to obtain $\mathbf{R}_i$); alternately, acell/angdeg input variables can also be used. Using the Wyckoff positions, we can locate the atoms in the unit cell in terms of relative coordinates.

For small change in external stimuli such as pressure, temperature or doping [27], several vanadium oxides undergo insulator-to-metal phase transition (IMT) that are accompanied by structural change and this leads to the change in number of formula unit (z) in the primitive unit cell. Below the phase transition temperature T_c, vanadium dioxide possesses monoclinic (insulating) structure and its primitive cell contains four formula units (z=4; 12 atoms). In its metallic phase, above T_c, it acquires rutile structure and contains two formula units (z=2; 6 atoms). For temperature below T_c, V_2O_3 has monoclinic structure with 20 atoms in its unit cell (z=4), while above T_c, the structure changes to trigonal corundum ("corundum" was derived from Sanskrit word "Kuruvinda", meaning ruby) with 10 atoms in the primitive unit cell. V_2O_5 has simple orthorhombic structure and its bulk phase does not undergo phase transition (i.e., remains semiconducting at all temperatures). The primitive unit cell contains two formula units (z=2; 14 atoms). Due to its layered structure and weak bonds between layers, few layers thick (~nm) or even a monolayer of V_2O_5 is possible to extract. IMT has been observed in the film of V_2O_5 but without structural change. Since graphene (single layer of graphite) exhibits interesting properties unlike its bulk counterpart, researchers are

curious whether analogous useful and exciting properties can be observed in the single layer of V_2O_5!

2.7.1 Vanadium Dioxide (VO_2)

Vanadium oxide, below T_c, can exist in two phases: stable phase/M_1 phase ($\beta = 122.65^o$) and metastable phase/M_2 phase ($\beta = 91.88^o$). The metastable phase is normally induced by either doping or stress. Since we are mainly focused on the temperature induced phase transition, we will study the most stable phase and its primitive unit cell is defined by following lattice parameters [96],

$$\mathrm{a} = 5.7517\text{Å};\ \mathrm{b} = 4.5378\text{Å}\ ;\mathrm{c} = 5.3825\text{Å}\ ;\ \beta = 122.646^o \tag{2.17}$$

Table 2.1 Wyckoff Parameters of the Stable Phase of VO_2: Simple Monoclinic Structure

Atom	Wyckoff position	Parameters		
		x	y	z
V	4e	0.23947	0.97894	0.02646
O_1	4e	0.10616	0.21185	0.20859
O_2	4e	0.40051	0.70258	0.29884

The M_1 phase of stoichiometric VO_2 is characterized by a simple monoclinic lattice with space group $P2_1/c$ (C_{2h}^5, $No.14$) [97]. Vanadium atom and the two types of oxygen atoms occupy the Wyckoff position (4e): $\pm(x,y,z), \pm(x,\frac{1}{2}-y,\frac{1}{2}+z)$ where x, y, z are shown in Table 2.1 [97]. With this definition of crystal structure of VO_2 and "cut3d" utility of ABINIT, XCrySDen [98] (a program for displaying Crystalline Structure and

Densities under X-window environment) was used to visualize the crystal structure, which is shown in Figure 2.3.

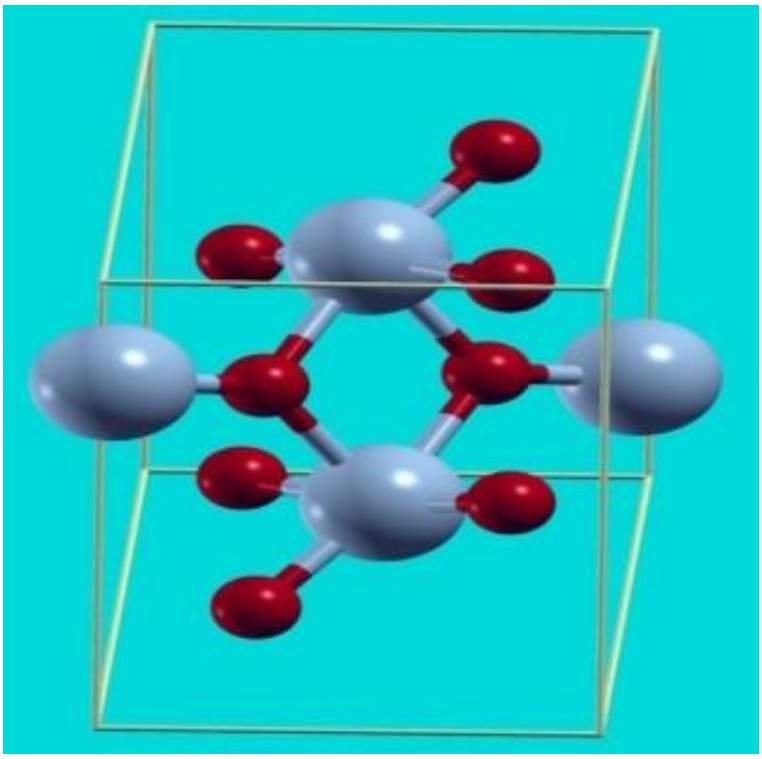

Figure 2.3 Monoclinic structure of stable phase of VO_2: V atoms (grey) and O atoms (red) are shown.

Similarly, at temperature above T_c, VO_2 has the rutile structure and its primitive unit cell is defined by the following lattice parameters,

$$\mathbf{a_R} = a_R(1,0,0);\ \mathbf{b_R} = a_R(0,1,0);\ \mathbf{c_R} = c_R(0,0,1) \tag{2.18}$$

with $a_R = 4.5546\text{Å}$ and $c_R = 2.8514\text{Å}$. Simple tetragonal lattice has space group $P4_2/mnm(D_{4h}^{14},\ No.136)$ and accordingly, vanadium atoms occupy the Wyckoff

position (2a): (0,0,0), $(\frac{1}{2},\frac{1}{2},\frac{1}{2})$ and oxygen atoms occupy the Wyckoff position (4f): $(x,x,0)$, $(-x,-x,0)$, $\left(-x+\frac{1}{2},x+\frac{1}{2},\frac{1}{2}\right)$, $\left(x+\frac{1}{2},-x+\frac{1}{2},\frac{1}{2}\right)$, with x = 0.3001 [97]. With this data, the crystal structure of VO_2 (Rutile) is visualized, which is shown in Figure 2.4.

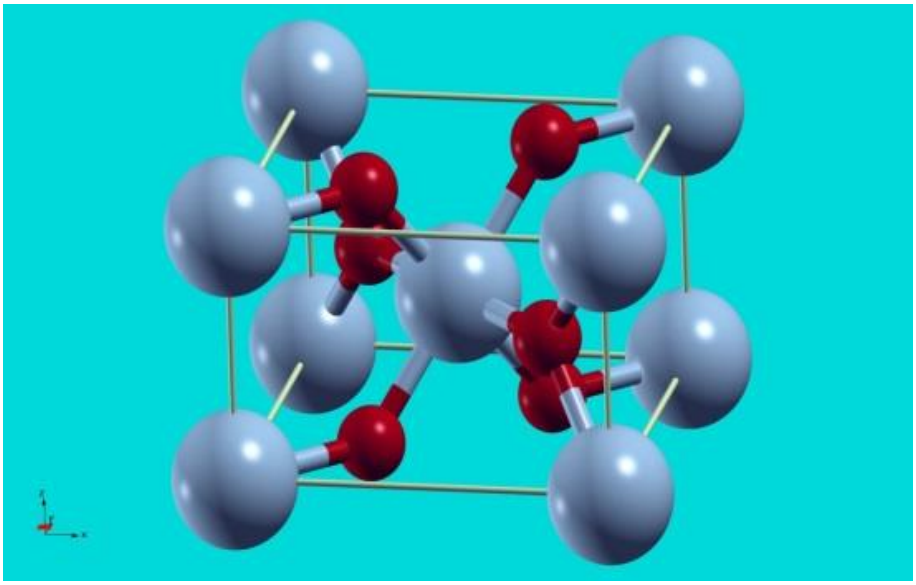

Figure 2.4 Rutile phase of VO_2: V atoms (grey) and O atoms (red) are shown.

2.7.2 Vanadium Sesquioxide (V_2O_3)

Vanadium sesquioxide (V_2O_3), in its insulating phase, has inner centered (body centered) monoclinic lattice with space group $I2/a(C_{2h}^6,\ No.15)$ and accordingly, vanadium and first kind of oxygen atoms occupy the Wyckoff position (8f): $\pm(x,y,z)$, $\pm(\frac{1}{2}+x,-y,z)$, $\pm(\frac{1}{2}+x,\frac{1}{2}+y,\frac{1}{2}+z)$ and $\pm(x,\frac{1}{2}-y,\frac{1}{2}+z)$ with $(x, y, z)_V$ = (0.3438,0.0008,0.2991) and $(x, y, z)_{O1}$ = (0.407, 0.845, 0.652) while the other kind of oxygen atoms occupy the

Wyckoff position (4e): $\pm(\frac{1}{4}, y_{o2}, 0)$, $\pm(\frac{3}{4}, \frac{1}{2} + y_{o2}, \frac{1}{2})$ with y_{o2} = 0.191 [99]. The unit cell of the monoclinic lattice is defined by following lattice parameters [36],

$$\text{a} = 7.255\text{Å};\ \text{b} = 5.002\text{Å}\ ;\ \text{c} = 5.548\text{Å}\ ;\ \beta = 96.75^{\text{o}} \tag{2.19}$$

With these data, the crystal structure was visualized which is shown in Figure 2.5.

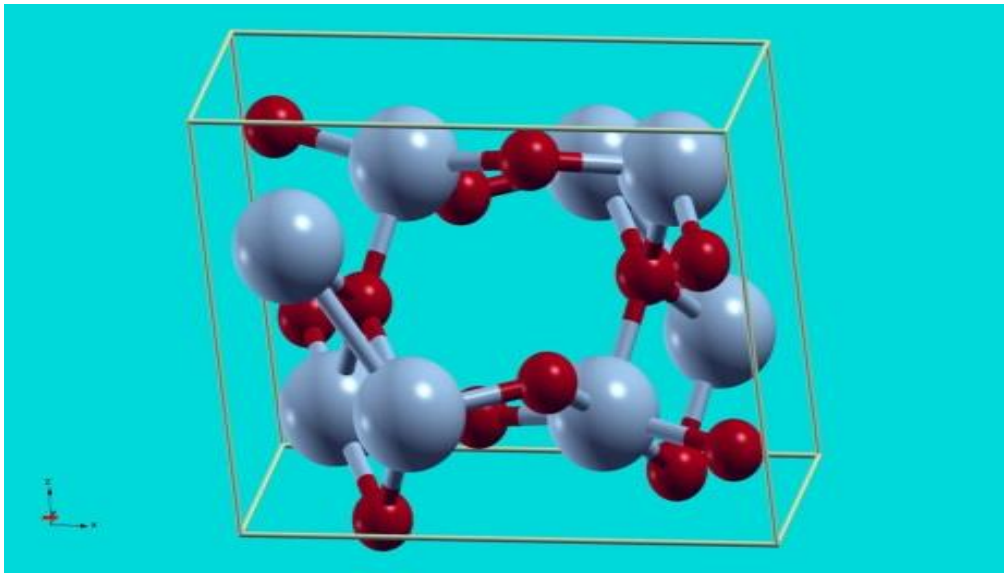

Figure 2.5 Insulating phase of V_2O_3: V atoms (grey) and O atoms (red) are shown.

Metallic phase of V_2O_3 has trigonal corundum structure with space group $R\bar{3}C(D_{3d}^6,\ No.167)$. Vanadium atoms are located in the trigonal lattice are located at the Wyckoff positions (4c): $\pm(x, y, z), \pm(\frac{1}{2} + x, \frac{1}{2} + y, \frac{1}{2} + z)$ with x = y = z = 0.3463 and oxygen atoms occupy the Wyckoff positions (6e): $\pm(x,\ \frac{1}{2} - y,\ \frac{1}{4})$; $\pm(\frac{1}{4},\ y,\ \frac{1}{2} - z)$;

$\pm(\frac{1}{2}-x,\ \frac{1}{4},\ z)$ with x = y = z = 0.56164 [99]. The primitive unit cell of the trigonal lattice is defined by following lattice parameters,

$$\mathbf{a_t} = a_t\left(1/2, -\frac{\sqrt{3}}{2}, \frac{c_t}{a_t}\right);\ \mathbf{b_t} = a_t\left(1/2, \frac{\sqrt{3}}{2}, \frac{c_t}{a_t}\right);\ \mathbf{c_t} = a_t(-1, 0, c_t/a_t) \tag{2.20}$$

with $a_t = 2.85875$Å and $c_t = 4.66767$Å. With these specifications, the crystal structure is visualized as shown in Figure 2.6.

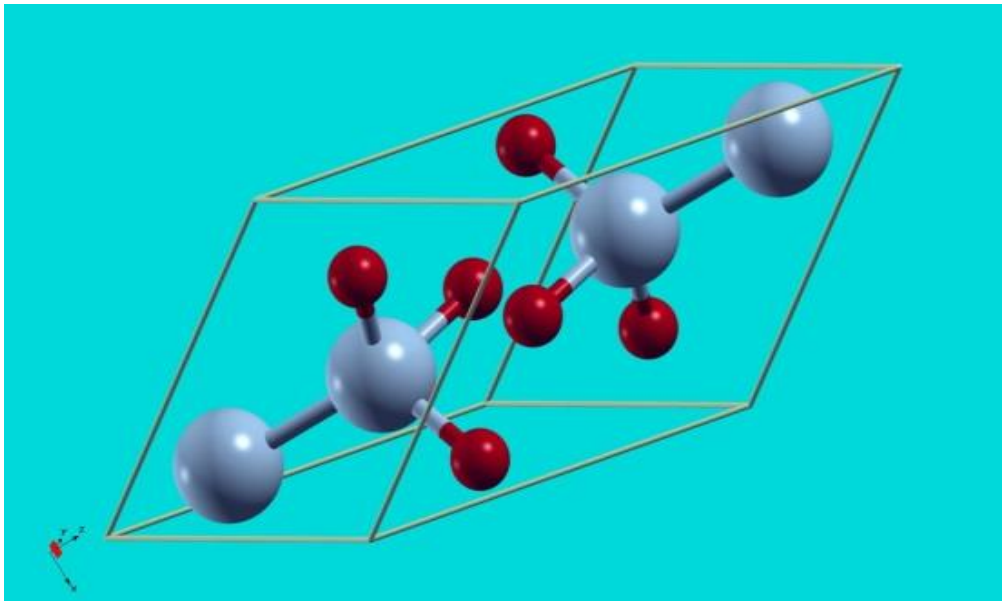

Figure 2.6 Metallic phase of V_2O_3: V atoms (grey) and O atoms (red) are shown.

2.7.3 Vanadium Pentoxide (V_2O_5)

The crystal structure of vanadium pentoxide consists of simple orthogonal lattice with space group $Pmmn(D_{2h}^{13},\ No.\ 59)$ and lattice constants for the primitive unit cell are given by [100],

$$a = 11.512Å;\ b = 3.564Å\ ;\ c = 4.368Å \tag{2.21}$$

Table 2.2 Wyckoff Parameters of V_2O_5: Simple Orthorhombic Lattice

Atom	Wyckoff positions	Parameters		
		x	y	z
V	(4f)	0.10118	0.25	-0.1083
O_1	(4f)	0.1043	0.25	-0.469
O_2	(4f)	-0.0689	0.25	0.003
O_3	(2a)	0.25	0.25	0.001

The structure consists of vanadium atom and three different types of oxygen atom; vanadium and two types of oxygen atom occupy the Wyckoff positions (4f): (x, 1/4, z), (-x+1/2, 1/4, z), (-x, 3/4, -z), (x+1/2, 3/4, -z) and the third type of oxygen atom occupies the Wyckoff positions (2a): (1/4, 1/4, z), (3/4, 3/4, -z) [101-104] where x, y, z are given in Table 2.2 [105]. Based on the crystal structure parameters, the unit cell was visualized as is shown in Figure 2.7.

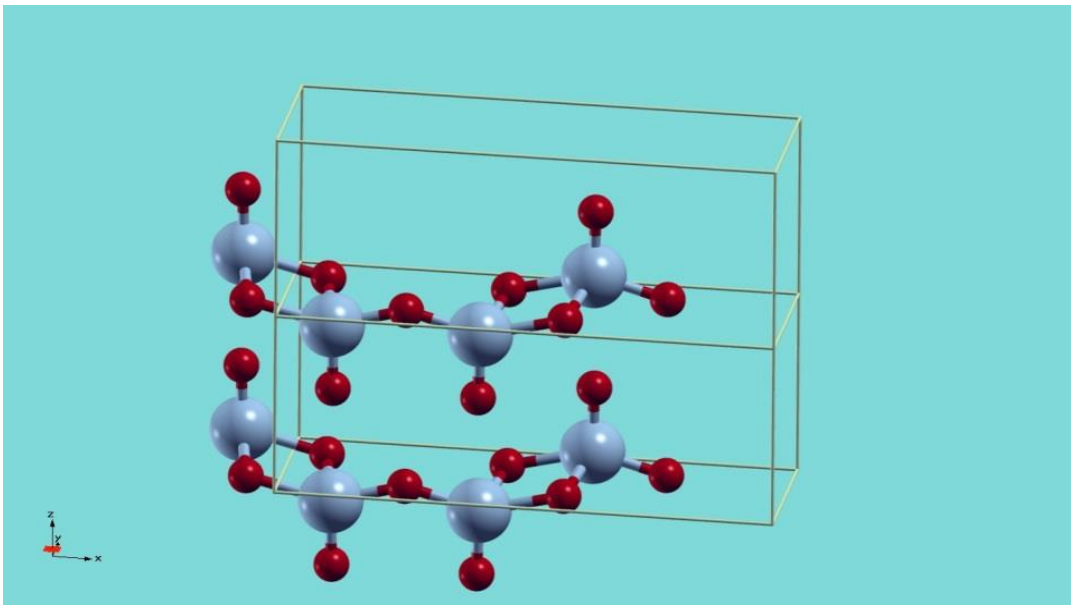

Figure 2.7 Crystal structure of V_2O_5: V atoms (grey) and O atoms (red) are shown.

2.8 Optimization of Unit Cell

Structure optimization in ABINIT can be done, at 1 atmosphere and 0K, using its input variable "optcell" (=2) which optimizes both cell shape and dimensions when "ions" are allowed to move using "ionmov" variable. Since the symmetry of the system is taken into account, effectively relevant degrees of freedom are optimized. In order to avoid the discontinuities (as a result of abrupt change in number of plane waves with cell size), suitable value of "ecutsm" has to be used. Keeping in mind that larger sphere of plane waves may be necessary during the optimization, proper value of "dilatmx" should be provided in the input file. In our calculation, dilatmx =1.14 was used, allowing the lattice parameters to change up to 14% from input values. Using ionmov=2, full variable cell relaxation was performed, using the Broyden-Fletcher-Goldfarb-Shanno (BFGS) minimization procedure.

The result of structural optimization is given in Tables 2.3. The differences between original and corresponding relaxed parameters are close to each other within 5% except the monoclinic structure of V_2O_3 and V_2O_5 in c direction, which show little more deviation but lie within 10%: which were defined a little further than their relaxed positions. Since overall the changes were very small, unit cells were defined with reasonable accuracy.

Table 2.3 Lattice Constants for Bulk VO_x

	Before relaxation	After relaxation
V_2O_5 (Simple Orthorhombic)		
Lattice Parameter (Angstrom)	a=11.512; b=3.564; c=4.368	a=11.695; b=3.546; c=3.951
Angle (Degree)	$\alpha = \beta = \gamma$ = 90	$\alpha = \beta = \gamma$ = 90
V_2O_3 (Trigonal corundum)		
Lattice Parameter (Angstrom)	a = b = c = 5.4735	a = b = c = 5.4673
Angle (Degree)	$\alpha = \beta = \gamma = 53.7843$	$\alpha = \beta = \gamma = 51.0410$
V_2O_3 (Monoclinic)		
Lattice Parameter (Angstrom)	a = 7.255; b = 5.002; c = 5.548	a = 7.431; b = 4.781; c = 5.166
Angle (Degree)	$\alpha = \gamma = 90$; β = 96.75	$\alpha = \gamma = 90$; β = 100.3311
VO_2 (Rutile)		
Lattice parameter (Angstrom)	a = b = 4.5546; c=2.8514	a = b = 4.5479; c= 2.7328
Angle (Degree)	$\alpha = \beta = \gamma$ = 90	$\alpha = \beta = \gamma$ = 90
VO_2 (Monoclinic)		
Lattice parameter (Angstrom)	a = 5.7517; b = 4.5378; c = 5.3825	a = 5.541; b = 4.527;c = 5.286
Angle (Degree)	$\alpha = \gamma = 90$; $\beta = 122.646$	$\alpha = \gamma = 90$; $\beta = 121.63$

2.9 Convergence Studies

The variables that mainly affect the convergence of ground state energy calculations in ABINIT are: density of k-points in first Brillouin zone and kinetic energy cut-off for plane waves. Figure 2.8 shows the variation of total energy, at gamma point, of vanadium oxides (per unit cell used in the calculations) as a function of cutoff energy. In our calculations, we have considered the value of the plane wave cutoff to be 40 Hartree.

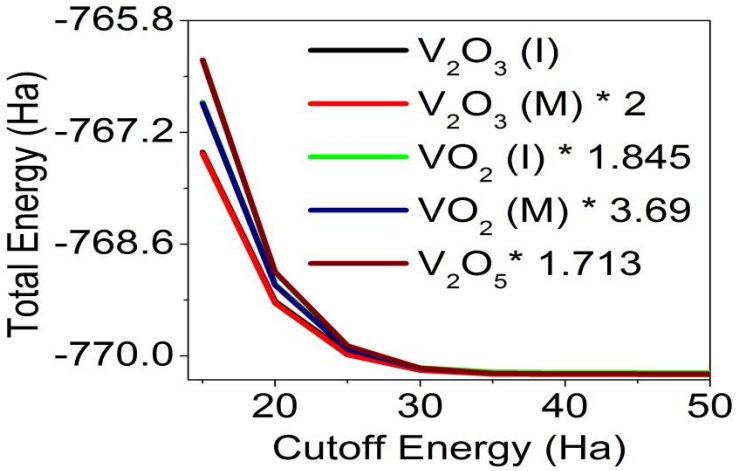

Figure 2.8 Variation of total energy, of vanadium oxides, with plane wave cutoff; scaled by multiplication factors as shown.

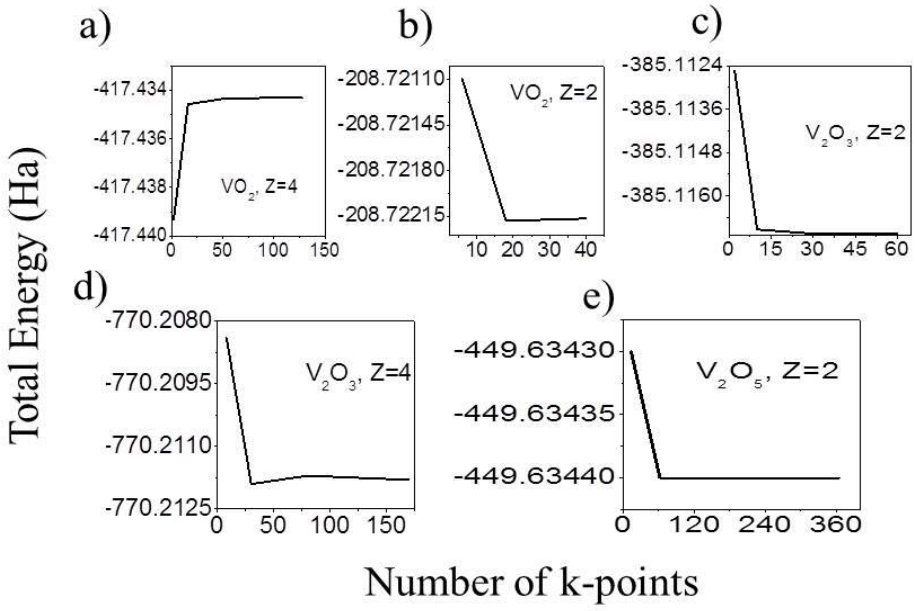

Figure 2.9 Variation of total energy, of vanadium oxides, with number of k-points.

Similarly, convergence tests were done to determine the optimum number of k-points required in the BZ; the number of k-points depends on whether the system is

metallic or not and, of course, the precision of the calculations. The metallic system usually requires more k-points than the insulating/semiconducting systems. In the present study, ground state calculations were performed with Monkhorst-Pack Grid having different k-point densities represented by 2×2×2, 4×4×4, 6×6×6 and 8×8×8 grids as shown in Figure 2.9. 6×6×6 grid is found to be appropriate for all the systems except V_2O_5, for which 4×4×4 is good enough.

2.10 BoltzTraP: Calculations of Boltzmann Transport Properties

BoltzTraP [106] is a program for calculating the semi-classical transport coefficients based on Boltzmann transport equations. The code performs smooth Fourier expansion of band energies, maintaining the space group symmetry. In the present study, the electron density from Self-Consistent Field (SCF) calculation was used as an input for Non-Self-Consistent (NSCF) calculation to obtain electronic structure on much finer grid (as compared to the SCF grid). The purpose of NSCF calculation, here, was to effectively reduce the time of transport coefficient calculations. Smooth highly resolved electronic bands, thus obtained, were processed using the BoltzTraP code. Transport properties were calculated using band energies with constant relaxation time approximation. Since the calculations are done at 0 Kelvin and 1 atmospheric pressure, temperature dependency in energy band is ignored. However, the electronic properties at higher temperature are simulated by applying Fermi distribution over electronic states.

$$f_0(\varepsilon) = \frac{1}{\left(e^{(\varepsilon-\varepsilon_F)/K_BT}\right)+1} \text{ (equilibrium F-D function)} \qquad (2.22)$$

Main transport properties studied are (a) electrical conductivity: Ohm's law, in the absence of magnetic field and thermal gradient (b) Seebeck coefficient (thermo-power) and (c) thermal (electronic) conductivity which are, respectively, given by equations (2.23), (2.25) and (2.26) [107]. Clearly, the transport coefficients are function of temperature (T) and chemical potential (μ).

$$\sigma_{\alpha\beta}(T;\mu) = \frac{1}{\Omega}\int \sigma_{\alpha\beta}(\varepsilon)\left[-\frac{\partial f_{\mu}(T;\varepsilon)}{\partial \varepsilon}\right]d\varepsilon \tag{2.23}$$

$$\sigma_{\alpha\beta}(\varepsilon) = \frac{e^2}{N}\sum_{i,k} T_{i,k}\ v_{\alpha}(i,k)v_{\beta}(i,k)\delta(\varepsilon - \varepsilon_{ik}) \tag{2.24}$$

$$S_{\alpha\beta}(T;\mu) = \frac{1}{\mathrm{eT}\Omega\,\sigma_{\alpha\beta}(T;\mu)}\int \sigma_{\alpha\beta}(\varepsilon)(\varepsilon-\mu)\left[-\frac{\partial f_{\mu}(T;\varepsilon)}{\partial \varepsilon}\right]d\varepsilon \tag{2.25}$$

$${K^0}_{\alpha\beta}(T;\mu) = \frac{1}{e^2\mathrm{T}}\int \sigma_{\alpha\beta}(\varepsilon)(\varepsilon-\mu)^2\left[-\frac{\partial f_{\mu}(T;\varepsilon)}{\partial \varepsilon}\right]d\varepsilon \tag{2.26}$$

where e is electronic charge, Ω is volume of unit cell, N is number of k-points sampled, v(k) is the band velocity, ε (k) is band energy and τ (k) is relaxation time. Due to the presence of delta function like factor, BoltzTraP considers transport electrons in a narrow energy range and relaxation time is practically same for such range [107].

CHAPTER 3

ELECTRONIC PROPERTIES OF VANADIUM OXIDES

3.1 General Considerations

In mean-field approximation, every electron in a crystal, with $> 10^{23}$ electrons/cm^3, experiences the same average potential V(**r**) and Schrödinger equation for each electron is given by,

$$\left(\frac{p^2}{2m} + \mathrm{V}(\mathbf{r})\right)\Phi_n(\mathbf{r}) = E_n\Phi_n(\mathbf{r}) \tag{3.1}$$

where, the one-electron Hamiltonian operates on wavefunction $\Phi_n(\mathbf{r})$ to yield energy of the electron in an eigenstate n (each of which can be occupied, at most, by two electrons of opposite spin – Pauli's exclusion principle). Using Bloch's theorem, the eigenstate of one particle Hamiltonian, can be written as the product of plane waves and a lattice periodic function,

$$\Phi_{nk}(\mathbf{r}) = e^{i\mathbf{k}.\mathbf{r}}\mathrm{u}_{nk}(\mathbf{r}) \tag{3.2}$$

Thus the wave function is indexed with a quantum number n and the wave vector **k**. A plot of the electron energies in (3.1) versus k is known as electronic band structure or "spaghetti plot". Each value of k has a discrete spectrum of states, labeled by band index n, the energy band numbering. The number of bands, in a band structure diagram, is equal to the number of atomic orbitals in the unit cell [108]. The overlap integral (overlap

between the interacting orbitals) determines the width of the band or band width or band dispersion, which is the difference in energy between the lowest and highest points in a band. The greater the overlap between neighboring unit cells, the greater is the band width and vice versa.

The wave vector k can take any value within the Brillouin zone. All the points in a Brillouin zone can be classified using the symmetry of the reciprocal lattice. Symmetric points or Lifschitz points [109], also called special/specific high symmetry points, are those points which remain fixed or transform into an equivalent one under a symmetry operation of the Brillouin zone. These points play a specific role in solid state physics: (a) if two k vectors can be transformed into each other due to some set of symmetry elements, electronic energies at those k-vectors must be identical; (b) "wave functions can be expressed in a form such that they have definite transformation properties under symmetry operations of the crystal" [110]. Similarly, we can define symmetric lines and planes in the Brillouin zone. Customarily, high symmetry points and lines inside the Brillouin zone are denoted by Greek letters while those on the surface are denoted by Roman letters. The center of a Brillouin zone is always denoted by Greek letter Γ.

The behavior of electrons in a solid can be studied microscopically from its electronic band structure [110]. One can extract important information about a material such as its stability, transport coefficients, optical properties, and intra as well as intermolecular bonding interactions from the band structure diagrams. Since electronic band structure of a material is dependent on the crystal structure, it (band structure) can be considered as a link between crystal structure and physical properties.

Experiments have been performed to investigate the electronic structure of vanadium oxides through photoemission and x-ray absorption spectroscopy. The studies have revealed that the electronic structure of these three oxides of vanadium, VO_2, V_2O_3 and V_2O_5, is characterized by a strong hybridization between the 2p (O) and 3d (V) bands. It has been found that the hybridization energy exceeds both the coulomb repulsion energy of two 3d electrons (U_{dd}) and the energy required to transfer an electron from a ligand orbital (e.g., 2p (O)) to 3d (V) orbital, i.e., the charge transfer energy [111]. It is the hybridization that determines the shape of the valence band [112, 113].

3.2 Electronic Band Structure of Bulk V_2O_5

Figure 3.1 shows the electronic band structure and density of states of bulk V_2O_5 calculated by ABINIT. The variable "acell" was set to the theoretical value of 21.7545, 6.7350, 8.2543 Bohr [100] and 76 bands were computed by solving Kohn-Sham equation for uniformly spaced k points, at least 12 k points along each symmetry line, using the variable "ndivsm = 12". Occupation option was chosen such that all k points have the same number of bands and the same occupancies of the band. The electron density from SCF calculation (data set number 1) was used as an input for NSCF calculation (data set number 2) and hence the potential used for Kohn-Sham equation does not vary during the k-point scanning. The variable "tolwfr=10^{-12}" was used as a tolerance criterion for non-self-consistent calculations in ABINIT, which is tolerance on wavefunction squared residual. However, not all bands can be converged within the specified tolerance. By default, two upper bands constitute such "buffer" bands. Since buffer allows reaching the convergence of important non-buffer bands, the number of bands can be increased, for instance, by 2 so as to achieve the same convergence for all bands. The following high

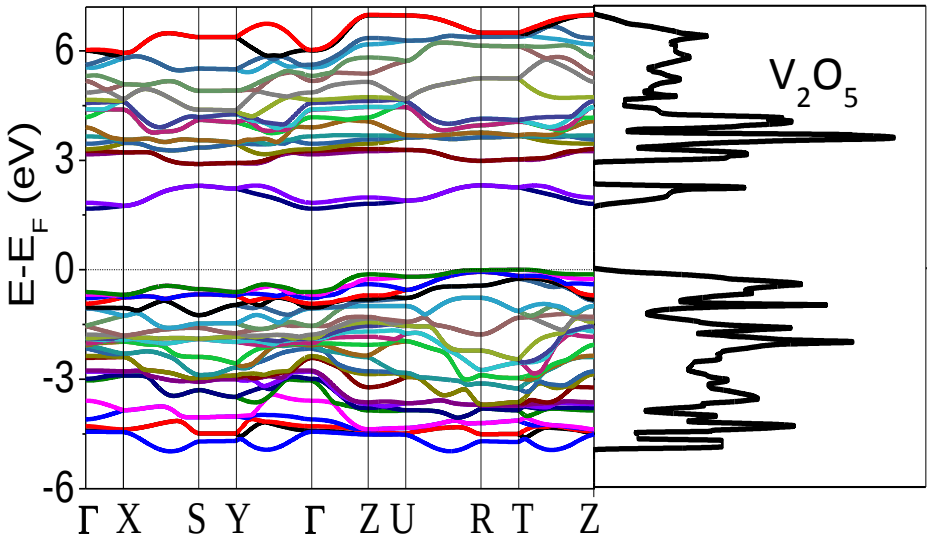

Figure 3.1 Electronic band structure and density of states for bulk V_2O_5.

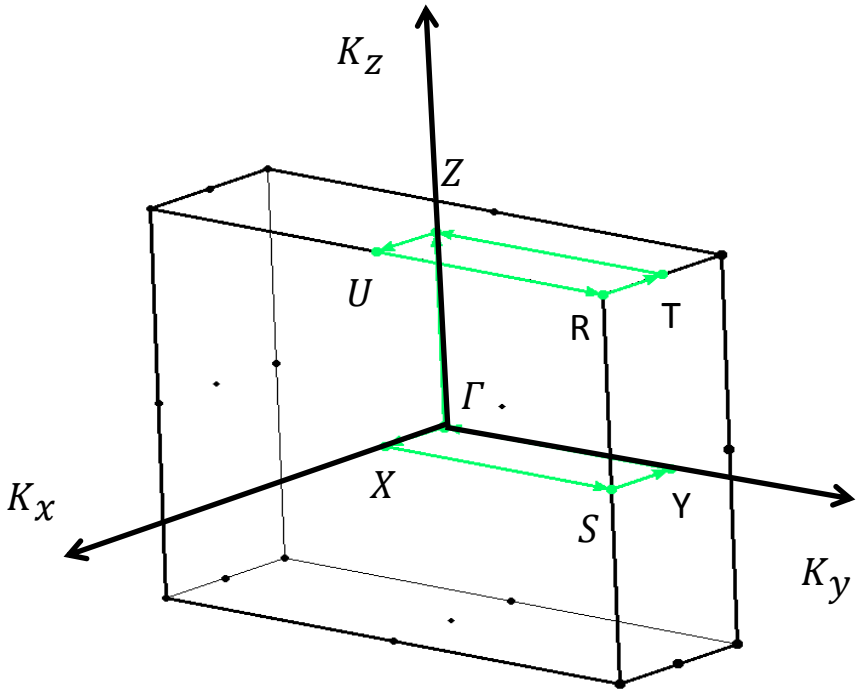

Figure 3.2 Definition of high symmetry points and lines in BZ for bulk V_2O_5.

symmetry points, specified in reduced coordinates within the first Brillouin zone, were chosen in the calculations: Γ (0, 0, 0), X (0.5, 0, 0), S (0.5, 0.5, 0), Y (0, 0.5, 0), Γ (0, 0, 0), Z (0, 0, 0.5), U (0.5, 0, 0.5), R (0.5, 0.5, 0.5), T (0, 0.5, 0.5) and Z (0, 0, 0.5) as indicated in Figure 3.2. XCrySDen [98] was used for the visualization of Brillouin Zone.

The Fermi energy obtained at the end of SCF calculations, in bulk V_2O_5, is 1.62 eV; the origin is shifted by this amount as shown by the horizontal dotted line in the band structure plot. The Fermi level corresponds to the highest occupied band. As the number of valence electron bands (as opposed to core electron bands considered in the pseudopotential) is equal to one half the number of the "valence electrons" in the unit cell (i.e., 2×13+5×6=56 but only 30 are shown in the Figure 3.1 and other 26 bands, not shown, range from -62.1 eV to -15.4 eV) and the rest, 18+2=20, bands correspond to the conduction band. Sometimes the two bands appearing around 2 eV are also called intermediate bands. These (intermediate) bands, with narrow band width 0.65 eV(≈ 0.75 eV [114]) separated from higher conduction band by 0.58 eV (≈ 0.6 eV [114]), can make significant contribution to transport phenomena or mediate optical transitions from valence to higher conduction bands. Also, not shown in the Figure are the 4s like bands which lie at a much higher energy. Bands appearing at -62.1 and -15.4 eV correspond to V3s and O2s, respectively. Some other bands appearing at -37.1 eV correspond to V3p. Valence-top bands (5 eV wide ≈ 5.1 eV [114]) comprise of mainly O2p states (total of 30: p orbitals consist of three states per oxygen atom and there are ten oxygen atoms in the unit cell) plus some contribution from V3d states. Similarly, conduction-bottom bands (5.3 eV wide) consist of empty V3d states (total of 20: d orbitals consist of five states per vanadium atom and there are four vanadium atoms in the unit cell) hybridized

Table 3.1 Band Structure of V_2O_5: Comparison Table

	Present calculation	Comparison with remark (Remark)	
Band gap	1.7 eV (indirect: $\Gamma - T$)	1.74 eV (indirect : $\Gamma - T$)	Similar calculation [105]
		1.6 eV (indirect: $\Gamma - R$)	Similar calculation [94]
		2.2 eV (indirect)	Experiment [105]
V3s bands	4 bands (~ appearing at -62.1 eV)	N/A	Not shown in Figure
V3p bands	12 bands (~ appearing at -37.1 eV)	N/A	Not shown in Figure
O2s bands	10 bands (~ appearing at -15.4 eV)	N/A	Not shown in Figure
Valence bands (mainly O2p)	30 bands (width: 5 eV)	30 bands (width: 5.1 eV)	Similar calculation [114]
Conduction bands (mainly V3d)	20 bands (width: 5.3 eV)	20 bands	Similar calculation [105]
Intermediate bands	~ 2 eV (width: 0.65 eV)	~ 2 eV (width: 0.75 eV)	Similar calculation [114]
		Width: 0.45 eV	Experiment [115]
	0.58 eV below higher band	0.6 eV below higher band	Similar calculation [114]
		0.35 eV below higher band	Experiment [115]
"Valence electrons" considered by PPs	56×2=112 electrons	-----	-----
Number of bands calculated	76 bands	-----	-----

with O2p states, the bonding oxygen orbitals with higher energy (as compared to anti-bonding counterpart). Triply degenerate t_{2g} and doublet e_g states, separated from each other by the crystal-field, are located at the lower edge of the conduction band and higher energies, respectively. All the degeneracies involved in t_{2g} and e_g states are lifted eventually because the octahedral coordination in V_2O_5 suffers strong deviation [105]. The density of electronic states (DOS) for V_2O_5 is shown on the right side of Figure 3.1. As can be seen in Figure 3.1, the most bonding part of the d band is split-off from the d band spectrum and the optical band gap is the difference in energy between the top of the O2p band and the bottom of the split-off part of the V3d band [116]. An indirect band gap of 1.7 eV is observed between T-point of the valence band to the Γ-point of the conduction band which is smaller than the experimental value of 2.2 eV [105]. It is to be noted here that this result is consistent with the reported band gap (1.74 eV) of Eyert and Höck [105]. This underestimation of the band gap is an inherent problem in determining band-gap using the DFT formalism. For convenience, the analyses of band structures of bulk V_2O_5 are summarized in Table 3.1 and are compared with the literature.

It is also seen from Figure 3.1 that the bands are dispersive to a varying extent. Bands are relatively flat (narrow band width) along Γ-X while larger dispersions (wide band width) are observed along Γ-Y and Γ-Z directions, for instance. This is a clear indication of anisotropies of the crystal structure. Disperse bands are indication of hybridization: the more the bands are dispersive, the stronger is the hybridization and vice-versa [117]. In general, the DOS is proportional to the inverse of the slope of the "band structure". Conduction bands below 4.7 eV are relatively flat which is also confirmed by the peaks in the DOS in the corresponding energy range. Bands along X-S,

S-Y, U-R and R-T are doubly degenerate throughout the energy range and the rest are non-degenerate.

3.3 Electronic Band Structure of Bulk VO_2

Figure 3.3 shows the electronic band structure and the DOS of bulk VO_2 in its metallic rutile phase. The following high symmetry points, specified in reduced coordinates within the first Brillouin zone, were chosen in the calculations: Γ (0, 0, 0), X (0, 0.5, 0), R (0 0.5 0.5), Z (0, 0, 0.5), Γ (0 0 0), R (0, 0.5, 0.5), A (0.5, 0.5, 0.5), Γ (0, 0, 0), M (0.5, 0.5, 0), A (0.5, 0.5, 0.5) and Z (0, 0, 0.5) as indicated in Figure 3.4. As usual, origin was shifted by 7.47 eV, the Fermi energy, as shown by the horizontal dotted line in the band structure plot. Out of the computed 35 bands, the first 24 [(1×13+2×6)-1=24] were fully occupied while the rest were either partially occupied or unoccupied. The Fermi level passes through partially occupied bands with indices 25-28, where the band with index 25 corresponds to the valence electrons (as opposed to core electrons considered in the pseudopotential). This is a clear indication of finite overlapping of valence and conduction bands, a factor that characterizes metallic behavior. We mainly observed seven groups of bands but the first three groups lying around -63 eV, -38 eV and -18 eV, not shown in the figure, are due to V3s, V3p and O2s states, respectively. These are less important in our discussion because they are very tightly bound. The rest of the four groups of bands lie below (one), at (one) and above (two) the Fermi energy. Out of the four groups, the first one lying between -7.6 and -1.6 eV (energy range = 6 eV [118]) consists of 12 bands and are mainly due to O2p states. The second group which starts at 6.8 eV is due to V4s states. The third and fourth groups consisting of 6 and 4 bands, in the ranges from -0.6 to 2.0 eV and from 2.2 to 5.1 eV, respectively, are mainly from V3d states and some contribution

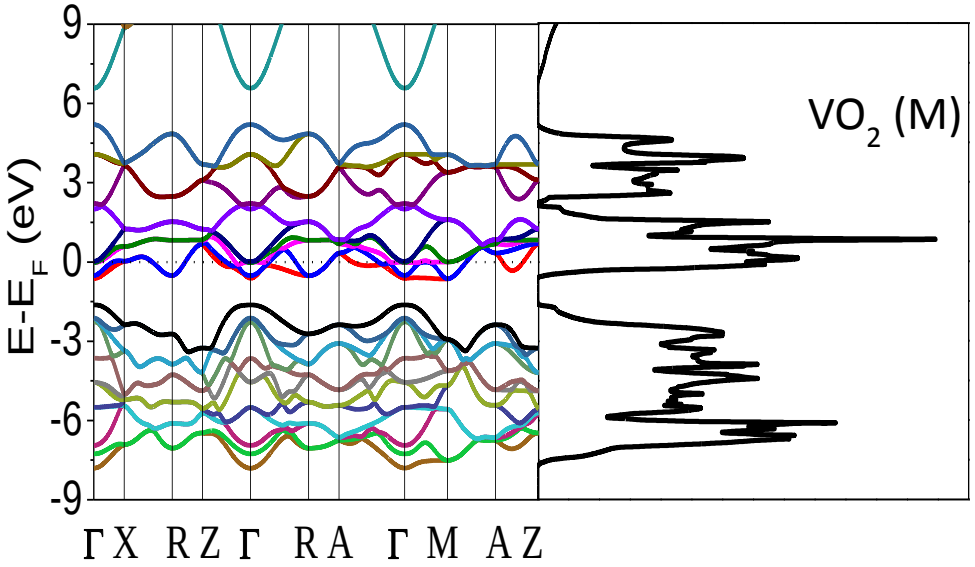

Figure 3.3 Electronic band structure and density of states for bulk VO_2 rutile structure.

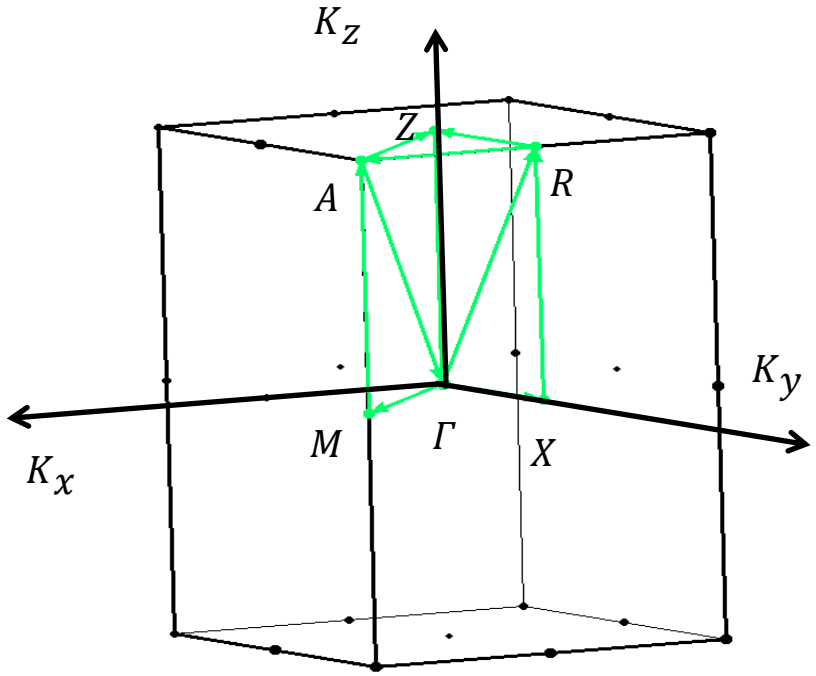

Figure 3.4 Definition of high symmetry points and lines in BZ for VO_2 rutile structure.

from O2p states as a result of the p-d hybridization. The groups of bands discussed above can be more clearly understood from the following picture of crystal field splitting.

It is known that nearly octahedral crystal field partially lifts the degeneracy of the d orbitals yielding two sets of bands: t_{2g} and e_g^{σ} (total of 10 bands, the sum of bands in the third and the fourth groups mentioned in the previous paragraph). Further, the tetragonal crystal field splits triply degenerate t_{2g} states, containing the single d electron, into an a_{1g} state and e_g^{π} doublet (which are also called $d_{\parallel}$ and π^*, respectively in the literatures) [22] as shown in Figure 3.5 (b). The Fermi level passes through partially occupied e_g^{π} and a_{1g} bands. Octahedral distortions can be measured in terms of t_{2g}- e_g configuration mixing [97]. In the case of insulating, monoclinic (M_1) phase, a_{1g} further splits into lower and upper a_{1g} bands as shown in Figure 3.5 (a), which are, respectively, called lower and upper Hubbard band, in the Mott picture while bonding (lower) and anti-bonding (upper) bands in the Peierls model [118]. This latest splitting has been explained by metal-metal pairing in the vanadium chains [99].

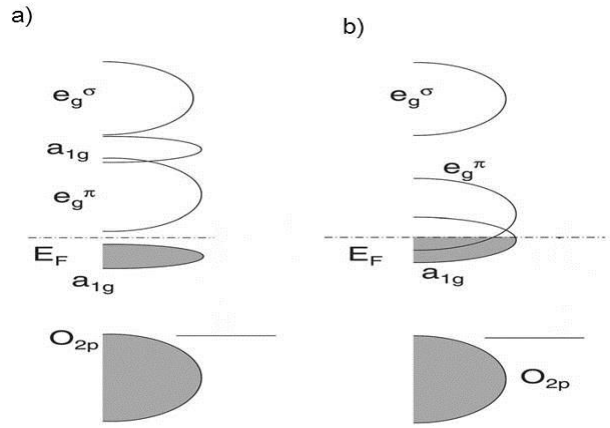

Figure 3.5 Schematic energy diagrams of the V3d and O2p states at the (a) insulating and (b) metallic phases of VO_2 [118].

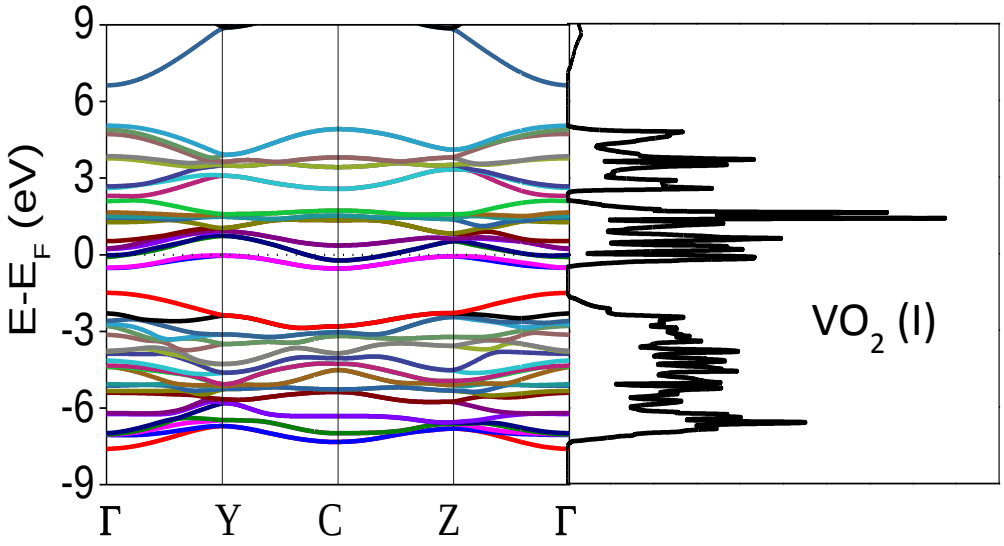

Figure 3.6 Electronic band structure and density of states for bulk VO_2 monoclinic (M_1) phase.

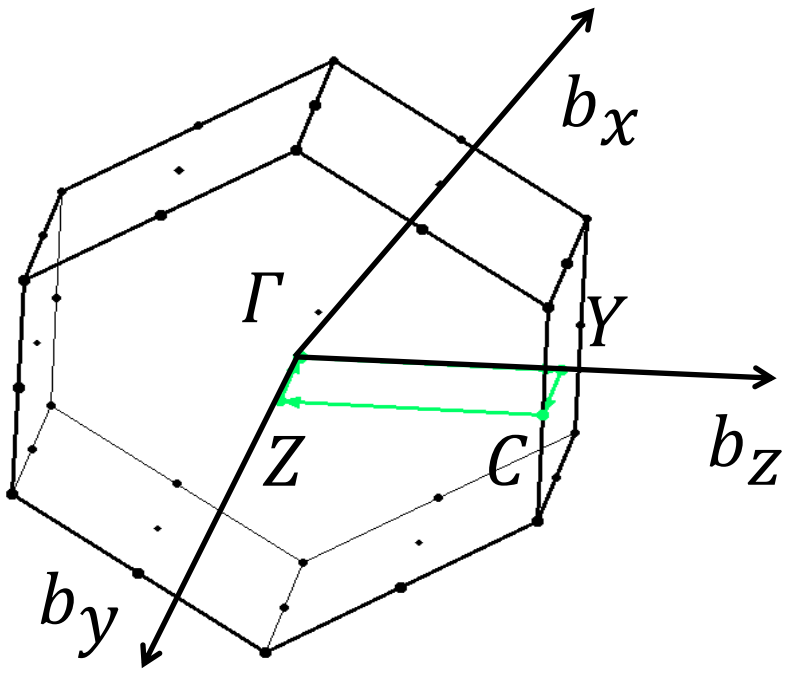

Figure 3.7 Definition of high symmetry points and lines in BZ for VO_2 monoclinic (M_1) phase.

Figure 3.6 shows the electronic band structure and density of states of bulk VO_2 in its monoclinic (M_1) insulating phase. The following high symmetry points, specified in reduced coordinates within the first Brillouin zone, were chosen in the calculations: Γ (0, 0, 0), Y (0, 0, 0.5), C (0, 0.5, 0.5), Z (0, 0.5, 0), Γ (0, 0, 0) as indicated in Figure 3.7. As usual, the origin was shifted by 7.44 eV, the Fermi energy, as shown by the horizontal dotted line in the band structure plot. Out of 69 bands that were computed, the first fifty [2×(1×13+2×6)=50] are fully occupied; the band with indices 51 and 52 are partially occupied and the rest are unoccupied. The number of band-groups in the insulating phase is exactly the same as in the metallic phase. They appear in similar locations as in the metallic phase and hence can be interpreted with same arguments. One difference is that the number of bands in each group is doubled in the insulating phase, which is consistent with the fact that the number of formula units in the real space primitive unit cell doubles during the phase transition. The fact that electronic states are present at the Fermi Level indicates the shortcomings of LDA in reproducing the observed optical gap of 0.6 eV [3]. However, some differences in the bands properties can be clearly seen in the insulating phase: (a) number of bands crossing the Fermi level is less, with smaller amount of overlapping between valence and conduction bands (b) bands corresponding to "valence electrons" considered in the pseudopotential are fully occupied, unlike in the metallic phase, as shown in Figure 3.8. For convenience, the analyses of band structures of bulk VO_2 are summarized in Table 3.2 and are compared with the literature.

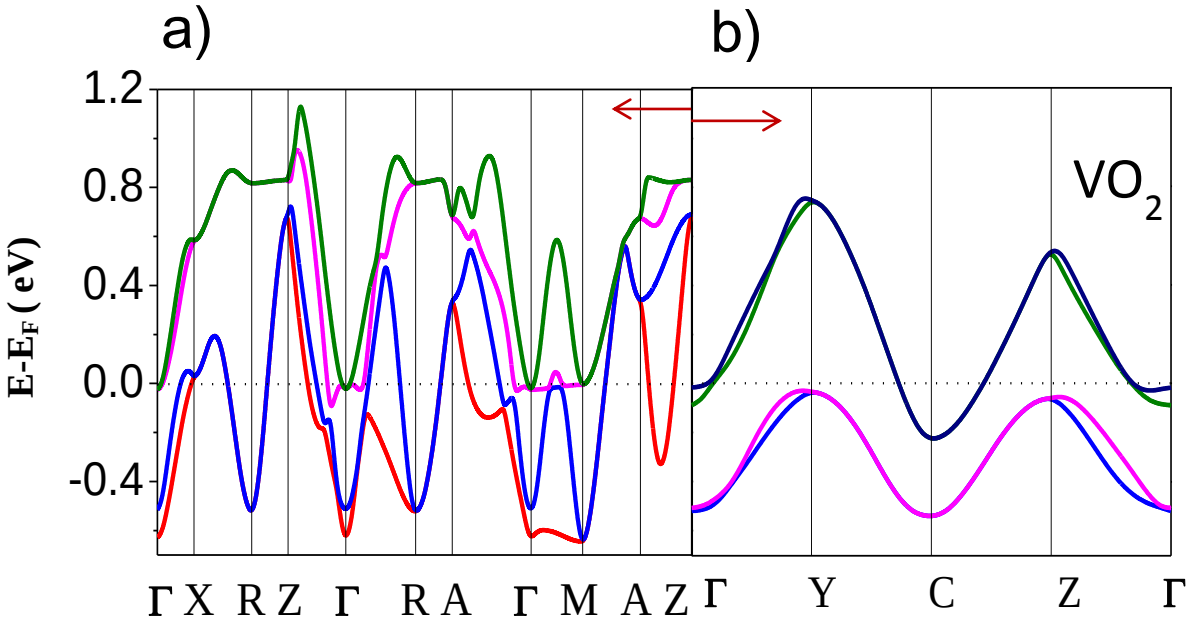

Figure 3.8 (a) Metallic phase and (b) insulating phase of bulk VO_2 at Fermi level.

Table 3.2 Band Structure of VO_2: Comparison Table

	Present calculation			Comparison with remark (Remark)	
Band gap	M	0		0	Metal
	I	0		0.6 eV	Experiment [119]
				0	Similar calculation [120]
V3s bands	M	2 bands	Appearing at ~ -63 eV	N/A	Not shown in Figure
	I	4 bands		N/A	Not shown in Figure
V3p bands	M	6 bands	Appearing at ~ -38 eV	N/A	Not shown in Figure
	I	12 bands		N/A	Not shown in Figure
O2s bands	M	4 bands	Appearing at ~ -18 eV	N/A	Not shown in Figure
	I	8 bands		N/A	Not shown in Figure
Valence bands (mainly O2p)	M	12 bands	Width: 6 eV	Width: 6 eV	Experiment [118]
				Width: 5.4 eV	Similar calculation [97]
	I	24 bands	Width: 6 eV		
Conduction bands (mainly V3d)	M	Two groups: 6 bands: t_{2g} 4 bands: e_g	From -0.6 to 2.0 eV & From 2.2 to 5.1 eV	from -0.6 to 2.0 eV & from 2.0 to 5.5 eV	Similar calculation [97]
	I	20 bands	Similar location as in metallic case		
Upper conduction bands (V4s)	M	2 bands	Starting at 6.8 eV	N/A	
	I	4 bands			
"Valence electrons" considered by PPs	M	50 electrons	----	----	----
	I	100 electrons	----	----	----
Number of bands calculated	M	35 bands	-----	-----	----
	I	69 bands	----	-----	----

3.4 Electronic Band Structure of Bulk V_2O_3

Figure 3.9 shows the electronic band structure and density of states of bulk V_2O_3 in its metallic corundum phase. The following high symmetry points, specified in reduced coordinates within the first Brillouin zone, were chosen in the calculations: Γ (0, 0, 0), L (0, -0.5, 0), Z (0, 0, 0.5), F (0.5, 0, 0.5), Γ (0, 0, 0) and Z (0, 0, 0.5) as indicated in Figure 3.10. As usual, the origin was shifted by 9.2 eV, the Fermi energy, as shown by the horizontal dotted line in the band structure plot. Out of 61 computed bands, the first 42 were fully occupied while the rest were either partially occupied or unoccupied. The Fermi level passes through partially occupied bands with indices 43-47, where the bands with indices 43 and 44 correspond to the valence electrons (as opposed to core electrons considered in the pseudopotential). This is a clear indication of finite overlapping of valence and conduction bands, a property that indicates metallic behavior. The V3s, V3p and O2s states appear in similar locations as in VO_2 but are not important for our purpose because they are tightly bound. By excluding these groups of bands, we can now see, mainly, four groups of bands as in VO_2. The first one lying between -8.0 and -3.6 eV (energy range ≈ 4.0 eV [121]) consists of 18 bands and are mainly due to O2p states. The second group which starts at 4 eV, consistent with the work of Mattheiss [121], is due to V4s states. The third and fourth groups consisting of 12 and 8 bands, in the ranges from -1.23 to 1.4 eV and from 1.94 to 3.7 eV, respectively, are mainly from V3d states and some contribution from O2p states as a result of p-d hybridization. The magnitude of the p-d hybridization is same as found for VO_2 [99]. The groups of bands, discussed above, can be more clearly understood from the following picture of crystal field splitting (Figure 3.11).

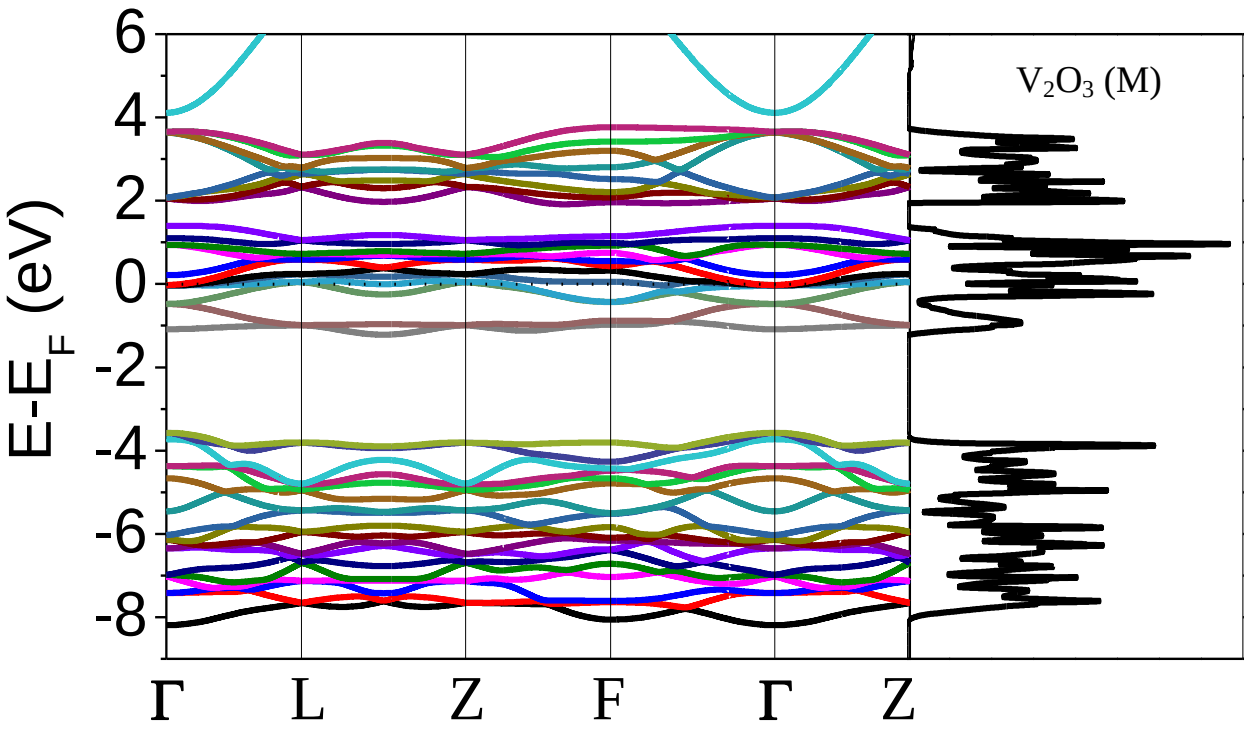

Figure 3.9 Electronic band structure and density of states for bulk V_2O_3 metallic phase.

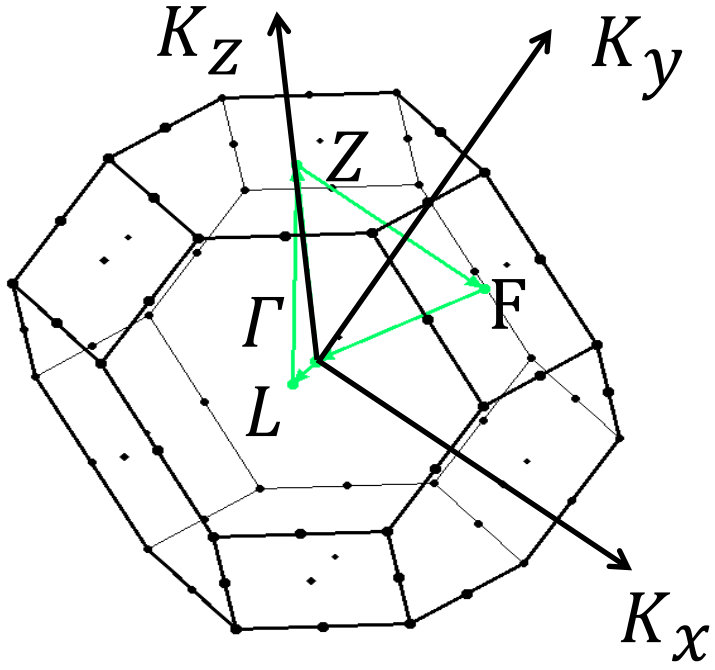

Figure 3.10 Definition of high symmetry points and lines in BZ for V_2O_3 metallic phase.

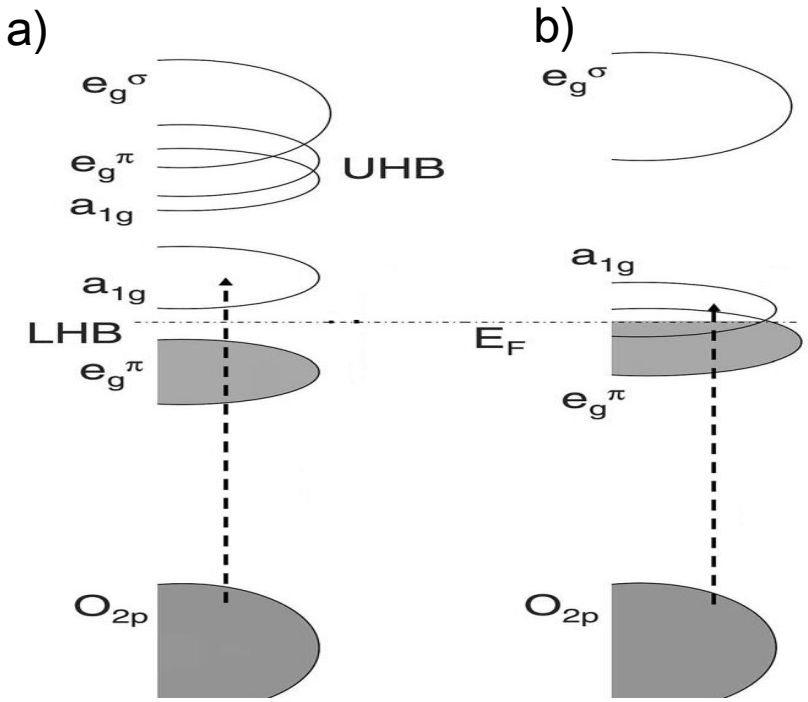

Figure 3.11 Schematic energy diagrams of the V3d and O2p states at the (a) insulating and (b) metallic phases in V_2O_3 [118], LHB and UHB are lower and upper Hubbard bands, respectively.

As in the case of VO_2, the crystal field due to the oxygen octahedra (VO_6) splits d orbitals into two sets of bands: t_{2g} (lower band) and e_g^σ (upper band). The upper band e_g^σ is twofold degenerate and consists of d_{xz} and d_{yz} bands. This oxygen octahedron is not perfect but has trigonal distortion. The influence of non-cubic arrangement of distant metal ions in the lattice, combined with the trigonal distortion, split the three fold degenerate t_{2g} orbitals into a_{1g} singlet ($d_{3z^2-r^2}$) and two fold degenerate e_g^π bands (d_{xy}, $d_{x^2-y^2}$) [122] as shown in Figure 3.11 (b). In the case of monoclinic phase, lower symmetry of the crystal field (due to structural change during phase transition) further lifts the degeneracy between two e_g^π bands as shown in Figure 3.11 (a) [118, 122, 123]. In this

model, the antiferromagnetic insulating (AFI) phase remains in Hund's rule (maximum spin) configuration $e_g^{\uparrow\uparrow}$, leaving a_{1g} band empty (putting V $3d^2$ ions in the S = 1 state). This is contrary to the one-band Hubbard model, where one V electron enters bonding a_{1g} orbital state and the other enters the doubly degenerate e_g^{π} state (S=1/2 on each V site) [123].

Figure 3.12 shows the electronic band structure and density of states of bulk V_2O_3 in its monoclinic insulating phase. The following high symmetry points, specified in reduced coordinates within the first Brillouin zone, were chosen in the calculations: Γ (0,0, 0), Y (0.5, 0, 0), C (0.5, 0.5, 0), Z (0, 0.5, 0) and Γ (0, 0, 0), as indicated in Figure 3.13. As usual, the origin was shifted by 9.2 eV, the Fermi energy, as shown by the horizontal line at zero energy. Out of the 121 bands that were computed, the first eighty-eight [2×(2×13+3×6)=88] are fully occupied; the band with indices 89, 90 and 91 are partially occupied and the rest are unoccupied. The number of band-groups in the insulating phase is exactly the same as in the metallic phase. They appear in similar locations as in the metallic phase and hence can be interpreted with same arguments. One difference is that the number of bands in each group is doubled in the insulating phase, which is consistent with the fact that the number of formula units in the real space primitive unit cell doubles during the phase transition. The fact that electronic states are present at the Fermi Level indicates the shortcomings of LDA in reproducing the observed optical gap of 0.66 eV [124]. However, some differences in the band properties can be clearly seen in insulating phase: (a) number of bands crossing the Fermi level is less (b) bands corresponding to "valence electrons" considered in the pseudopotential are fully occupied, unlike in the metallic phase as shown in Figure 3.14. For convenience, the analyses of band structures of bulk V_2O_3 are summarized in Table 3.3 and are compared with the literature.

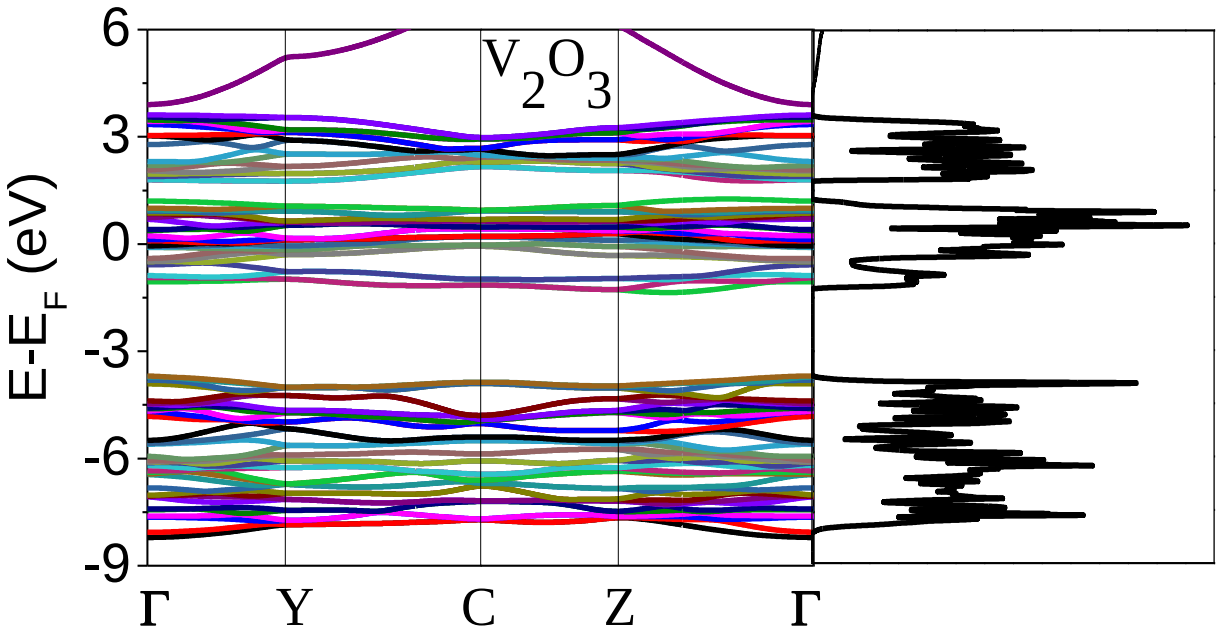

Figure 3.12 Electronic band structure and density of states for bulk V_2O_3 in insulating phase.

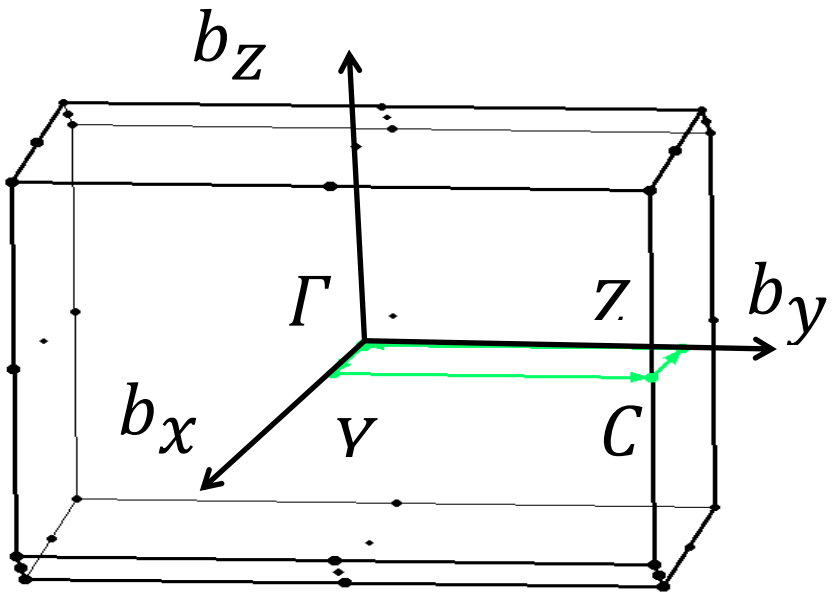

Figure 3.13 Definition of high symmetry points and lines in BZ for V_2O_3 insulating phase.

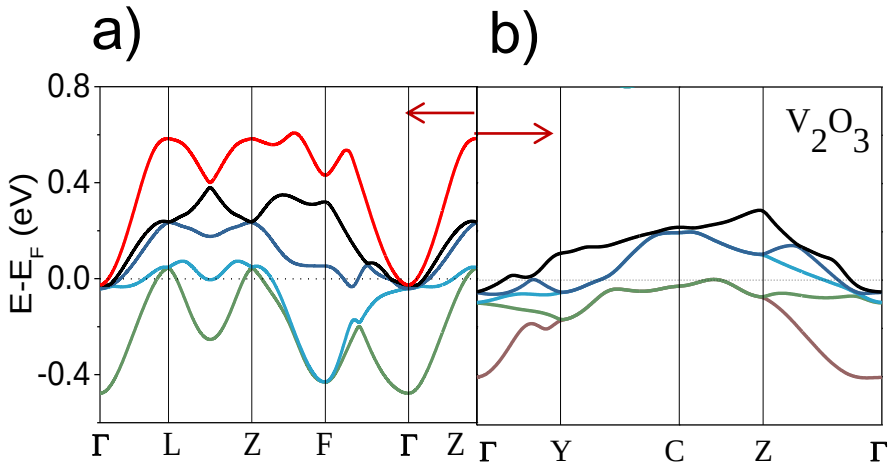

Figure 3.14 (a) Metallic phase and (b) insulating phase of V_2O_3 at Fermi level.

Table 3.3 Band Structure of V_2O_3: Comparison Table

	Present calculation			Comparison with remark (Remark)	
Band gap	M	0		0	Metal
	I	0		0.66 eV	Experiment [123]
				0	Similar calculation [125]
V3s bands	M	4 bands	Appearing at similar location as in VO_2	N/A	Not shown in Figure
	I	8 bands		N/A	Not shown in Figure
V3p bands	M	12 bands	Appearing at similar location as in VO_2	N/A	Not shown in Figure
	I	24 bands		N/A	Not shown in Figure
O2s bands	M	6 bands	Appearing at similar location as in VO_2	N/A	Not shown in Figure
	I	12 bands		N/A	Not shown in Figure
Valence bands (mainly O2p)	M	18 bands	Width: 4.4 eV	Width: 4.0 eV	Calculation [121]
	I	36 bands	Width: 4.4 eV		
Conduction bands (mainly V3d)	M	Two groups: 12 bands: t_{2g} 8 bands: e_g	From -1.2 to 1.4 eV & From 1.9 to 3.7 eV		
	I	40 bands	Similar location as in metallic case		
Upper conduction bands (V4s)	M	4 bands	Starting at 4.1 eV	N/A	Starting at 4 eV [121]
	I	8 bands			
"Valence electrons" considered by PPs	M	88 electrons	----	----	----
	I	176 electrons	----	----	----
Number of bands calculated	M	61 bands	-----	-----	----
	I	121 bands	----	-----	----

3.5 Summary

In this chapter, we have summarized the findings of our LDA one-electron, Kohn-Sham band-structure calculations of bulk vanadium oxides in both insulating and metallic phase. Electronic band structures depend on the crystal structure and contribute to stability, bonding interactions and physical properties such as transport and optical properties. Band structures, obtained in our study, are consistent with similar studies in the literatures. Band structures are found to be influenced by crystal field and the strong hybridization between 2p (O) and 3d (V) bands.

Bands in V_2O_5 are remarkably dispersive to different extent, along various high symmetry lines in the Brillouin zone (BZ). This implies that the crystal structure is highly anisotropic. A group of conduction bands (with narrow band width, called intermediate bands), lying close (0.6 eV apart) to higher conduction bands observed in V_2O_5, seem to play an important role in a variety of device applications. An indirect gap of 1.7 eV is observed between T and Γ points of the BZ, which is close to the value of 1.74 eV reported in the literature [105].

Similar calculations are done in both metallic and insulating phases of bulk vanadium dioxide (VO_2) and sesquioxide (V_2O_3). In the metallic phase, we see finite overlapping of valence and conduction bands. Bands in the insulating phases appear in similar locations as in corresponding metallic phases. The number of bands is doubled in the insulating phases (as compared to corresponding metallic counterpart), which is consistent with the fact that the number of formula units of the unit cell, in the calculations, is doubled in each of the oxides as the materials transition from metallic to insulating phase. Even though an optical gap is not observed in the insulating phase

(shortcomings of LDA), we have noticed some differences in the band structures that characterize phase- whether insulating or metallic. In insulating phase, (a) number of bands crossing the Fermi level is less; (b) bands corresponding to “valence electrons” considered in the pseudopotential are fully occupied, unlike in the metallic phase.

CHAPTER 4

THERMOELECTRIC PROPERTIES OF VANADIUM OXIDES

4.1 General Considerations

Boltzmann Transport Equation (BTE) is a semi-classical transport equation: quantum mechanics is embedded in the electronic band structure but the equation of motion for electrons is written in momentum space that looks like Newton's equation of motion,

$$\frac{d(\hbar\vec{k})}{dt} = -\nabla_r E_c(\vec{r}) = -q\vec{E}(\vec{r}) \tag{4.1}$$

where, $\vec{E}(\vec{r})$ = electric field; $E_c(\vec{r}) =$ bottom of conduction band. Here, the force is due to the electric field in the sample. The solution to equation (4.1) yields time dependent momentum coordinate. Similarly, the velocity of an electron is obtained from the band structure,

$$\overrightarrow{v_g}(t) = \frac{1}{\hbar}\nabla_k E[\vec{k}(t)] \tag{4.2}$$

and its solution gives the position of the particle with time. With these two solutions, the electrons can be tracked in phase space (this proves the semi classical nature of the approach because both momentum and position of a particle cannot be specified quantum mechanically). There are some assumptions considered in the Boltzmann approach such as: variation of bottom of the conduction band with space is slow so that quantum

mechanical reflections are not considered. This is a single particle approach but many body effects are treated. We include the effects of scattering (collision) but we consider the scattering to be very short in time duration such that the electrons' positions do not change during those events. It is the scattering or source term, in the second order, linear, non-homogeneous differential Equation (4.3), that imposes difficulty in finding analytical solution. In other words, these scattering phenomena are complicated and hence some approximation techniques need to be adopted to obtain analytical solutions. One of the widely used approximations is the relaxation time approximation (RTA) which considers a constant averaged (momentum) relaxation time, τ_m, for the electrons. The basic idea in RTA is that the effect of collision is to take a small perturbation and to react in a negative way to try to pull the system back to equilibrium. In other words, if the system is perturbed, it will decay back to equilibrium as: $\sim e^{-t/\tau_m}$. Within RTA, the BTE can be written as,

$$\vec{v}.\nabla_r f - q\vec{E}.\nabla_p f = -\frac{\delta f(\vec{p})}{\tau_m} \tag{4.3}$$

where, f = f(r,p,t) is occupation function which, in equilibrium, is given by,

$$f_0(\varepsilon) = \frac{1}{e^{(\varepsilon-\varepsilon_F)/K_B T}+1} \text{ (equilibrium F-D function)} \tag{4.4}$$

The solution of BTE within RTA can be used to derive thermoelectric (TE) transport parameters, which surprisingly yields accurate results for various systems [126].

In this study, the "BoltzTraP" code [106] is used which implements the Boltzmann theory to calculate the thermoelectric properties under constant relaxation time and rigid band approach [127]. The main transport properties calculated in this study are: Electrical Conductivity (σ), Seebeck Coefficient (S), Thermal (Electronic) Conductivity (K) as given by equations 4.5-4.7, respectively. Since Seebeck coefficient is independent of τ_m, it can be tested against experimental data to get the relatively realistic comparison.

$$J_e = \sigma E \text{ (In absence of magnetic field, B and thermal gradient, } \nabla T) \qquad (4.5)$$

$$S = -\Delta V/\Delta T \text{ (-ve sign, only when } \Delta V \text{ \& } \nabla T \text{ are opposite)} \qquad (4.6)$$

$$J_Q = -K\,(\nabla T) \text{ (In absence of electric field, ie } J_e=0) \qquad (4.7)$$

However, these transport coefficients, in a crystal, are tensors and given by the relations (2.23), (2.25) and (2.26), respectively.

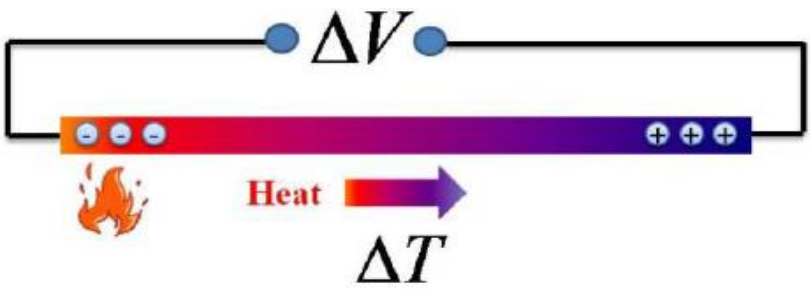

Figure 4.1 Voltage due to heat flow.

Thermoelectric effect refers to conversion of thermal energy into electric energy as shown in Figure 4.1. Good thermoelectric performance of a device is understood as having low thermal conductivity but high electrical conductivity as well as high Seebeck coefficient. These transport coefficients depend largely on the electronic structure of materials, specifically, electronic states near the Fermi level [128]. Moreover, the electron-electron correlation effect, present in vanadium oxides, are of immense interest for properties related to details of electronic structure [8]. Since the layered structures of oxide materials demonstrate interesting thermoelectric behavior [129], we are mainly interested in the thermoelectric properties of V_2O_5 which consists of layered unit cells. V_2O_5 is the most stable than the other two (vanadium dioxide and vanadium sesquioxide) and easy to produce using simple, inexpensive and non-toxic sol-gel deposition technique. Amongst the three oxides, only V_2O_5 exhibits thermoelectric (TE) properties [56] while VO_2 and V_2O_3 show little TE response (small value of Seebeck coefficient) as shown in Figure 4.2. In order to study the effect of phase transition on thermoelectric

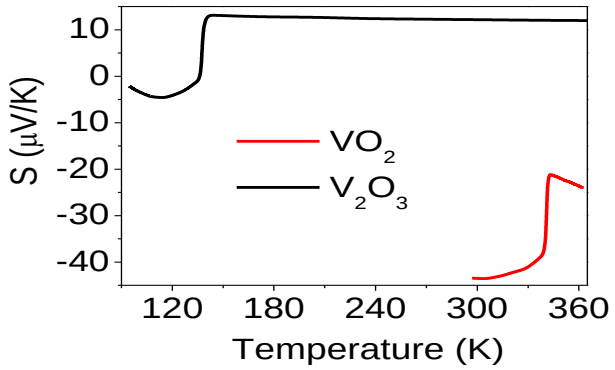

Figure 4.2 Seebeck coefficient versus temperature for VO_2 (red) and V_2O_3 (black) before and after phase transition [130, 131].

properties, the Seebeck coefficient, electrical conductivity and thermal (electronic) conductivity of vanadium dioxide, VO_2 are calculated.

Even though "BoltzTraP" works well for a large number of systems, it is computationally expensive because it requires high k-point mesh for convergence. In order to avoid the computational expense, a self-consistent (SCF) calculation was performed for the theoretical structure (before relaxation) with fewer (but well converged) k-point density. The electron density obtained in the SCF calculation was then fed to non-SCF calculation to obtain the electronic structure on a finer mesh of k-points as shown in Table 4.1. Both calculations use the cut-off energy to be 40 Hartree, a converged value with corresponding tolerance in energy of 0.1 meV for all the systems studied. In our study, the x-axis is defined parallel to the crystallographic a-axis (of conventional cell); y-axis is orthogonal to x-axis and lies in the a-b plane while z-axis is orthogonal to both the x and y axes. In other words, the coordinate-axes are same as crystallographic axes if the latter one is an orthogonal system. We have studied direction dependent (along the three axes) transport properties as well as their averaged (trace of a 3×3 tensor quantity) value.

Table 4.1 Non-SCF Grids Used in the Calculations

	Number of k-points in IBZ
V_2O_5	500
VO_2 (Metallic)	550
VO_2 (Insulating)	595

4.2 Transport Properties of Bulk V_2O_5

Figure 4.3 shows the variation of Seebeck coefficient with temperature from 10 to 700 K along the three crystallographic axes a b and c, at the value of chemical potential (μ) = 1.619 eV (≈ 1.624 eV, the Fermi energy). Clearly, the Seebeck coefficient is anisotropic. The absolute value of Seebeck coefficient, $|S|$, along a, is higher throughout the range beyond T = 150 K, as compared to the other two. The maximum (absolute) value of average Seebeck coefficient is found to be 246.54 μV/K at 300K. This value is consistent with the absolute value of 258 μV/K obtained in similar calculation [113] and an absolute value of 218 μV/K measured experimentally at room temperature [132]. Maxima and crossovers are also seen in the variation of Seebeck coefficient and have been attributed to the (a) "Specific details" of the band structure and (b) direction dependent electron-phonon interactions [133].

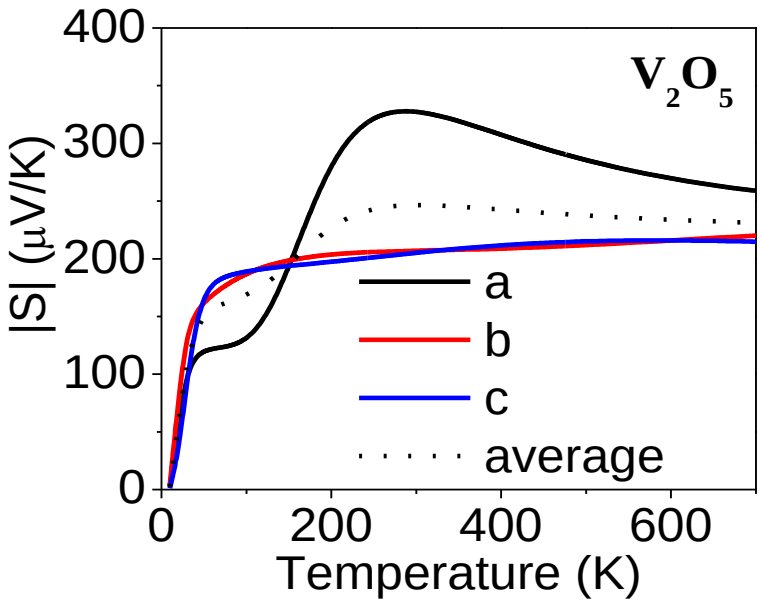

Figure 4.3 Seebeck coefficient versus temperature for bulk V_2O_5.

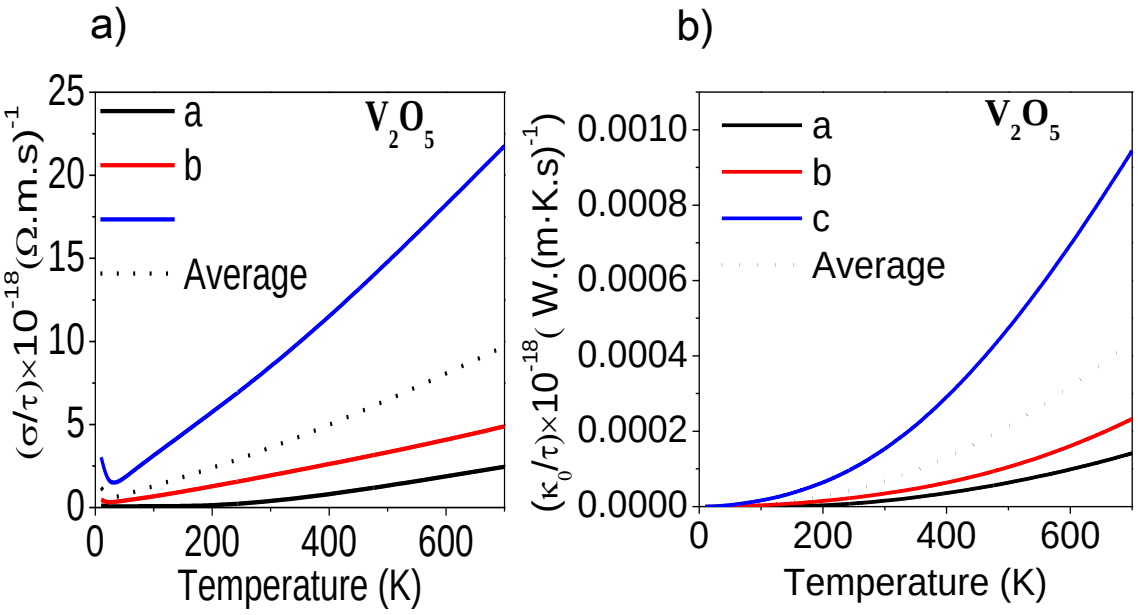

Figure 4.4 a) Electrical and b) thermal (electronic) conductivities of V_2O_5.

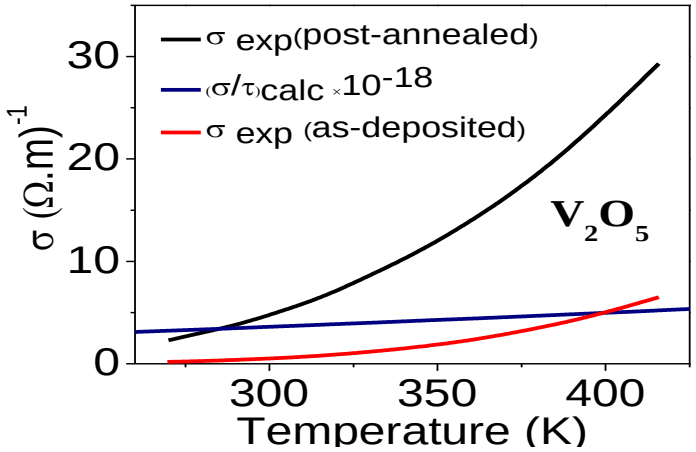

Figure 4.5 Calculated electrical conductivity of V_2O_5 compared with the experiment [132].

Figure 4.4 shows the temperature dependent variation of electrical and thermal (electronic) conductivities along the three crystallographic axes, in terms of constant relaxation time. Figure 4.5 shows the comparison of calculated averaged conductivity

($\sigma/\tau \times 10^{-18}$) with available experimental value of conductivity for V_2O_5 films (both as-deposited and post-annealed at 773 K) [132]. Assuming that the behavior of thin-film does not differ drastically with its bulk counterpart of V_2O_5 [134], we conclude that RTA, within the Boltzmann theory, cannot reproduce the experimental results of electrical conductivity with desired accuracy. In other words, the rate of variation of electrical conductivity is much higher than that predicted by the BTE. However, it can predict the anisotropic behavior as clearly manifested in the Figures 4.4 (a) in the following order: $\sigma_a < \sigma_b < \sigma_c$ and ${k^{el}}_a < {k^{el}}_b < {k^{el}}_c$. With attosecond momentum relaxation time ($\tau \sim 10^{-18}$ s), as seen from Figure 4.5, the thermal (electronic) conductivity, calculated in the Boltzmann framework, at 300K, is 6.7944×10^{-5} W/(m·K), which is ~3 orders of magnitude smaller than the thermal conductivity value of 0.45 W/(m·K), observed in the experiment [132]. Hence, the contribution of phonons might be taken into account to understand the thermal conductivity of bulk V_2O_5. With this analysis, we will mainly focus on Seebeck coefficient of VO_2 in the following discussion.

4.3 Transport Properties of Bulk VO_2

Figure 4.6 shows the temperature dependent variation of Seebeck coefficient of bulk VO_2 in its metallic rutile phase, at the value of chemical potential (μ) = 7.51 eV (≈ 7.47 eV the Fermi energy). In VO_2, there are two distinct directions for electric polarization: **E** ⊥ c and **E** ∥ c axes which is also manifested by the Seebeck coefficient in Figure 4.6. The absolute value of Seebeck coefficient increases with temperature. The absolute value of Seebeck coefficient parallel to the rutile c axis is slightly lower than its perpendicular counterpart. Berglund and Guggenheim [130] have measured Seebeck coefficients at

348K as 23.1 ± 0.2 μV/K and 21.1 ± 0.2 μV/K (absolute values) in the directions perpendicular and parallel to the rutile c-axis, respectively. The corresponding BoltzTraP (absolute) values are 227 μV/K and 205 μV/K, which are of one order of magnitude higher. This is due to the insufficient k-points used in our calculation. A rule of thumb is

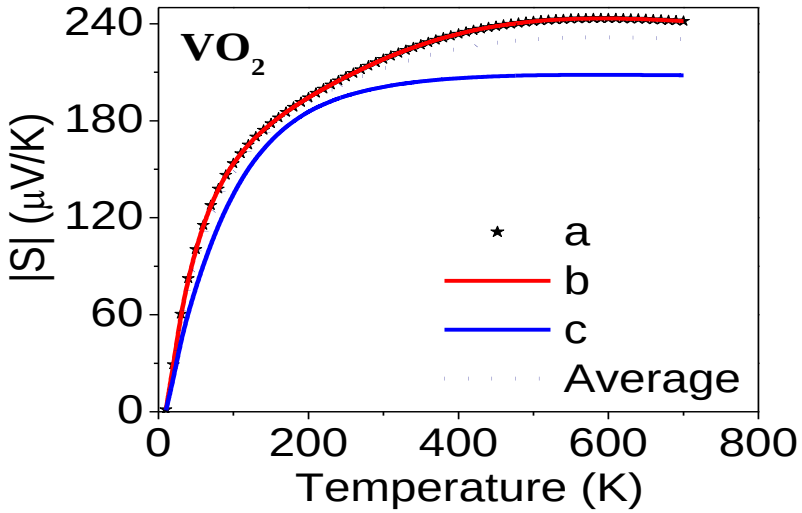

Figure 4.6 Seebeck coefficient versus temperature for bulk VO_2 in rutile phase.

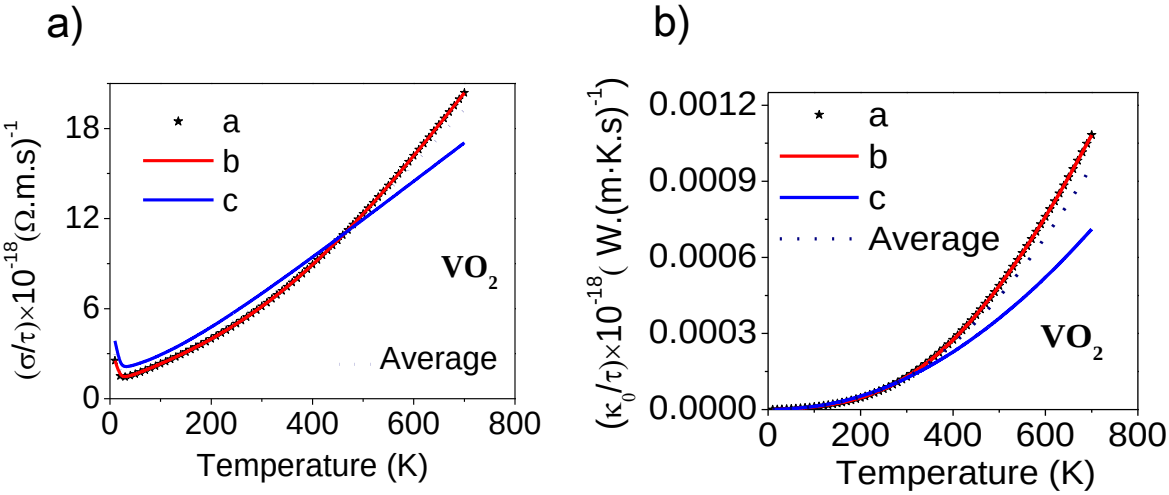

Figure 4.7 Electrical and b) thermal (electronic) conductivities of bulk VO_2 in high temperature phase.

that the number of k-points in the calculation should be more than $16 \times 10^6/V_{puc}$, where V_{puc} is the volume of the primitive unit cell [106]. Figure 4.7 shows the temperature dependent variation of electrical and thermal (electronic) conductivities along the three crystallographic axes, in terms of constant relaxation time. The anisotropic features are seen from both the plots, but electrical conductivity seems to be relatively reluctant to the directional variation as compared to the electronic component of thermal conductivity.

Figure 4.8 shows the temperature dependent variation of Seebeck coefficient of bulk VO_2 in its monoclinic phase, at the value of chemical potential (μ) = 7.51 eV ($\approx$ 7.44 eV, the Fermi energy). There is no noticeable anisotropy in the Seebeck coefficient. The Seebeck coefficient decreases with temperature. The absolute value of Seebeck coefficient at 298K is found to be 223 μV/K, whose magnitude is about five times greater than that measured in an experiment (43 μV/K, the absolute value) [130]. Seebeck coefficient in insulating phase deviates less from the experimentally measured values than that in the metallic phase. This relatively reduced value can be attributed to the reduction in BZ volume, where the k-point mesh is relatively denser. (The volumes of primitive unit cells, in real space, are: 59.149834 (Metallic phase) and 118.289910 $Å^3$ (Insulating phase) with a ratio of 1:2, which will be flipped in reciprocal space). Figure 4.9 shows the temperature dependent variation of electrical and thermal (electronic) conductivities along the three crystallographic axes, in terms of the constant relaxation time. Figure 4.10 shows the comparison of temperature dependent variations of Seebeck coefficient in low and high temperature phases with the experimental data; Seebeck coefficient in the metallic and insulating phases are scaled by factors 216/22.3 and 223/43, respectively. It is seen that the Seebeck coefficient, at experimental critical temperature of

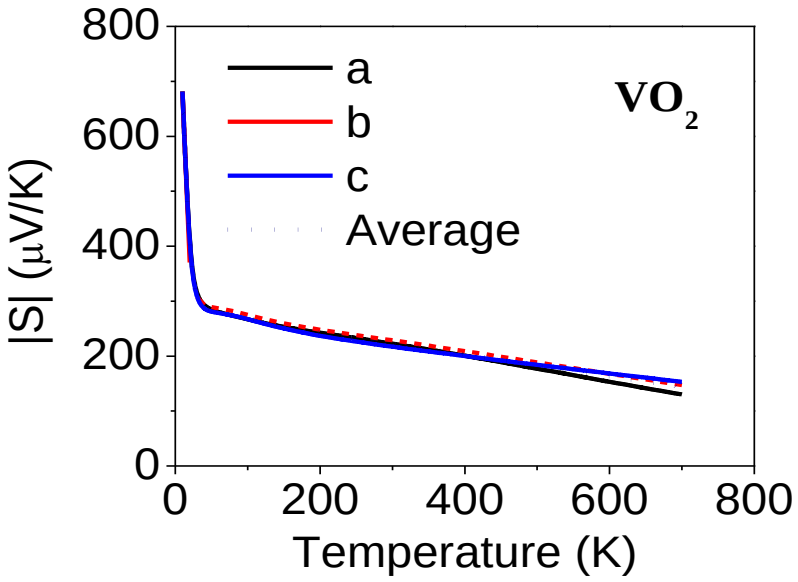

Figure 4.8 Seebeck coefficient versus temperature for bulk VO_2 in monoclinic phase.

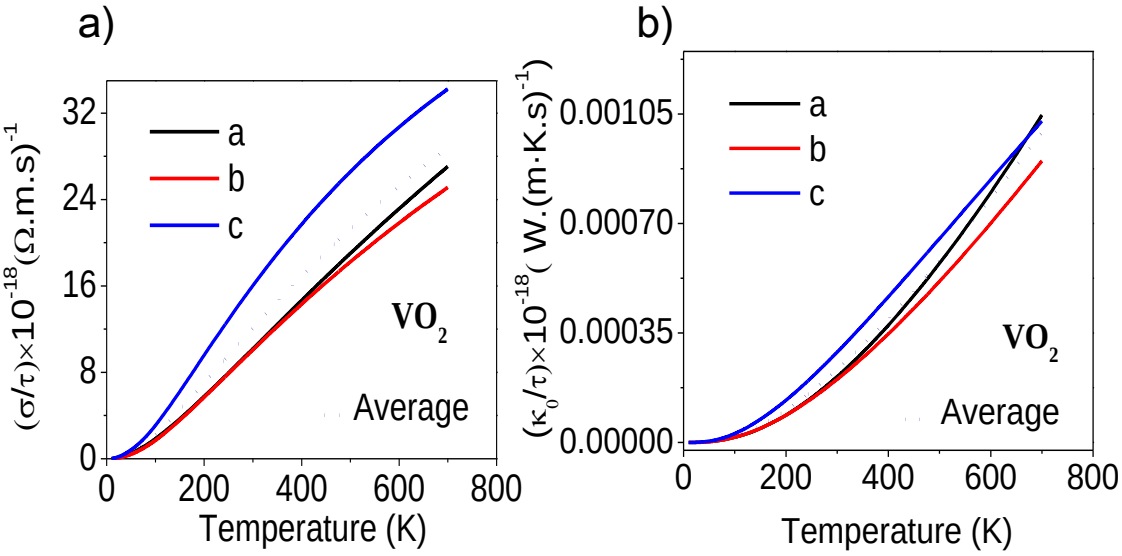

Figure 4.9 a) Electrical and b) thermal (electronic) conductivities of VO_2 in low temperature phase.

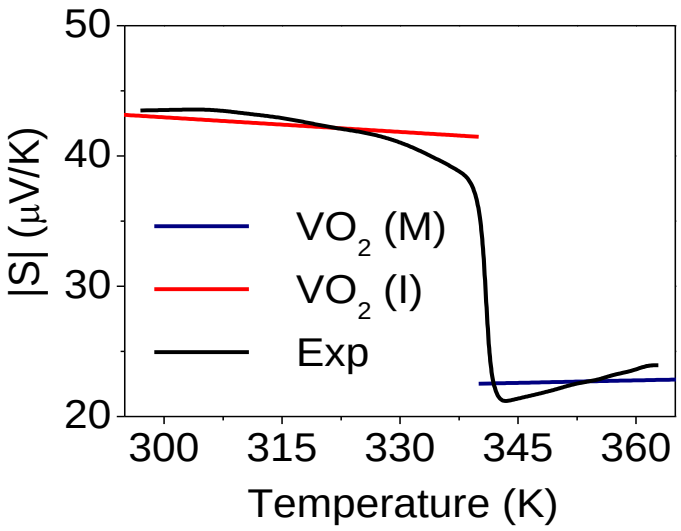

Figure 4.10 Seebeck coefficient in low and high temperature phases of bulk VO_2: "Kohn-Sham-Boltzmann" prediction of phase transition in VO_2.

340K, changes by 18.9 μV/K which lies within 10% of the observed discontinuity of 17.3 μV/K during the phase transition [130]. "Kohn-Sham-Boltzmann" approach can predict phase transition in VO_2 with reasonable accuracy.

4.4 Summary

Among the three oxides of our interest, in the present study, only V_2O_5 exhibits thermoelectric (TE) properties. It is the layered structure, stability and easiness to prepare by inexpensive and non-toxic approaches, which make V_2O_5 an interesting thermoelectric material. Seebeck coefficient, electrical conductivity and thermal (electronic) conductivity are studied as a function of temperature at a fixed value of chemical potential close to the Fermi energy using Kohn-Sham band structure approach coupled with Boltzmann transport equations. All the transport parameters have correctly reproduced highly anisotropic electrical conduction that has been observed in V_2O_5.

Maxima and crossovers are also seen in the temperature dependent variation of Seebeck coefficient which can be the consequences of "specific details" of the band structure and anisotropic electron-phonon interactions. Comparisons of averaged electrical conductivity with that of as-deposited as well as post-annealed V_2O_5 films have shown the value of momentum relaxation time to be ~10^{-18} s.

For understanding the effect of phase transition on transport properties, we have also calculated the thermoelectric properties of vanadium dioxide, VO_2, for both metallic and insulating phases. Seebeck coefficient and thermal (electronic) conductivity in metallic phase show similar and more pronounced anisotropic feature as compared to the electronic part of the thermal conductivity. However, in the insulating phase, Seebeck coefficient does not show noticeable anisotropy. The absolute value of Seebeck coefficient increases monotonically with temperature in the metallic phase while it decreases monotonically with temperature in the insulating phase. Seebeck coefficient, at experimental critical temperature of 340K, is found to change by 18.9 μV/K which lies within 10% of the observed discontinuity of 17.3 μV/K during the phase transition. "Kohn-Sham-Boltzmann" approach can predict phase transition in VO_2 with reasonable accuracy.

CHAPTER 5

OPTICAL PROPERTIES OF VANADIUM OXIDES

5.1 General Considerations

The optical property of a material originates from the response of electrons to perturbation due to the incident radiation and transition between electronic states. The two optical parameters, namely frequency dependent complex refractive index $\tilde{n}(\omega)$ and dielectric function $\in(\omega)$, are related to the electronic structure and band structure of the solid. The band gap calculation and absorption edge estimation have been of immense interest in research due to their application in the design of optical, electronic and optoelectronic devices. Band gaps of VO_2 and V_2O_5, at room temperature, have been reported as 0.6 eV [3] and 2.3 eV [135], respectively while a gap of 0.66 eV is found in V_2O_3 at 70K [124]. In this study, we have mainly analyzed the spectral dependence of the complex dielectric function $\in(\omega)$ of both bulk and thin film of the V-O systems deposited on Al_2O_3 substrates, based on the data available in the literature. Observed peaks in the corresponding spectra have been interpreted and compared as a function of structure, polarization and temperature. Complex dielectric function $\in(\omega)$ is related to the complex refractive index by the following equations,

$$\in_1 = n^2 - k^2 \tag{5.1}$$

$$\in_2 = 2nk \tag{5.2}$$

where, $n(\omega)$ and $k(\omega)$ are frequency (ω) dependent refractive index (n) and extinction coefficient (k), respectively.

Since the dielectric function is a complicated function of frequency [136], we have used the Penn model, a simplified model of a semiconductor or insulator [137, 138] to account for the average isotropic energy gap in terms of the long-wavelength electronic dielectric constant in the non-dispersive region. Van Vechten's [139] extension of Penn model to d-electrons has also been implemented to account for the energy gap and ionicity of the bonds have been calculated using the empirical theory developed by Phillips [140]. Also, the sum rule has been applied to the V-O system to describe the effective number of electrons participating in the optical transitions.

5.2 Review of Optical Spectra

Above T_c, VO_2 has a tetragonal crystal structure with two distinct directions for electric polarization. The lower symmetry monoclinic structure is energetically favorable for the crystal phase below T_c, and hence higher degree of anisotropic behavior is expected with three distinct directions for electric polarization. However, the "domain" pattern [141], observed in this low temperature phase, reduces the degree of anisotropy and hence electric vector (**E**) sees only two independent directions. Therefore, the optical properties have been studied with **E** ⊥ a axis for monoclinic phase and **E** ⊥ c axis for tetragonal phase and their parallel counter-parts. Anisotropic character of V_2O_3 is rarely taken into consideration since experimental study of its electrical and optical properties show very small directional dependence [142, 143]. However, V_2O_5 is highly anisotropic [114].

By definition, the dielectric function of an insulator or semiconductor quantifies the dielectric polarization, which in turn is described classically by the oscillation of a

spring connecting a pair of electric charges generated by an external electric field. Resonant oscillation of the spring, followed by light absorption, can be observed when the frequency of the incident radiation matches with the oscillating frequency of the spring. In other words, $\in_2$, which is proportional to the amount of light absorbed in the medium, shows a peak corresponding to the resonance frequencies of the spring. Since the region of interest for incident photons lies within the infrared to the vacuum ultraviolet range, we will analyze, in essence, the atomic and electronic polarization. On the other hand, refraction or absorption of light in a medium can be completely determined by the complex refractive index, (n+ik), as well. Clearly, the real part (n) controls the speed of light in the medium while the extinction coefficient (k) signifies absorption and modulates the amplitude of the electromagnetic radiation in the medium.

Figures 5.1-5.4 show the variations in optical properties such as $\in_1$, $\in_2$, n, k and R of the bulk and thin film of VO_2, V_2O_3 and V_2O_5 with photon energy at different temperatures and polarizations of electric field. It is evident from the figures that the optical parameters show strong variation with energy of incident photons from infrared to vacuum ultraviolet range (up to 12 eV). The value of $\in_1$ at temperature higher than T_c decreases with frequency at the lower end of the spectrum and becomes negative while the $\in_2$-E spectra show the corresponding exponential increase with decrease in frequency. This can be attributed to the free-carrier absorption or Drude tail of the metallic [144] phase and can further be justified by the rapid increase in reflectivity spectra with decrease in frequency below $\omega < \omega_p$, the plasma frequency at which $\in_1$ becomes zero. The Drude absorption feature can also be observed in k-E spectra at high temperature metallic phase as evidenced in Figure 5.3 (b). The anisotropy is manifested

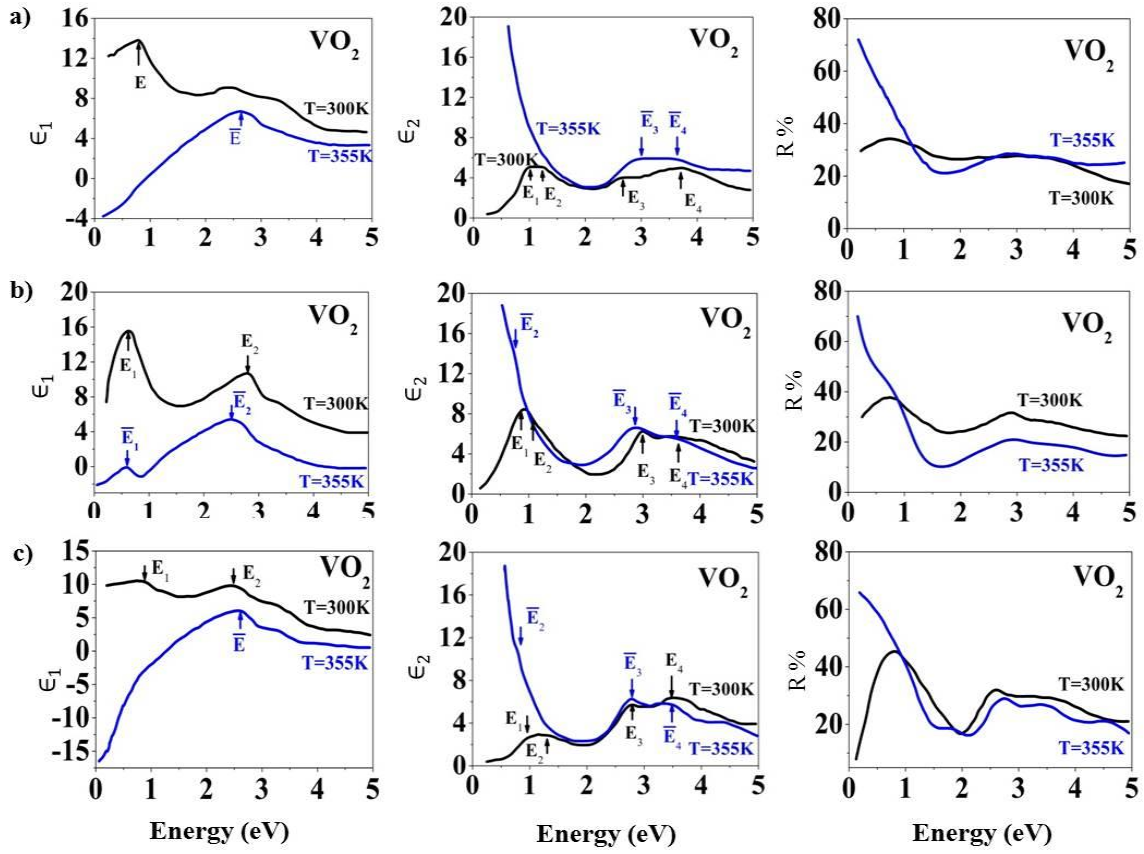

Figure 5.1 Variation of ϵ_1, ϵ_2 and R with photon energy at temperatures 300K and 355K [141] for bulk VO_2 with two polarizations of electric field (a) **E** ∥ a axis (b) **E** ⊥ a axis and (c) a 1000 Å thin film of VO_2 on Al_2O_3 substrate.

from the amplitude, width and energy position of the corresponding structure in the optical spectra for polarizations parallel to the crystallographic axes a, b and c. By comparing the peaks in the ϵ_2-E spectra of the insulating phase, for instance, of all the three oxides, V_2O_5 shows high anisotropic behavior; most of the peaks are more sharply peaked in V_2O_5 than those seen in VO_2 and V_2O_3. Similarly, unlike in high temperature phase, the absorption peaks in the ϵ_2-E spectra, at low temperature phase, are relatively sharper. The temperature dependence of the spectral variation of the optical properties is highly manifested at the lower end of the spectrum. These changes in the infrared region

during IMT are due to the onset of free carrier dominated absorption, a characteristic of metallic phase [141]. However, no remarkably high qualitative difference is observed in the optical spectrum between different temperatures at the higher frequency.

Figure 5.1 shows the comparison of the reflectivity spectra and dielectric function- both real and imaginary part- of vanadium dioxide in the energy range of 0.25-5.0 eV as a function of temperature below and above T_c. Figures 5.1(a) and 5.1(b) show $\in_1$-E, $\in_2$-E and R-E spectra of bulk single crystal of VO_2 for polarization **E** ∥ a axis and **E** ⊥ a axis, respectively while Figure 5.1 (c) shows the optical spectrum for 1000 Å polycrystalline thin film of VO_2 deposited on Al_2O_3 substrate. The band gap absorption, as expected in the $\in_2$-E spectra, cannot be seen which might be due to stoichiometric impurity and other imperfections in the samples. Comparison of Figure 5.1 (a) and (b) indicates the direction dependence of optical properties; the absorption and reflectivity peaks, observed in the low temperature phase, are higher for the polarization **E** ⊥ a axis as compared to the parallel counterparts. The contribution of atomic polarization to the dielectric function, which is indicated by the first resonance peak located in the infrared region, at 300K for electric field **E** ⊥ a axis is higher than for the polarization **E** ∥ a axis. A small peak appearing near 0.6 eV in the $\in_1$-E spectra in the metallic phase at 355K, as seen in Figure 5.1 (b), is absent for the polarization **E** ∥ a axis. It means that the anisotropy is remarkable in the infrared region. No significant difference in structural feature between the bulk and thin film spectra is seen. The structures in the spectra below 2.0 eV at high temperature phase have been described as a result of metallic free carrier dominated absorption [141]. However, significant peaks can be seen at energies above 2.5 eV in both phases as indicated in Table 5.1 and are explained in terms of (direct)

inter band transitions i.e. the transitions between the 2p (O) and 3d (V) bands which are separated approximately by 2.5 eV [141]. A shoulder appearing relatively distinct near 0.7 eV in the $\in_2$-E spectra of high temperature phase, in Figure 5.1 (b), has been interpreted as inter band transition within the 3d bands [141].

Table 5.1 Photon Energies Corresponding to the Peaks and Shoulders as Seen in $\in_2$-E Spectra of VO_2 [141]

		Bulk								Film on Al_2O_3			
		E ∥ a axis				**E**⊥ a axis							
E (eV) ⟶		E_1	E_2	E_3	E_4	E_1	E_2	E_3	E_4	E_1	E_2	E_3	E_4
$\in_2$	300K	1.0	1.3	2.6	3.6	0.85	1.3	3.0	3.7	1.0	1.3	2.8	3.5
	355K	---	---	3.0	3.6	---	0.75	2.9	3.6	---	0.85	2.8	3.5

Figure 5.2 shows the reflectivity spectra and dielectric function-both real and imaginary part- of vanadium sesquioxide (V_2O_3) from infrared to vacuum ultraviolet range (up to 10.0 eV) as a function of temperature below and above T_c. Figure 5.2 (a) shows the $\in_1$-E and $\in_2$-E spectra of bulk V_2O_3 calculated using density function theory [145] and R-E spectra of single crystal of V_2O_3 at near-normal incidence [63]. The absorption, in bulk V_2O_3 at temperature of 148K, starts at 1eV as seen in the $\in_2$-E spectra of Figures 5.2 (a). It means that the low temperature insulating phase is transparent to infrared radiation. Other absorption peaks appear at near infrared, visible and near ultraviolet regions as indicated in Table 5.2. The highest but wider peak centered at 6.1 eV covers the range from 5 to 9 eV, which is an indication of strong absorption in the ultraviolet region. The infrared reflectivity spectra of a single crystal of V_2O_3, measured in the temperature range of 100 to 600 K, show two distinct behaviors. Unlike the R-E spectra at the temperature of 100K, the reflectivity at low frequency edge increases with

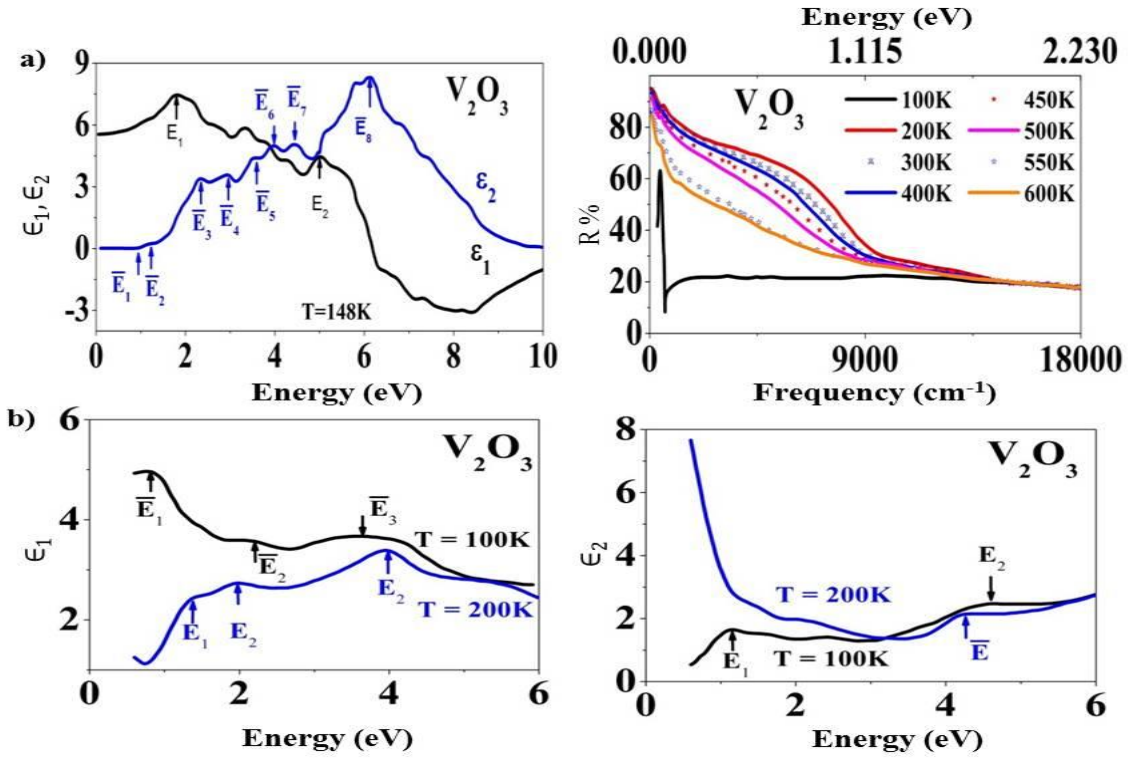

Figure 5.2 Variation of ϵ_1, ϵ_2 and R with photon energy for (a) bulk V_2O_3 at different temperatures [63, 145] (b) thin film of V_2O_3 on Al_2O_3 substrate [118].

decrease in frequency at all temperatures above 200K. This can be attributed to the high temperature metallic behavior. However, the temperature dependent variations at higher temperatures are relatively insignificant, and it seems that the significant changes in reflectivity occur within a few degree of T_c. On the other hand, the high frequency reflectivity tails merge with each other, irrespective of the temperature. Figure 5.2 (b) shows the dielectric function of a 75 nm polycrystalline film of V_2O_3 deposited on Al_2O_3 substrate at temperatures below and above T_c [118]. Table 5.2 lists the absorption peaks observed in the ϵ_2-E spectra. Clearly, fewer structures are seen in the case of experimental spectra of the thin film as compared to the calculated spectra of the bulk V_2O_3. This can be partially attributed to the optical property calculations combined with

other parameters such as temperature difference and possibly surface effects. However, the peaks in insulating phase, existing at three energy locations viz. E_2, E_3 and E_7 (see Table 5.2), seem to refer to major optical transitions.

Table 5.2 Photon Energies Corresponding to the Peaks and Shoulders as Seen in $\in_2$-E Spectra of V_2O_3 [118, 145]

Energy (eV) →		E_1	E_2	E_3	E_4	E_5	E_6	E_7	E_8
Bulk	148 K	1.0	1.2	2.3	3.0	3.6	4.0	4.5	6.1
Film on Al_2O_3	100 K	---	1.2	2.4	---	---	---	4.6	---
	200 K	---	---	2.0	---	---	---	4.3	---

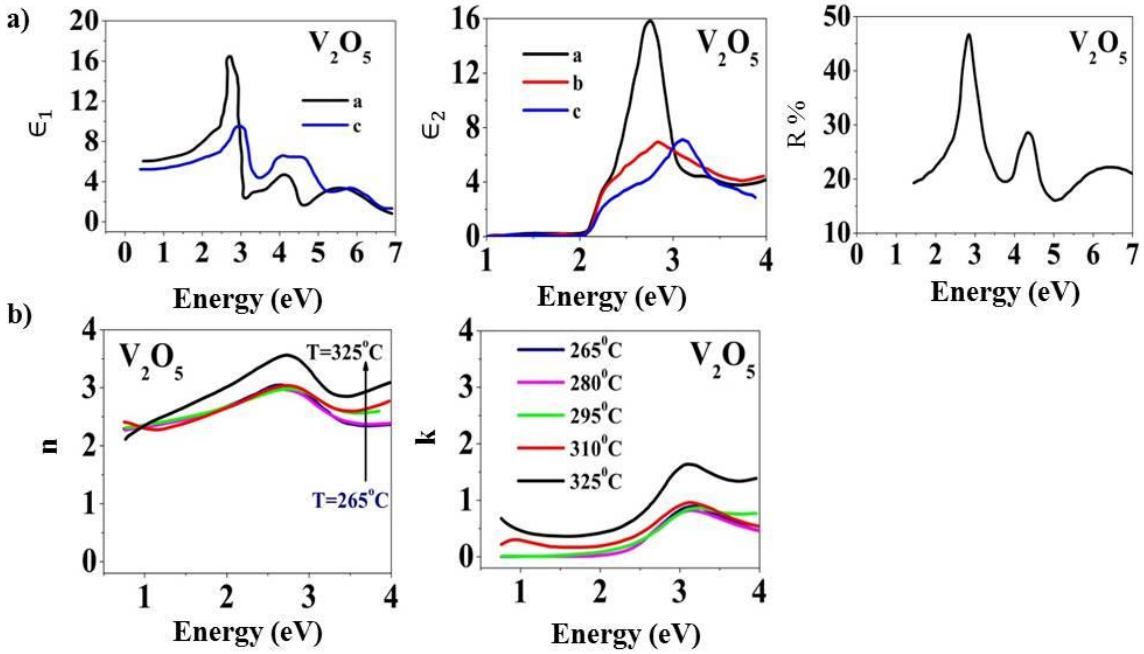

Figure 5.3 Variation of $\in_1$[115], $\in_2$[114], R[115] n and k [39] with photon energy for (a) bulk V_2O_5 at polarization **E** ∥ a (black), **E** ∥ b (red) and **E** ∥ c (blue) (b) thin film of V_2O_5 on Al_2O_3 substrate.

Figure 5.3 shows the dielectric function, reflectivity spectra, and both the real and imaginary part of refractive index of vanadium pentoxide (V_2O_5) from infrared to near-vacuum ultraviolet range (up to 7.0 eV) as a function of temperature below and above T_c. Figure 5.3 (a) shows the $\in_1$-E, $\in_2$-E and R-E spectra of bulk single crystal of V_2O_5 for polarizations parallel to crystallographic axes a, b and c. The band-edge absorption is visible around 2.0 eV from the $\in_2$-E spectra, which cannot be described by a unique inter band optical transition but can only be partially attributed to direct forbidden transitions (**k** $\neq$0, where **k** is the wave vector) [114]. Beyond the intrinsic edge towards higher energy, the peaks represent the absorption and correspond to electronic transitions from filled 2p (O) to empty 3d (V) states [115]. It can be seen from the $\in_2$-E and R-E spectra for polarization vector **E** ∥ a axis, in Figure 5.3(a), that the first sharp absorption occurs at around 2.8 eV whereas the second and third peaks appear at 4.3 and 6.4 eV, respectively. The dielectric function shows a very high anisotropy in the range between 2.2-3.3 eV (visible region) as noticed in $\in_1$-E and $\in_2$-E spectra; the spectra in **E** ∥ a axis deviates most from the other two. Clearly the anisotropy depends on the spatial distribution of electron wave functions and it is possible that the 3d-orbitals directed along the a-axis are relatively more localized, as indicated by the narrow intense peak in the $\in_2$-E spectra for **E** ∥ a axis, forming a wider conduction band. Figure 5.3 (b) shows the frequency dependent refractive index and extinction coefficient of a polycrystalline thin film of α-V_2O_5 deposited on Al_2O_3 substrate. The measurements were taken from 0.75 -4.0 eV at various temperatures ranging from 265 to 325 ºC with an increment of 15 ºC. Both n-E and k-E spectra exhibit significant temperature dependent change over the entire energy range indicating the phase transition. The k-E spectra shows a shift in the absorption edge

from 1.5 eV to less than 0.75 eV as the temperature rises from 280 to 295 ºC [39]. The sharp absorption observed in the k-E spectra, at around 3.0 eV, is close to the corresponding absorption peak located at 2.8 eV in bulk V_2O_5.

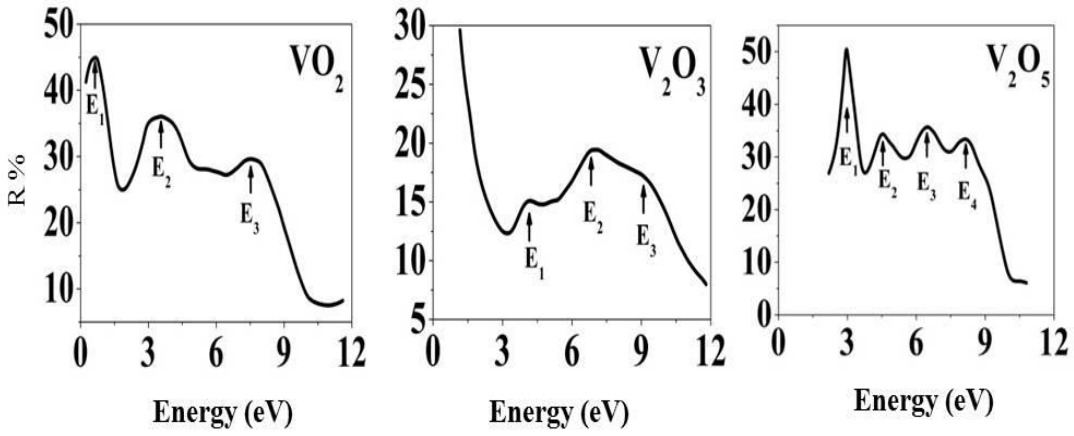

Figure 5.4 Variation of R with photon energy for bulk VO_2, V_2O_3 and V_2O_5 at 298K [146].

5.3 Application of Penn Model

Band structure of a material is related to its R-E spectra ($\in_2$-E spectra). By definition, an intensity maximum in R (or $\in_2$) in the R-E spectra (or $\in_2$-E spectra) represents a maximum number in the optically induced electronic transitions in the material [147]. The energy corresponding to the peak should therefore correspond to a band-to-band energy difference or a band gap. Since this is a macroscopic gap [138], it should be related to the high-frequency dielectric constant $\in_\infty$ ($=n^2$), where n is the refractive index. It should be noted here that "high-frequency" dielectric constant refers to the "zero-frequency" dielectric constant $\epsilon(0)$ which is low compared to interband transition frequencies but higher than phonon frequencies.

Several models [138, 148, 149] have been proposed to interpret the frequency and wave-vector dependence of the dielectric function. All these models have, however, been proposed for elemental semiconductors. Extrapolation of the applicability of these models to amorphous semiconductors, [150] and narrow and wide gap materials, including alkali halides [139, 151, 152], has been carried out with reasonable success. Here, we demonstrate the applicability of one such model to the three oxides of vanadium. For a model semiconductor, the high frequency dielectric constant is given by [138],

$$\varepsilon_\infty = 1 + \left(\hbar\omega_p/E_p\right)^2\left[1 - \left(E_p/4E_F\right) + \frac{1}{3}\left(E_p/4E_F\right)^2\right] \tag{5.3}$$

where, E_p is the Penn gap [138] and E_F is the Fermi energy given by [151],

$$E_F = 0.2947\left(\hbar\omega_p\right)^{4/3} \tag{5.4}$$

with the valence-electron plasmon energy given by [153]: $\hbar\omega_\mathrm{p} = 28.8(\mathrm{N_v}\rho/\mathrm{W})^{1/2}$, W is the molecular weight and $\mathrm{N_v}$ is the number of valence electrons per molecule calculated by using,

$$\mathrm{N_v} = \mathrm{Ma} + \mathrm{N}(8 - \mathrm{b}) \tag{5.5}$$

for a compound $A_M B_N$, where a(b) is number of valence electrons per atom of type A(B) and M(N) is the atomic fraction of element A(B). Equation (5.3) can be rewritten as,

$$\varepsilon_\infty = 1 + \left(\hbar\omega_p / E_p\right)^2 S_0 \qquad (5.6)$$

where, S_0 represents the terms inside the square brackets. Since the most significant variation occurs in the expression before S_0, Penn neglects the smaller terms containing E_g/E_F and thus approximates the value of S_0 as 1 [154]. This is true for materials with band gaps in the commonly occurring range where $E_g/E_F = 0.3$ [149]. However, Grimes and Cowley [149] found that the value of S_0 is only weakly dependent on the band gap and that a value of 0.6 is a fairly good representation of S_0. Thus, with this slightly more accurate value for S_0, the energy gap can be determined by using appropriate values of the dielectric constant.

At room temperature, VO_2 and V_2O_5 are in insulating phase while V_2O_3 is in metallic phase with very low density of states at the Fermi level [146]. It is believed that IMT is governed by the change in the 3d band structure [155, 156]. In Penn model, the effect of the d band is to increase the number of valence electrons per molecule, N_v. Van Vechten [139] has considered, in detail, the effect of d electrons on the dielectric properties of materials. In Table 5.4, we also evaluate the Penn gap incorporating the d-electron contribution to N_v as indicated within the parenthesis.

It is important to note here that the effective valence-conduction band gap, for the material consisting of different atoms in the unit cell, can be separated into homopolar (E_h) and heteropolar part (C) as introduced by Phillips [157]. Accordingly, we write $E_p^2 = E_h^2 + C^2$ and introduce a parameter, Phillips ionicity, defining the ionic character in

bonds as, $f_i = C^2/(E_h^2 + C^2)$, where, E_h is related to the static dielectric constant (ε_0) by [140],

$$\varepsilon_0 = 1 + \left(\hbar\omega_p/E_h\right)^2 S_0 \tag{5.7}$$

In order to study the Penn gap, which is the macroscopic gap accounting for all the possible optically induced electronic transitions in the material, we rely on the reflectivity data, measured at room temperature, extended for longer range of photon energy as shown in Figure 5.4 [146]. The size of the single crystal samples of V_2O_5 and V_2O_3 used in these measurements were 10×10×5 mm^3 each whereas that of VO_2 was 7×5×5 mm^3. The measurements were performed for the polarization **E** ‖ a axis. The energies corresponding to maxima in intensities seen in Figure 5.4 are listed in Table 5.3.

We can clearly see three major peaks for VO_2 crystal as indicated in the Table. The first peak appearing at 0.7 eV, in the insulating phase, corresponds to the shoulder appearing in the $\in_2$-E spectra of high temperature phase, in Figure 5.1 (b), both of them having the same origin of transition, i.e., from occupied to empty states within the d band [141, 146]. The other two peaks, at 3.6 and 7.4 eV, correspond to the transition from 2p (O) to 3d (V) band. The fact that the 3d-band width in V_2O_3 is around 3 eV [156], which is the largest of all three V-O system [146], and the electronic transitions start at 4.2 eV imply that no transition occurs within the d band in V_2O_3. Also, the transitions are mostly to the 4s, 4p bands of vanadium only after 10 eV [146], the observed peaks between 4.2 eV and 9.0 eV can be referred to the transition from 2p (O) to 3d (V) band. We can see four major peaks for V_2O_5 crystal as indicated in the Table and refer to the transition from 2p (O) to 3d (V) band, where the first peak at 2.97 eV shows the highest optical transition

rate and is attributed to excitonic transition [146]. Since the first peak appears at relatively high energy, no transition occurs within the d band in V_2O_5.

Table 5.3 Peak Energies from Reflectivity Data of the V-O Systems at Temperature of 298 K

Energy (eV) ⟶	E_1	E_2	E_3	E_4
VO_2	0.7	3.6	7.4	---
V_2O_3	4.2	6.8	9.0	---
V_2O_5	2.97	4.51	6.5	8.1

The results of the calculations based on Penn model are presented in Table 5.4. Also, listed in Table 5.4 are the values of band gap energy (E_g), zero-frequency (ϵ_0) and high-frequency (ϵ_∞) dielectric constants, Phillips ionicity (f_i), average homopolar (E_h) and heteropolar (C) energy gaps, Fermi energy (E_F) and arithmetic average of all the energies corresponding to the peaks in the R-E spectra ($\overline{E}$). Using the values of E_F and E_p listed in Table 5.4, we have evaluated the value of S_0 and it is found to be 0.88 which is more than our approximation but still less than unity. It can be seen from Table 5.4 that the calculated value of E_p for the single crystal of V_2O_3 is close to $\overline{E}$. While E_p of VO_2 and V_2O_5 are also seen to be in good accord with the corresponding values of $\overline{E}$, the difference between E_p and $\overline{E}$ for V_2O_5 is relatively higher as compared to that of VO_2. These relative deviations are consistent with the degree of anisotropy of the three V-O systems. It is important to note here that E_p value of VO_2 and V_2O_3 are closer to the value in the parenthesis (the average of all energies corresponding to the peaks and shoulders in the R-E spectra, $\overline{E}$). This indicates that an isotropic, nearly free electron model such as the Penn model seems to be valid in explaining the energies corresponding to the peaks in

the reflectivity spectra of these vanadium oxides. It is to be noted here that such a procedure of comparing the calculated E_p with the average of the energies corresponding to the peaks in the R-E spectra was proposed by Phillips [140]. Examining the ionicity, we see that the V-O systems are more than 65% ionic. V_2O_3 and VO_2 follow the general trend that low oxidation states of vanadium oxides are more ionic and undergo IMT [158]. However, V_2O_5 is highly ionic but is consistent with the fact that V_2O_5 is more ionic than VF_5 [159].

Table 5.4 Properties of the V-O Systems; the Parenthesis Value of $\overline{E}$ is the Arithmetic Average of All the Energies Corresponding to the Peaks and Shoulders in the R-E Spectra

V-O system	Mol. Wt (W)	ρ (g/cc)	E_g (eV)	N_v	$\hbar\omega_p$ (eV)	E_F (eV)	ϵ_∞	E_p (eV)	$\overline{E}$ (eV)	ϵ_0	f_i	C (eV)	E_h (eV)
VO_2	82.94	4.68 [160]	0.60 [3]	6	16.56	12.44	9.7 [161]	4.4 (4.6)	3.9 (4.79)	25.9 [161]	0.65	3.55	2.60
V_2O_3	149.88	4.98 [142]	0.66 [124]	10	16.60	12.48	5.0 [162]	6.4 (6.7)	6.6 (6.30)	15.0 [163]	0.71	5.43	3.44
V_2O_5	181.88	3.36 [164]	2.30 [135]	14	14.64	10.55	4.0 [165]	6.5 (6.8)	7.36 (5.52)	13.8 [115]	0.77	5.73	3.17

5.4 Sum Rule

At this stage, it would be worthwhile to look into the number of electrons participating in the optical transitions. Most of the electrons in the material are core electrons and are tightly bound to the atomic nuclei. If we consider that the core electrons are excited for high enough frequencies, the sum rule can be written as [166],

$$\frac{2\,\pi^2 N n e^2}{m} = \int_0^\infty \omega \in_2 (\omega)\; d\omega \tag{5.8}$$

where, m is the mass of a free electron; e, the electronic charge; N, the number of atoms per unit volume (atom density); ω, the angular frequency of light and n, the total number of electrons per atom. However, the electrons contributing to the optical properties of solids are conduction and valence electrons and, hence, the core states can be neglected. Further assuming that other absorptive processes such as phonon excitation are not overlapping with electronic excitation [167], the effective number of electrons per atom participating in optical transitions over a given frequency range is approximated by,

$$n_{eff}(\omega_0) = \frac{m}{2\,\pi^2 N e^2} \int_0^{\omega_0} \omega \in_2 (\omega)\; d\omega \; (In\ terms\ of\ frequency)$$

$$n_{eff}(\omega_0) = \frac{(4\,\pi\, \in_0) m}{2\;\pi^2 N \hbar^2} \int_0^{E_0} E \in_2 (E)\; dE \; (In\ terms\ of\ Energy\ and\ SI\ system)$$

(5.9)

where, $\in_0$ is the permittivity of free space and $n_{eff}(\omega_0)$ is the effective number of electrons per atom governed by polarization of electron shells, contributing to optical transitions below an energy ω_0. Since we are interested in calculating the effective number of electrons per formula unit, we define N as the number of vanadium ions per formula unit per unit volume.

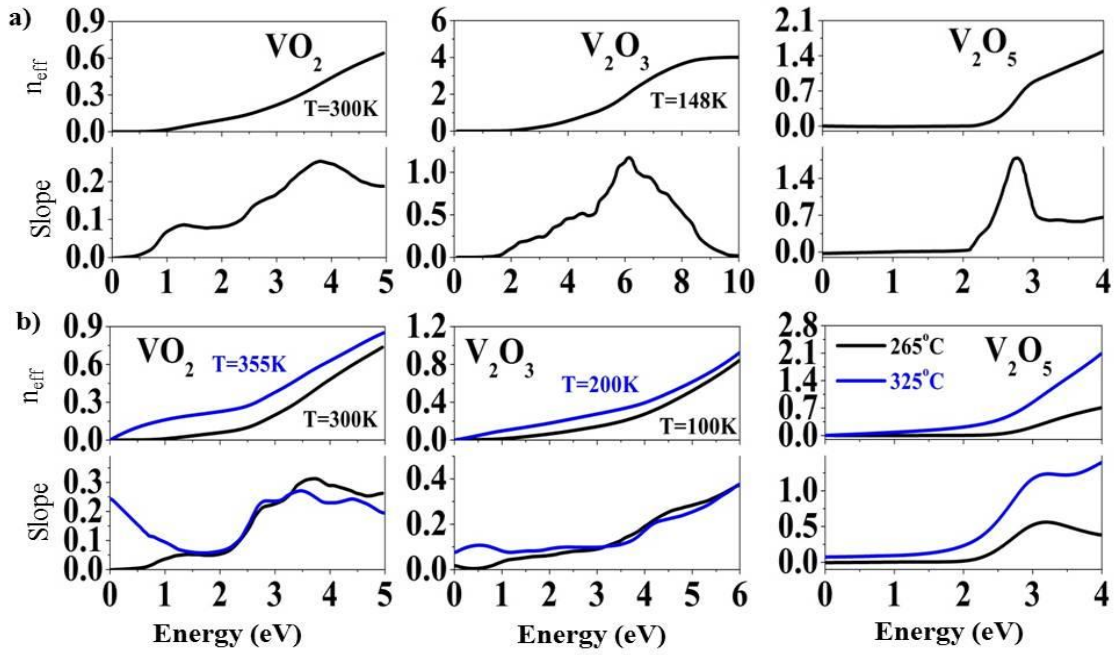

Figure 5.5 Variation of n_{eff} with photon energy calculated using Eq. (5.9) along with its slope with respect to the energy for (a) bulk at polarization **E** ∥ a [114, 141, 145] and (b) film of VO_2, V_2O_3 and V_2O_5 on Al_2O_3 substrate [39, 118, 141].

Figure 5.5 shows the variation of n_{eff} and its slope with photon energy, which were calculated numerically using Equation (5.9) for all the three V-O systems at temperatures below and above T_c. The effective number of electrons shows a clear temperature dependent variation with photon energy below and above T_c. The calculated n_{eff} for insulating phase is zero below certain photon energy but varies with photon energy. The

rate of change of n_{eff} with respect to energy of incident photons, referred to as slope, is not constant throughout the frequency range and shows significant variation.

The n_{eff} for both the bulk and thin film of VO_2, corresponding to the insulating phase (300K), is almost zero below 0.6 eV which then varies with the energy of incident photons. The slope for bulk phase, at 300K, initially increases until 1.2 eV, remains fairly constant from 1.2-2.1 eV, rises to a maximum at 3.8 eV, with a small shoulder in between, and finally decreases with increase in photon energy. The region of the shoulder may refer to the transition from 2p (O) to 3d (V) states and is small when compared to its expected value of unity for the absorption due to the one "extra" d electron per formula unit. While there are some differences in the magnitude between the slope of the bulk and film of VO_2, their energy dependent variations show similar pattern. The slope for the high temperature phase of VO_2 initially decreases and reaches minimum at 1.75 eV and then rises until 2.5 eV and finally shows slight rise and fall alternatively as indicated in Figure 5.5 (b).

The slope for V_2O_3 in Figure 5.5 (a) shows the highest peak, besides other small structures, at around 6.1 eV which indicates a strong absorption in the ultraviolet region. This peak is consistent with the corresponding peak in the $\in_2$-E spectra observed in Figure 5.2 (a). On comparing Figures 5.5 (a) and (b), we see that the n_{eff} for both the bulk and film of V_2O_3 in its insulating phase show similar trend until 3 eV. However, after 3 eV, the n_{eff} in the film of V_2O_3 deviates considerably from its bulk counterpart, which in fact shows saturation near a value of 4 electrons per formula unit at the end of the ultraviolet spectrum. Assuming that the density functional theory [145] correctly predicts the optical properties of V_2O_3 in the photon energy range of 0 to 10 eV, this saturation can be

attributed mainly to absorption due to the two d-electrons per vanadium ion combined with some contribution due to the transition from 2p (O) to 3d (V) states. However, there is a remarkable difference in the n_{eff} between the bulk and film of V_2O_3 and may require further study to make a definite conclusion to interpret the difference.

The n_{eff} for both the bulk and film of insulating phase of V_2O_5 is almost zero below 2.2 eV and is consistent with the observed absorption band edge. An abrupt change in the slope near the peak region, as seen in Figure 5.5 (a), is characteristic of inter band transition. This peak is consistent with the peak in Figure 5.3 (a) in the $\in_2$-E spectra observed at polarization **E** ‖ a axis. The n_{eff} in bulk phase of V_2O_5 shows a value of 1.49 at photon energy of 4.0 eV. Since V_2O_5 does not have any d electron in its V^{5+} ion, this should be the contribution due to the transition from 2p (O) to 3d (V) states. The value of n_{eff} corresponding to this transition is higher in V_2O_5 as compared to the other two oxides and can be attributed to the higher number of oxygen atoms per formula unit. A similar interpretation can be made for the film of V_2O_5 on Al_2O_3 substrate. However, the variation of n_{eff} with energy at two different temperatures below and above T_c appears to show more consistent pattern at sufficiently high photon energy in both VO_2 and V_2O_3 while a divergence pattern can be easily seen from Figure 5.5(b) for the corresponding variation in V_2O_5. Comparison of n_{eff} of bulk at room temperature and film of V_2O_3 at 265^oC shows different pattern of variation with photon energy which may be partly attributed to the difference in temperature and the highly anisotropic nature of V_2O_5. This may be due to the fact that studies [3, 39] of optical property do not pertain to the same crystallographic axis besides ambient conditions and other aspects of the experiment such as the quality of the crystal and analysis procedures. This conclusion is consistent with

the perspective of Kang et al. [39], where assertion has been made that the structural phase transition in V_2O_5 does not occur and that V_2O_5 film undergoes an IMT at a critical temperature of 280^oC instead of 257 ^oC [30] as reported in most of the literature.

5.5 Summary

Vanadium oxides, which consist of strongly correlated d electrons, are extremely sensitive to the external stimulus such as temperature and undergo insulator-metal transitions (IMT) at a particular temperature depending on the O/V ratio. Vanadium oxides are widely used in technology in which devices make use of their properties such as IMT, high temperature coefficient of resistance (TCR) and a small 1/f noise constant. In this study, we have analyzed the optical properties such as $\in_1$, $\in_2$, n, k and R of bulk and film of VO_2, V_2O_3, and V_2O_5 deposited on Al_2O_3 substrates, based on the data available in the literature. The observed peaks in the corresponding spectra have been interpreted and compared as a function of structure, polarization and temperature. The anisotropy is significant in the infrared region for VO_2 and in the visible region for V_2O_5. Penn model leads to an explanation of the energies corresponding to the peaks in the R-E spectra of the single crystal of the V-O systems at room temperature. E_p values for VO_2 and V_2O_5 are close to the average of the energies corresponding to the peaks ($\overline{E}$) while their values are even closer in V_2O_3, clearly reflecting the degree of anisotropy in the order of $V_2O_3 < VO_2 < V_2O_5$. The vanadium oxygen bonds are highly ionic and undergo IMT at T_c as a function of oxidation state of the vanadium ion i.e. the transition temperature increases with oxidation states of the vanadium atom. Optical transitions and effective number of electrons participating in these processes are described from the $\in_2$-E spectra and its numerical integration using the well-known sum rule. The results of these

calculations show that the optical transitions from valence to conduction band occur including the transition from 2p (O) to 3d (V) bands and the inter band transitions within the d bands. The optical spectra has no indication of the transition occurring from occupied to empty states within the d band for V_2O_3 and V_2O_5 systems but the intra band transition seems to occur in VO_2. The change in n_{eff} with respect to the energy of incident photons is also calculated and it is found that this change is consistent with the peaks observed in the $\in_2$-E spectra.

CHAPTER 6

SIMULATION OF SPECTRAL EMISSIVITY OF VANADIUM OXIDES (VO_X) BASED MICROBOLOMETER STRUCTURES

6.1 Introduction

Materials at non-zero temperature emit radiation and the radiated energy varies as the fourth power of the absolute temperature (Stefan-Boltzmann law). At room temperature, the emission is mostly in the infrared (IR) region which ranges from 0.75-1000 μm [168]. The other major source of thermal radiation is Cosmic Microwave Background (CMB) radiation, a remnant of the hot Big Bang theory for the origin of the universe (Nobel prize in 1978, Penzias and Wilson of Bell Labs, NJ, USA). The microwave ranges in the region between 103 to 106 μm. Detection of dangers in advance, superior situation awareness and the use of precise weapon on time are the main requirements for both military (defense) and non-military (civilian) security applications. Infrared detectors, sensitive in both short and long wavelength infrared region, fulfill most of these requirements [116].

The atmosphere allows infrared (IR) transmission in the following region [168]: 0.79-1.7 μm (Near Infrared, Near-IR), 2-6 μm (Mid Wave Infrared, MWIR) and 8-14 μm (Long Wave Infrared, LWIR). As can be seen from Figure 6.1, the transmission is affected primarily due to the IR scattering and absorption by various atmospheric gases such as H_2O, CO_2, O_3 and O_2. According to Wien's displacement law, a sensor such as the human eye can see an object in the presence of radiation within certain range of electromagnetic (EM) spectrum and a temperature source around it, with certain minimum temperature (for example: industrial fluorescent light bulbs for eye) as shown

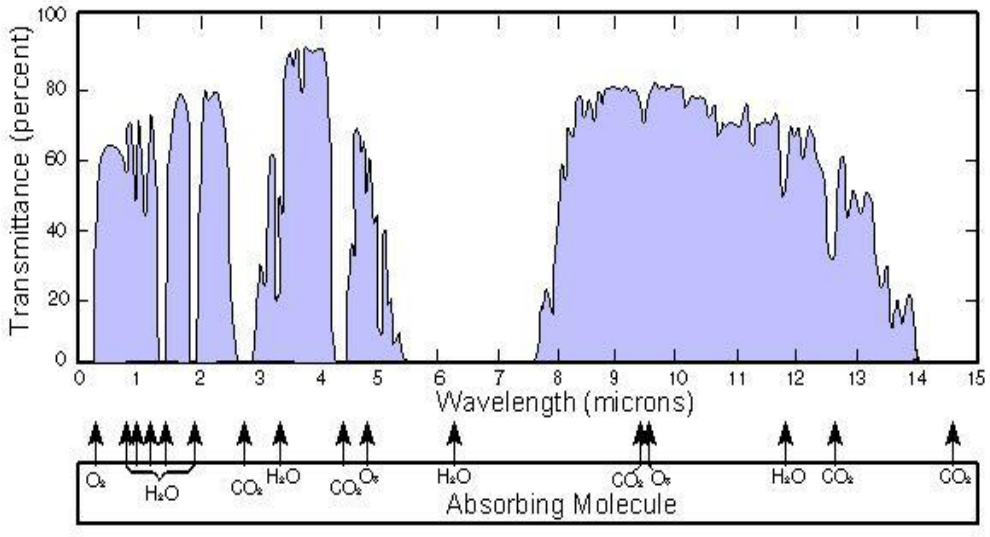

Figure 6.1 IR transmission in earth's atmosphere [168].

in Table 6.1. Usually 8-14 μm window is a choice for high performance thermal imagers because of the following reasons: (a) smoke and mist particles are small as compared to these wavelengths and IR can easily transmit through them; (b) it is highly sensitive to objects at ambient temperature and (c) scattering by gas molecules is very small in the region above 2 μm [169]. However, at high altitude in the atmosphere, where the temperature is far below -35ºC, the IR detection is still a challenge to the current technology.

Table 6.1 Minimum Temperature of Sources Required to "See" an Object in Different Spectral Regions [170]

	Eye	Near IR	SWIR	LWIR
λ (μm)	0.38-0.72	0.79-1.7	2-6	8-14
Temp (ºC)	525	275	-25	-35

In order to detect radiation, a photodetector, a device which converts the absorbed photons into a measurable form is used. There are mainly two types of detectors that can convert the absorbed photons into a measurable form: photon detectors and thermal detectors. A photon detector is an optoelectronic device which gives rise to an electrical output signal when energy distribution of electrons changes as a result of the interaction of radiation with either free or bound charge carriers in a material. Interaction can be either internal or external. In internal interaction, photons either interact with charge carriers (bound or free) or produce a localized excitation of an electron to higher energy state [171]. However, in external interaction, electrons are emitted as a result of Einstein's photoelectric effect. On the other hand, thermal detectors absorb the photon energy and convert it into heat which, in turn, affects physical or electrical parameters such as electrical conductivity, thermoelectric voltage, and pyroelectric voltage. Hence thermal detectors do not depend on the nature of the photon or spectral content of the radiation but depend on radiant power; the spectral response of a sensing material is determined by the emissivity of the surface. Since heating and cooling are slower processes compared to the interaction between photons and electrons, thermal response is relatively slower than spectral response. Typically, thermal effects occur in millisecond time scale while the effects due to photons are observed on micro or nano second time scale.

Photon detectors are used in IR detector technology due to two major performance parameters: excellent signal to noise ratio and fast response time. Since the energy of incident photons is comparable to average thermal energies (K_BT) of atoms of the sensing element [172], the noise due to thermal charge carriers is inevitable and hence

these photon detectors require cryogenic cooling to 77K or below [1]. Cooling mechanism, included in the photodetectors, makes the device not only heavy, bulky and inconvenient but also expensive. Furthermore, photon detectors lack in broad band response, i.e., they exhibit selective wavelength dependent response to incident radiation. The difficulty in operating photon detectors with appropriate spectral response in the IR region [173] is their other drawback. On the other hand, thermal detectors such as thermocouples, bolometers, thermopiles, and pyroelectric detectors are interesting because they are rugged, reliable, light, inexpensive and they can be operated at room temperature. Most of the thermal detectors are passive devices since they do not require bias and, most importantly, they provide flatter spectral response. In this chapter, a discussion of one of the thermal IR detectors, the bolometer, is presented.

The bolometer consists of a sensing element having a strong temperature coefficient of resistance [TCR, $\alpha = \frac{1}{R}\frac{dR}{dT}$] so that a small temperature change, caused by the incident radiation, can be measured. Commonly used bolometer sensing elements are: VO_x, SiO_2 and amorphous Silicon ($\alpha - Si$) [168]. Thermal bolometric detectors can be fabricated on thermally isolated hanging membranes by utilizing micro-electro-mechanical systems (MEMS) technology [174]. A "monolithic" structure fabricated, at Honeywell, by silicon micromachining is termed as microbolometer which consists of a two-level structure with a gap (d) of ~ 2.5 μm between them as shown in Figure 6.2 (Texas Instruments developed the pyroelectric detector arrays). The upper layer is a square shaped silicon nitride (Si_3N_4) plate, of side 50 μm and thickness 0.5 μm, suspended over an underlying silicon readout integrated circuit (ROIC) substrate. Encapsulated in the center [169] of Si_3N_4 bridge is 500Å of polycrystalline VO_x - a

popular thermistor. A reflective layer of Al coated on top of Si wafer increases the absorption effectively at 10μm wavelength due to the formation of a quarter wave resonant cavity.

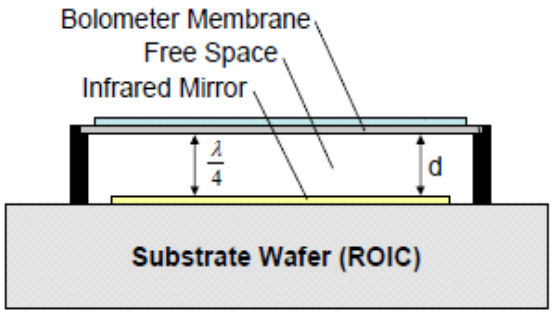

Figure 6.2 Schematic of a microbolometer pixel structure [168].

Due to the development of MEMS technology, uncooled infrared bolometers have now maintained the performance levels of cooled infrared photon detectors [51]. The performance of a thermal detector can be divided into two steps: raising the temperature of a sensing material by input radiation and using the temperature dependent variation of a particular property of the material as its response. The second step, involving the use of material property, depends on the type of thermal detector and, for a bolometer, TCR is utilized. TCR is related to the voltage responsivity, a widely used parameter to specify the performance of a bolometer, as,

$$R_v = \frac{\alpha I R_0 \Delta T}{P_i} = \frac{\alpha\, I\, R_0 \epsilon}{G(1+\omega^2\tau^2)^{1/2}} \tag{6.1}$$

where, P_i is the incident power, G is thermal conductance, ω is frequency of sinusoidal excitation, τ is thermal time constant, ΔT is the rise in temperature, ϵ is emissivity, R_0 is resistance at ambient temperature and I is bias current. The complete characterization of a microbolometer requires the understanding of both electrical and optical properties. The focus of the present study is the simulation of room temperature spectral emissivity of a single pixel industry standard VO_x based microbolometer.

6.2 Results and Discussion

The Multi-Rad, a copyrighted software, was developed at Massachusetts Institute of Technology (MIT) to study the radiative properties of silicon-related layered materials [175-177]. It implements thin film optics in the form of the matrix method of multilayers [175] and assumes the layers to be optically smooth, parallel to each other, optically isotropic (no variation in azimuthal direction) and the area in question is much larger than the wavelength of the incident radiation (no edge effects).

A generic layered structure is shown in Figure 6.3 [178]. The analyses in this section follows the earlier approach [178]**.** There are N layer interfaces (circled) and N+1 "layers" (squared), including the unbounded transparent media on each side of the actual stack. The terms A_i and B_i are the amplitudes of the forward and backward propagating electric-field vectors on the left side of the interface, i. The prime notation on A'_{N+1} and B'_{N+1} indicates that these are the amplitudes on the right side of interface N. Light is incident on interface 1, with an angle of incidence $\theta = \theta_1$.

The central equation of the multilayer theory relates the amplitudes on the left side of interface 1 with those on the right side of interface N,

$$\begin{pmatrix} A_1 \\ B_1 \end{pmatrix} = \left[\prod_{i=1}^{N} P_i D_i^{-1} D_{i+1} \right] \begin{bmatrix} A'_{N+1} \\ B'_{N+1} \end{bmatrix} = \begin{bmatrix} m_{11} & m_{12} \\ m_{21} & m_{22} \end{bmatrix} \begin{bmatrix} A'_{N+1} \\ B'_{N+1} \end{bmatrix} \tag{6.2}$$

where, P_i is the propagation matrix, D_i is the dynamical matrix, and m_{ij} is an element of the transfer function matrix. The propagation matrix accounts for the effect of absorption and interference within a layer *i* bounded by two interfaces.

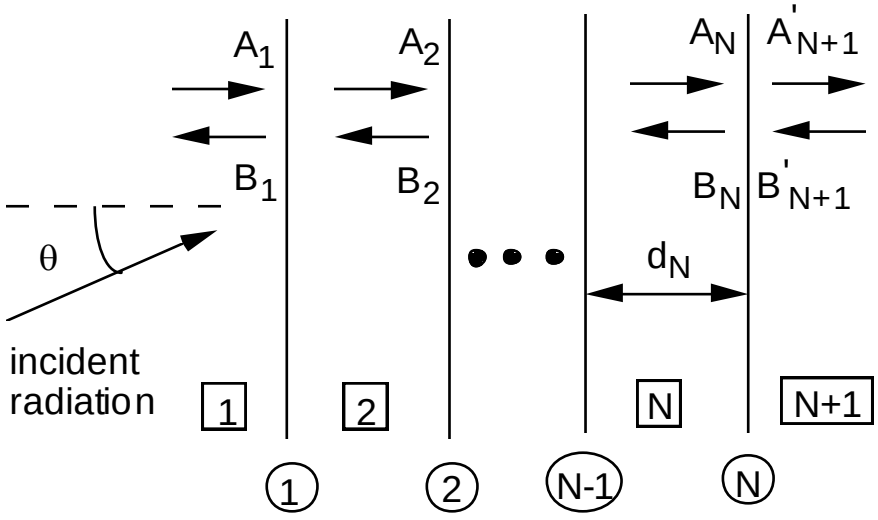

Figure 6.3 Notation for matrix method of multilayers.

Reflectance, transmittance and emittance of a multilayer stack can be studied in the spectral range of 0.4-20 μm at different thickness and angle of incidence. Radiation at a given wavelength is treated as coherent; so interference effects are taken into account [179]. The details of the modeling and the approach to the simulation has been described in earlier studies [178].

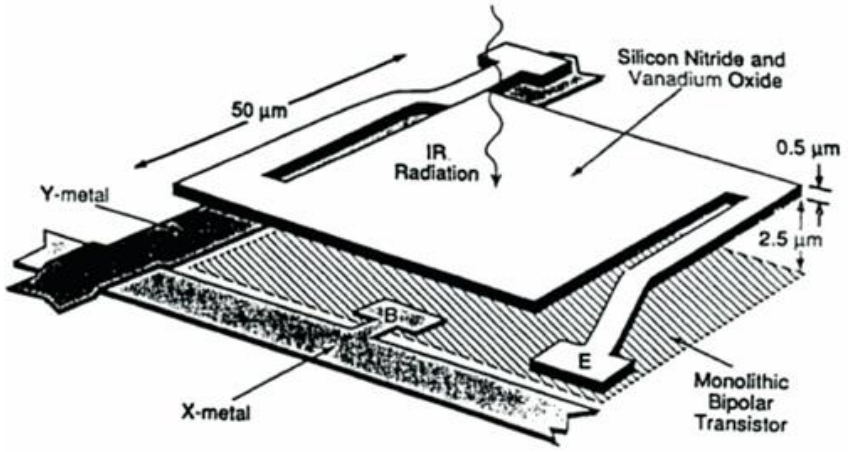

Figure 6.4 A microbolometer pixel structure [180].

Emissivity, $\varepsilon(\lambda, \theta, \phi, T)$, is the ratio of energy radiated from a material surface to that radiated from a blackbody at the same temperature (T), wavelength (λ), viewing condition (θ, ϕ). It also depends on the property of a material and its surface roughness. According to Kirchhoff's law, emissivity is equal to absorptivity for an object in thermodynamic equilibrium which can be clearly conceptualized from the notion that an object absorbing all the incident light will emit more radiation. Radiation penetrates certain thickness of the specimen before being absorbed and hence opacity is not only a material property but it depends on thickness as well. Emissivity also depends on its thickness; for instance, thinner sample is characterized by lower emissivity. Emissivity is usually measured (experimentally) at a direction normal to the surface. In this study, the point in question is singular with respect to ϕ and hence $\theta=0$ and $0 \leq \phi \leq 2\pi$. The present study analyzes the spectral emissivity of the VO_x based micro-bolometer structure [Figure 6.4] under conditions of normal incidence using Multi-rad. The microbolometer structure, considered in this study, was originally developed by Honeywell, Inc. [180].

In the Honeywell microbolometer structure, the bolometer sensing element has been chosen to be VO_x, a standard sensing material with x equal to 1.8, and is used in large scale production [181]. The thin films (500Å) of mixed oxides of vanadium (VO_2,V_2O_3 and V_2O_5) result in a family of materials having desired properties for bolometric operation such as high TCR and well-defined electrical properties with good fabrication capability [53]. As mixed oxides of vanadium, the VO_x can be realized as,

$$x\ VO_2 + yV_2O_3 + zV_2O_5 = VO_{1.8} \tag{6.3}$$

The above equation yields the two relations,

$$x+2y+2z=1$$

$$2x+3y+5z=1.8$$

which after solving yields the following relation,

$$y\ (V_2O_3) + (1.4 - 4 \times y)(VO_2) + (y - 0.2)(V_2O_5) = VO_{1.8} \tag{6.4}$$

This leads to a set of inequalities for non-zero amount of all three oxides as: $y > 0$; $(1.4 - 4 \times y) > 0; y - 0.2 > 0$ i.e. $0.2 < y < 0.35$. Since x=1.8 in VO_x is nearly equal to 2, we assume that other oxides (V_2O_3 and V_2O_5) are formed during VO_2 deposition process, due to their smaller heat of enthalpy (enthalpy of formation, ΔH, for V_2O_5, V_2O_3

and VO_2 are −1557, -1219 and −713 cal/mole, respectively [182]). By choosing y = 0.2025, a value close to 0.2, relation (6.4) can be written as,

$$0.2025\ (V_2O_3) + 0.59 \times\ (VO_2) + 0.0025\ (V_2O_5) \quad = VO_{1.8} \tag{6.5}$$

On the other hand, the value of y can be chosen in such a way that the maximum possible amount of V_2O_5 is obtained in the mixture, consistent with the lowest enthalpy of all the three vanadium oxides. Choosing the value of y = 0.3475, the following relation is obtained,

$$0.3475\ (V_2O_3) + 0.01 \times (VO_2) + 0.1475\ (V_2O_5) = VO_{1.8} \tag{6.6}$$

However, by considering the heat of formation, ΔH, and assuming that different oxides are formed with a probability which varies linearly as ΔH, the following relation is obtained,

$$y: (1.4 - 4 \times y): (y - 0.2) = 1219: 713: 1557 \tag{6.7}$$

The non-negative value of y, obtained by solving equation (6.7), is 0.3 and leads to the following relation,

$$0.3\ (V_2O_3) + 0.2 \times (VO_2) + 0.1\ (V_2O_5) = \ VO_{1.8} \tag{6.8}$$

Accordingly, 0.05 μm thick VO_x layer in 50µm× 50µm pixel, in Figure 6.4, can be realized in the following three combinations:

(a) t (VO_2) = 4.7589×10^{-4} μm, t (V_2O_3) = 0.0281 μm, t (V_2O_5) = 0.0214 μm [based on relation (6.7)] - consistent with lowest ΔH of V_2O_5;

(b) t (VO_2) = 0.0313 μm, t (V_2O_3) = 0.0183 μm, t (V_2O_5) = 4.0551×10^{-4} μm [based on relation (6.5)] – with the assumption that the two oxides, V_2O_3 and V_2O_5, are formed during the deposition process of VO_2;

(c) t (VO_2) = 0.0099 μm, t (V_2O_3) = 0.0251 μm, t (V_2O_5) = 0.0150 μm [based on relation (6.8)] – with the assumption that formation probability of the three oxides is linear with enthalpy.

For clarification and simplicity, we will label them as combinations (a), (b) and (c), respectively, in the following discussion. The use of thickness (and composition) to four-decimal place is due to the capability of Multi-rad.

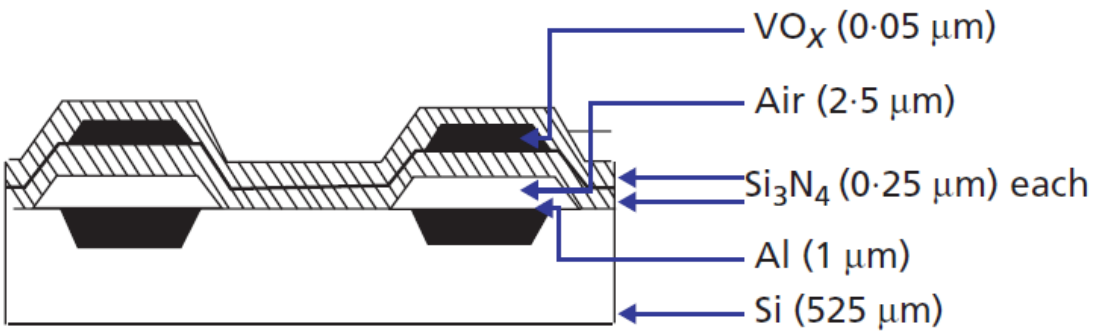

Figure 6.5 Simulated structure of a microbolometer pixel [180, 183].

Materials, in Multi-rad, are defined in terms of their real and imaginary parts of their refractive indices; the air gap is defined as n = 1 and k = 0 throughout; the wavelength dependent optical constants, n and k, of Al, VO_2, V_2O_3 and V_2O_5 have been taken from the literature [184-186]. Since typical microbolometer pixels are fabricated on an industry standard substrate of 4 inch diameter [187], wafer thickness is taken as 525 μm [188], with 1 μm thick Al layer "deposited" on the substrate. The simulated structure of the microbolometer pixel is shown in Figure 6.5.

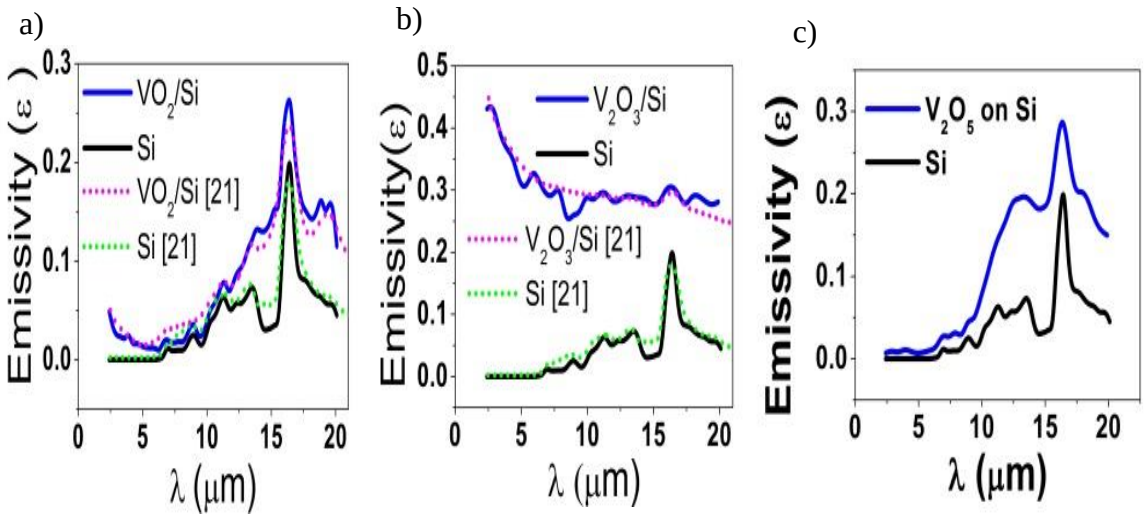

Figure 6.6 Comparison of simulated emissivity of VO_2/Si, V_2O_3/Si and Si with experiments [185]; only simulated emissivity is presented for V_2O_5/Si.

Room temperature emissivity of VO_2/Si, V_2O_3/Si and Si, simulated using Multi-Rad, and their comparison with experimental data are presented in Figure 6.6. As can be seen in the figure, the simulated values of emissivity of these structures are in good agreement with the experimental data. It can be further noted that V_2O_3/Si exhibits high emissivity that is consistent with the metallic behavior of V_2O_3 at room temperature. The

emissivity spectrum of VO_2/Si follows the wavelength dependent emissivity of Si. Thus, having established the validity of the application of Multi-Rad in simulating the emissivity of vanadium oxides/Si successfully, the study is extended to simulate the emissivity of V_2O_5/Si. Similar to VO_2/Si, V_2O_5/Si also follows the spectral emissivity of Si. It should be noted that VO_2 and V_2O_5 are insulators at room temperature.

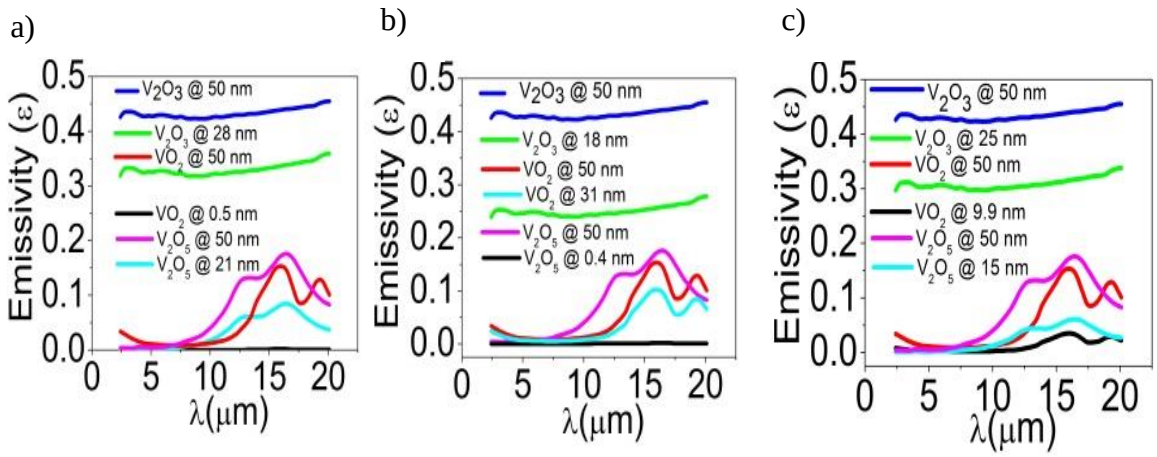

Figure 6.7 Room temperature (30 °C) emissivity of each of VO_x constituents for different thicknesses of the three combinations defined by relations (6.6), (6.5) and (6.8).

Figure 6.7 shows the calculated emissivity of each of the VO_x constituents, at 30 °C, in the wavelength range of 2.4-20 μm, for different thicknesses of the three combinations defined by relations (6.6), (6.5) and (6.8). As can be seen in the figure, the emissivity of each oxide at different thickness, corresponding to the combinations (a) through (c), is calculated and compared with a situation where 50 nm thick VO_x is either VO_2 or V_2O_3 or V_2O_5. The emissivity of V_2O_3 (metallic phase [189]) shows almost flat spectral response throughout the wavelength range considered in all the combinations. However, the emissivity of the insulating phase [189] of both VO_2 and V_2O_5 exhibit wavelength dependent variation with two major peaks as shown in Table 6.2. Emissivity spectra of

VO_2 have peaks at wavelengths 15.9 and 19.2 μm whereas those of V_2O_5 have peaks at wavelengths 13.2 and 16.5 μm. Without implying generality, wavelength λ=16.5 μm corresponding to the highest value of emissivity, listed in Table 6.2, will be considered as a reference value for comparison as seen in the following discussion.

Table 6.2 Emissivity Peaks for Each V-O System of Three Different Combinations

VO_2	Wavelength (λ)		λ_1=15.9 μm	λ_2=19.2 μm
	Emissivity-peak for thickness (t)	t_1=0.0099 μm	0.035	0.029
		t_2=0.0313 μm	0.103	0.085
		t_3=0.05 μm	0.154	0.129
V_2O_5	Wavelength (λ)		λ_1=13.2 μm	λ_2=16.5 μm
	Emissivity-peak for thickness (t)	t_1=0.0150 μm	0.044	0.061
		t_2=0.0214 μm	0.061	0.085
		t_3=0.05 μm	0.132	0.177

It can also be seen from Figure 6.7 that the qualitative features of emissivity of the three oxides, at two different thicknesses, are generally similar for all the combinations, the deviation being $\leq$ 7.03% (excluding films of thickness less than 1 nm for which the emissivity is close to zero). Since the industry uses 0.05μm thick film of VO_x (Figure 6.5), all the calculated emissivity of the vanadium oxides have been normalized with respect to the emissivity of 0.05μm thick film of VO_x. Emissivity is a volume effect. In order to correlate the film thickness with emissivity, the parameters: "thickness ratio", defined as the ratio of 0.05μm to the thickness of a single oxide film and "ε-scaling", defined as the ratio of emissivity at different thicknesses to emissivity at thickness of 0.05μm, at λ = 16.5 μm, are compared. Variation of ε-scaling with thickness ratio for each V-O system is shown in Figure 6.8 and summarized in Table 6.3. It can be seen from this table and the figure that ε-scaling varies linearly with thickness ratio as: ε-scaling = (0.73 $\times$

thickness ratio) + 0.55 (for VO_2); ε-scaling = (0.42 × thickness ratio) + 0.55 (for V_2O_3) and ε-scaling = (0.70 × thickness ratio) + 0.50 (for V_2O_5). This indicates that the slope of this variation is less than one for each of the V-O systems. Furthermore, due to the metallic phase of V_2O_3 at room temperature [189], the slope of the ε-scaling versus thickness ratio for V_2O_3 differs from that of the insulating phase of the other oxides at room temperature. The emissivity of 0.05μm thick film at 16.5 μm varies as V_2O_3 > V_2O_5 > VO_2 such that the emissivity for V_2O_3 is more than twice that for VO_2 or V_2O_5.

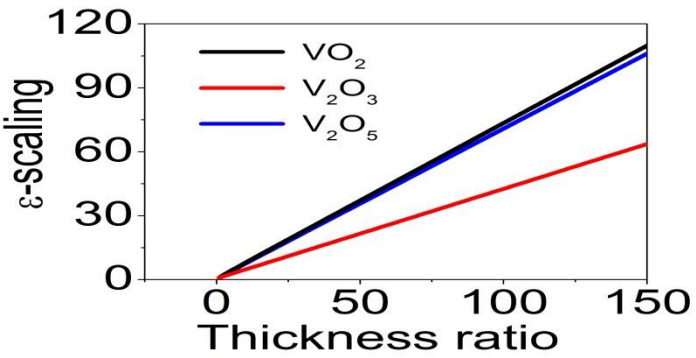

Figure 6.8 Variation of ε-scaling with thickness ratio for each vanadium oxide layer.

Table 6.3 Thickness Dependence of Emissivity for Each V-O System

		VO_2	V_2O_3	V_2O_5
Combination (a)	ε-scaling	73.5000	1.3009	2.0824
	thickness ratio	100.0000	1.7794	2.3364
Combination (b)	ε-scaling	1.5000	1.7027	88.5000
	thickness ratio	1.5974	2.7322	125.0000
Combination (c)	ε-scaling	4.4545	1.3912	2.9016
	thickness ratio	5.0505	1.9920	3.3333
ε at λ = 16.5 μm for 0.05μm thick film		0.1470	0.4410	0.1770

Figure 6.9 shows the emissivity of VO_x in the wavelength range of 2.4-20 μm, with all six possible layer-stacking of its constituents of the three combinations defined by relations (6.6), (6.5) and (6.8). The emissivity change within the entire wavelength range is < 0.085. As can be seen in Figure 6.9, a closer examination within the framework of specified "variation" shows that the wavelength dependent emissivity of all possible layer-stacking completely overlaps, especially in the range of 8-14 µm, for all combinations (a) through (c). In other words, stacking pattern of layers of the three different vanadium oxides has no effect on the emissivity in the region of interest (LWIR). This is an indication that the combined structure of the thin films of vanadium oxides behave as a mixed system instead of thin isolated layered system. In the present simulation, however, the thin film layer of V_2O_3 is stacked on the VO_2 layer with V_2O_5 layer on top of V_2O_3.

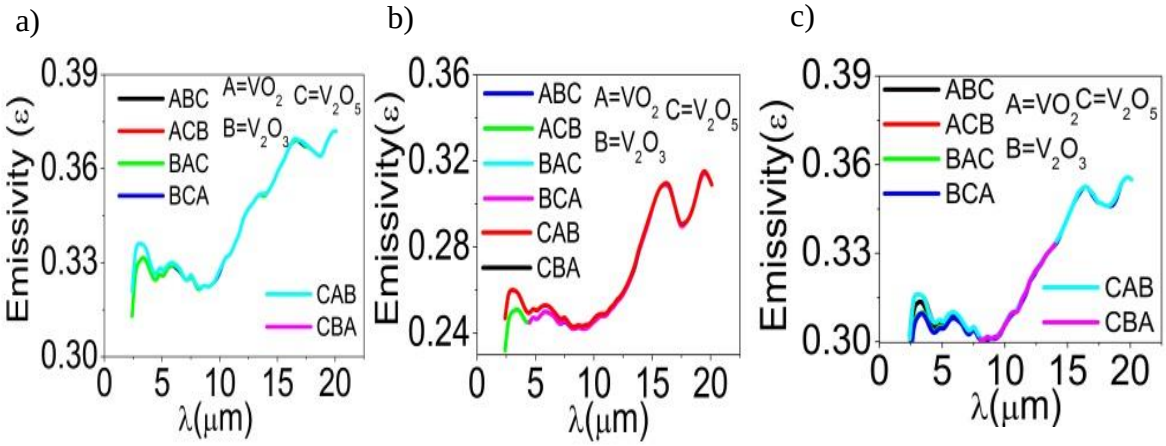

Figure 6.9 Emissivity of VO_x with all six possible layer-stacking of its constituents of the three combinations defined by relations (6.6), (6.5) and (6.8).

Figure 6.10 shows the evolution in emissivity of the microbolometer pixel structure [180] in the wavelength range of 8-14 μm, as the individual component layers

are introduced on top of silicon substrate in the specific pattern of the three combinations defined by relations (6.6), (6.5) and (6.8). It can be seen that the wavelength dependent emissivity for the aluminum-silicon system is minimal. In other words, due to the highly

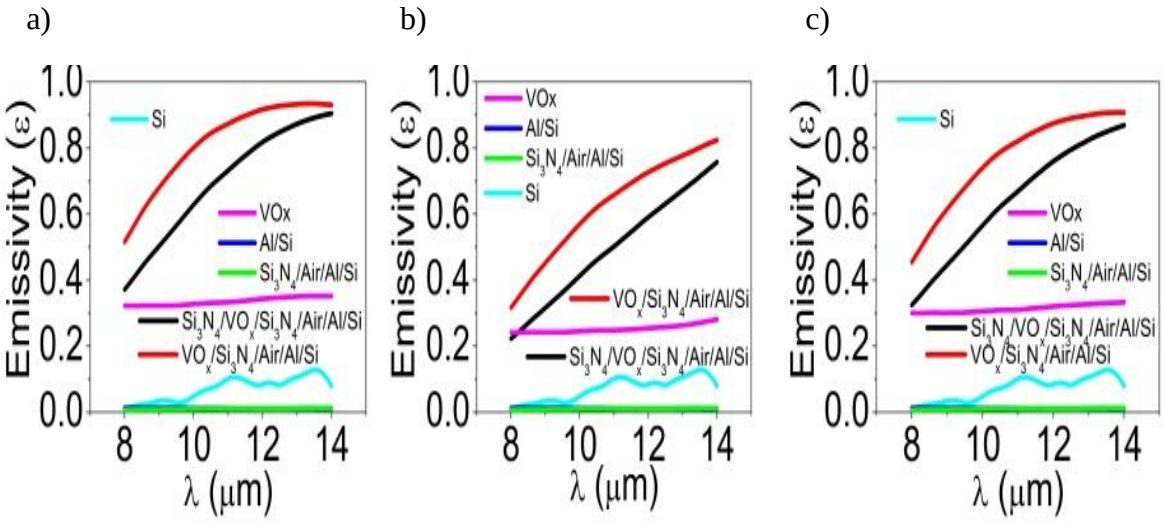

Figure 6.10 Evolution in emissivity of a microbolometer pixel structure [180] with addition of individual constituent layers on top of silicon substrate in the specific order of the three combinations defined by relations (6.6), (6.5) and (6.8).

reflecting nature of Al coating on silicon substrate, emissivity is practically zero over the entire spectral range. Furthermore, the addition of Si_3N_4 overlayer on air/Al/Si has no contribution to the emissivity. The two configurations, without and with Si_3N_4 on top of VO_x/Si_3N_4/Air/Al/Si, hereafter labeled as configuration 1 (Config. 1) and configuration 2 (Config. 2), respectively, show high emissivity throughout the LWIR range; the wavelength dependent variation of emissivity, $(\varepsilon - \lambda)$, in the shorter wavelength of the LWIR range seems to be linear but tends to saturate in the longer wavelengths. It is also apparent that the role of Si_3N_4 overlayer on top of configuration 1, combination (b) is to linearize the spectral emissivity. The arithmetic and weighted averages of emissivity for

the two configurations, in all the three combinations (a) through (c), as defined below, have been presented in Table 6.4.

$$Arithmetic\ mean = \frac{\sum \varepsilon_i}{\sum i} \text{ and } Weighted\ arithmetic\ mean\ = \frac{\sum \varepsilon_i \times \lambda_i}{\sum \lambda_i}$$

The configuration 2 ($Si_3N_4/VO_x/Si_3N_4$/Air/Al/Si) is the structure that is being utilized in the current uncooled VO_x based microbolometer technology, whose average emissivity is reported to be 0.8 [190] in the wavelength range of 8 to 14 microns.

Table 6.4 Emissivity Comparison for the Two Configurations in All Three Combinations (a) through (c)

Emissivity	Combination (a)		Combination (b)		Combination (c)	
	Config. 1	Config. 2	Config. 1	Config. 2	Config. 1	Config. 2
Arithmetic average	0.8197	0.6979	0.6249	0.4973	0.7707	0.6431
Weighted average	0.8393	0.7252	0.6496	0.5240	0.7925	0.6711

Calculations in Table 6.4 show that this Config. 2, with Combination (a), has the weighted average value of emissivity of 0.73. This represents about 8.7% deviation from the reported average emissivity of 0.8 [190] for the "VO_x based industry micro-bolometer". It is interesting to note that the calculated emissivity for Config. 1 is consistently higher than that of Config. 2 and is irrespective of the combination (a), (b) or (c). The overall influence of the top Si_3N_4 layer seems to be to reduce the spectral emissivity of the bolometer structure while at the same time providing the much desired linear performance of the bolometer [Figure 6.10(b)].

6.3 Summary

The analysis of an industry standard VO_x based micro-bolometer [180], with x equal to 1.8 [181], has been performed in the above study. This analysis is based on modeling room temperature spectral emissivity using Multi-Rad, a simulation package that utilizes thin film optics in the form of matrix method of multilayers [175] and assumes the layers to be optically smooth and parallel to each other. The study of spectral emissivity of individual component of bare VO_x, i.e., VO_2, V_2O_3 and V_2O_5, with different thickness shows that the wavelength dependent variation of emissivity, $(\varepsilon - \lambda)$, scales with thickness almost linearly. Unlike the insulating phase (VO_2 and V_2O_5), the metallic phase (V_2O_3) of same thickness shows appreciable emissivity throughout the spectral range and its emissivity is less sensitive to thickness variation. The $(\varepsilon - \lambda)$ of bare VO_x, in the wavelength range of 8-14 μm, with all six possible layer-stacking of its constituents for all three combinations, shows that the stacked layers of the thin films of VO_2, V_2O_3 and V_2O_5, of total thickness of 500Å, behave as a mixed system.

The evolution in the $(\varepsilon - \lambda)$ of the microbolometer pixel structure [180] has been studied in detail by considering the constituent layers, one layer at each step, on top of the silicon substrate in the specific stacking order of the three specific combinations of VO_2, V_2O_3 and V_2O_5 layers. Si_3N_4 overlayer does not change the spectral emissivity of Al/Si while it decreases the spectral emissivity of the VO_x/Si_3N_4/Air/Al/Si system. Calculations show that the Si_3N_4 layer provides the much desired linear performance of the VO_x based bolometer.

CHAPTER 7

CONCLUSIONS

In this study, we have performed one electron Kohn-Sham electronic band-structure calculations of VO_2, V_2O_3 and V_2O_5 in both metallic and insulating phases, implementing a full ab-initio simulation package based on Density Functional Theory (DFT), Plane Waves and Pseudopotentials (PPs). Electronic band structures are found to be influenced by crystal structure, crystal field splitting and strong hybridization between 2p (O) and 3d (V) bands. Bands in V_2O_5 are remarkably dispersive to different extents, along various high symmetry lines in the Brillouin zone (BZ). This implies that the crystal structure is highly anisotropic. A group of conduction bands (with narrow band width, called intermediate bands), lying close (0.6 eV apart) to higher conduction bands, observed in V_2O_5, play a critical role in optical and thermoelectric processes. An indirect gap of 1.7 eV is observed between T and Γ points of the BZ, which is close to the value of 1.74 eV reported in similar calculations but is smaller than the experimental value of 2.2 eV [105]. This underestimation of the band gap is inherent with DFT.

Similar calculations have been performed in both metallic and insulating phases of bulk vanadium dioxide (VO_2) and sesquioxide (V_2O_3). In the metallic phase, we see finite overlapping of valence and conduction bands. Bands in insulating phases appear in similar locations as in corresponding metallic phases. However, the numbers of bands are doubled in the insulating phases (as compared to corresponding metallic counterpart), which is consistent with the fact that the number of formula units of the unit cell, in the calculations, is doubled in each oxide during phase transition from metallic to insulating phase. Even though an optical gap is not observed in the insulating phase (shortcomings

of LDA), we have noticed some differences in the band structures that characterize phase- whether insulating or metallic. In insulating phase, (a) number of bands crossing the Fermi level is less, (b) bands corresponding to "valence electrons" considered in the pseudopotential are fully occupied, unlike in the metallic phase.

Transport parameters such as Seebeck coefficient, electrical conductivity and thermal (electronic) conductivity are studied as a function of temperature at a fixed value of chemical potential close to the Fermi energy using Kohn-Sham band structure approach coupled with Boltzmann transport equations. Among the three oxides of our interest, in the present study, only V_2O_5 exhibits significant thermoelectric (TE) properties that are found to be consistent with the literature. A comparison of averaged electrical conductivity with that of as-deposited as well as post-annealed V_2O_5 films has shown the value of momentum relaxation time to be $\sim 10^{-18}$ s. For understanding the effect of phase transition on transport properties, we have also calculated the thermoelectric properties of vanadium dioxide, VO_2, for both metallic and insulating phases. The absolute value of Seebeck coefficient increases monotonically with temperature in the metallic phase while it decreases monotonically with temperature in the insulating phase. Seebeck coefficient, at an experimental critical temperature of 340K, is found to change by 18.9 μV/K which lies within 10% of the observed discontinuity of 17.3 μV/K during the phase transition. "Kohn-Sham-Boltzmann" approach can predict phase transition in VO_2 with reasonable accuracy.

Numerical methods have been used to analyze the optical properties of bulk and thin films of VO_2, V_2O_3, and V_2O_5, deposited on Al_2O_3 substrates, from infrared to vacuum ultraviolet range (up to 12 eV), based on the data available in the literature. The

observed peaks in the corresponding spectra have been interpreted and compared as a function of structure, polarization and temperature. The anisotropy is significant in the infrared region for VO_2 and in the visible region for V_2O_5. Penn model has been used to explain the energies corresponding to the peaks in the R-E spectra of the single crystal of the V-O systems at room temperature. E_p values for VO_2 and V_2O_5 are close to the average of energies corresponding to the peaks ($\overline{E}$) while their values are even closer in V_2O_3, reflecting the degree of anisotropy in the order of $V_2O_3 < VO_2 < V_2O_5$. The vanadium oxygen bonds are highly ionic and undergo IMT at T_c as a function of oxidation state of the vanadium ion i.e. the transition temperature increases with oxidation states of the vanadium atom. Optical transitions and effective number of electrons participating in these processes are described from the ϵ_2-E spectra and its numerical integration using the well-known sum rule. The results of these calculations show that the optical transitions from valence to conduction band occur including the transition from 2p (O) to 3d (V) bands and the inter band transitions within the d bands. The optical spectra has no indication of the transition occurring from occupied to empty states within the d band for V_2O_3 and V_2O_5 systems but the intra band transition seems to occur in VO_2. The change in n_{eff} with respect to the energy of incident photons is also calculated and it is found that this change is consistent with the peaks observed in the ϵ_2-E spectra.

In the Honeywell microbolometer structure, the bolometer sensing element has been chosen to be VO_x, with x equal to 1.8, along with other layers of Si_3N_4, air, Al and Si. The room temperature spectral emissivity of such layered structure is analyzed using Multi-Rad, a simulation package that utilizes thin film optics in the form of matrix

method of multilayers. The study of spectral emissivity of individual components of bare VO_x, i.e., VO_2, V_2O_3 and V_2O_5, with different thickness shows that the wavelength dependent variation of emissivity, $(\varepsilon - \lambda)$, scales with thickness almost linearly. Unlike the insulating phase (VO_2 and V_2O_5), the metallic phase (V_2O_3) of same thickness shows appreciable emissivity throughout the spectral range and its emissivity is less sensitive to thickness variation. The $(\varepsilon - \lambda)$ of bare VO_x, in the wavelength range of 8-14 μm, shows that the stacked layers of the thin films of VO_2, V_2O_3 and V_2O_5, of total thickness of 500Å, behave as a mixed system.

The evolution in the $(\varepsilon - \lambda)$ of the microbolometer pixel structure [180] has been studied in detail by considering the constituent layers, one layer at each step, on top of the silicon substrate in the specific stacking order of the three specific combinations of VO_2, V_2O_3 and V_2O_5 layers. Si_3N_4 overlayer does not change the spectral emissivity of Al/Si while it decreases the spectral emissivity of the VO_x/Si_3N_4/Air/Al/Si system. Calculations show that the Si_3N_4 layer provides the much desired linear performance of the VO_x based bolometer.

REFERENCES

1. Darling, R.B., Iwanaga, S. (2009). Structure, properties, and MEMS and microelectronic applications of vanadium oxides. *Sadhana, 34*, 531-542.

2. Adler, D. (1968). Mechanisms for Metal-Nonmental Transitions in Transition-Metal Oxides and Sulfides. *Reviews of Modern Physics, 40*, 714-736.

3. Parker, J.C., Geiser, U.W., Lam, D.J., Xu, Y. & Ching, W.Y. (1990). Optical Properties of the Vanadium Oxides VO_2 and V_2O_5. *Journal of the American Ceramic Society, 73*, 3206-3208.

4. Henrich, V.E., Cox, P.A. (1996). *The Surface Science of Metal Oxides*. Cambridge, United Kingdom: Cambridge University Press.

5. Imada, M., Fujimori, A. & Tokura, Y. (1998). Metal-insulator transitions. *Reviews Modern Physics, 70*, 1039-1263.

6. Fierro, J.L.G. (ed.) (2006). *Metal Oxides: Chemistry and Applications*. Boca Raton, Florida: CRC Press.

7. http://www.cpfs.mpg.de/~kasinath/. (accessed on 11/27/2014).

8. Wu, C., Feng, F. & Xie, Y. (2013). Design of vanadium oxide structures with controllable electrical properties for energy applications. *Chemical Society Reviews, 42*, 5157-5183.

9. Lalena, J.N., Cleary, D.A. (2005). *Principles of Inorganic Materials Design*. Hoboken, New Jersey: John Wiley & Sons, Inc.

10. deBoer, J.H., Verwey, E.J.W. (1937). Semi-conductors with partially and with completely filled 3d-lattice bands. *Proceedings of the Physical Society, 49*, 59-71.

11. Adler, D., Brooks, H. (1967). Theory of Semiconductor-To-metal Transitions. *Physical Review, 155*, 826-840.

12. Emin, D. (1982). Small polarons. *Physics Today, 35*, 34-40.

13. Hurd, C.M. (1985). Quantum tunnelling and the temperature dependent DC conduction in low-conductivity semiconductors. *Journal of Physics C: Solid State Physics, 18*, 6487-6499.

14. Bruce, P.G. (1997). *Solid State Electrochemistry*. Cambridge, United Kingdom: Cambridge University Press.

15. Tredgold, R.H. (1962). On Very Low Mobility Carriers. *Proceedings of the Physical Society, 80*, 807-810.

16. Mott, N.F., Peierls, R. (1937). Discussion of the paper by de Boer and Verwey. *Proceedings of the Physical Society, 49*, 72-73.

17. Mott, N.F. (1949). The Basis of the Electron Theory of Metals, with Special Reference to the Transition Metals. *Proceedings of the Physical Society. Section A, 62*, 416-422.

18. Mott, N.F. (1961). The transition to the metallic state. *Philosophical Magazine, 6*, 287-309.

19. Hubbard, J. (1964). Electron Correlations in Narrow Energy Bands. III. An Improved Solution. *Proceedings of the Royal Society of London. Series A, 281*, 401-419.

20. Gebhard, F. (1997). *The Mott Metal-Insulator Transition: Models and Methods, Issue 137*. New York: Springer.

21. Wentzcovitch, R.M., Schulz, W.W. & Allen, P.B. (1994). VO_2: Peierls or Mott-Hubbard? A view from band theory. *Physical Review Letters, 72*, 3389-3392.

22. Biermann, S., Poteryaev, A., Lichtenstein, A.I. & Georges, A. (2005). Dynamical singlets and correlation-assisted peierls transition in VO_2. *Physical Review Letters, 94*, 026404 (4 pages).

23. Peierls, R.E. (1955). *Quantum Theory of Solid*. London: Oxford University.

24. Gruner, G. (1988). The dynamics of charge-density waves. *Reviews of Modern Physics, 60*, 1129-1181.

25. Kuper, C.G. (1955). On the Thermal Properties of Fröhlich's One-Dimensional Superconductor. *Proceedings of the Royal Society of London. Series A, Mathematical and Physical Sciences, 227*, 214-228.

26. Rice, T.M., Launois, H. & Pouget, J.P. (1994). Comment on "VO_2: Peierls or Mott-Hubbard? A View from Band Theory". *Physical Review Letters, 73*, 3042-3042.

27. Kotliar, G., Vollhardt, D. (2004). Strongly Correlated Materials: Insights from Dynamical Mean-Field Theory. *Physics Today, 57*, 53-59.

28. Zylbersztejn, A., Mott, N.F. (1975). Metal-insulator transition in vanadium dioxide. *Physical Review B, 11*, 4383-4395.

29. Morin, F. (1959). Oxides which show Metal-to-Insulator Transitions at the Neel Temperature. *Physical Review Letters, 3*, 34-36.

30. Nadkarni, G.S., Shirodkar, V.S. (1983). Experiment and theory for switching in Al/V_2O_5/Al devices. *Thin Solid Films, 105*, 115-129.

31. Lamb, D.M. (2009). *Semiconductor to Metalic Phase Transitions from Vanadium and Titanium Oxides Induced by Visible Light*. Missouri State University, Springfield.

32. Batista, C., Ribeiro, R.M. & Teixeira, V. (2011). Synthesis and characterization of VO_2-based thermochromic thin films for energy-efficient windows. *Nanoscale Research Letters, 6*, 301 (7 pages).

33. Cavalleri, A., Tóth, C., Siders, C.W., Squier, J.A., Ráksi, F., Forget, P. & Kieffer, J.C. (2001). Femtosecond Structural Dynamics in VO_2 during an Ultrafast Solid-Solid Phase Transition. *Physical Review Letters, 87*, 237401 (4 pages).

34. Wessel, C., Reimann, C., Müller, A., Weber, D., Lerch, M., Ressler, T., Bredow, T. & Dronskowski, R. (2012). Electronic structure and thermodynamics of V_2O_3 polymorphs. *Journal of Computational Chemistry, 33*, 2102-2107.

35. Chain, E.E. (1991). Optical properties of vanadium dioxide and vanadium pentoxide thin films. *Applied Optics, 30*, 2782-2787.

36. Dernier, P.D., Marezio, M. (1970). Crystal Structure of the Low-Temperature Antiferromagnetic Phase of V_2O_3. *Physical Review B, 2*, 3771-3776.

37. Chudnovskiy, F., Luryi, S. & Spivak, B. (2002). Switching device based on first-order metalinsulator transition induced by external electric field. In: Luryi, S., Xu, J.M., Zaslavsky, A. (Eds.), *Future Trends in Microelectronics: the Nano Millennium*, pages 148-155. Hoboken, New Jersey: John Wiley & Sons, Inc.

38. Blum, R.-P., Niehus, H., Hucho, C., Fortrie, R., Ganduglia-Pirovano, M.V., Sauer, J., Shaikhutdinov, S. & Freund, H.-J. (2007). Surface Metal-Insulator Transition on a Vanadium Pentoxide (001) Single Crystal. *Physical Review Letters, 99*, 226103 (4 pages).

39. Kang, M., Kim, I., Kim, S.W., Ryu, J.-W. & Park, H.Y. (2011). Metal-insulator transition without structural phase transition in V_2O_5 film. *Applied Physics Letters, 98*, 131907 (3 pages).

40. Liu, W.-T., Cao, J., Fan, W., Hao, Z., Martin, M.C., Shen, Y.R., Wu, J. & Wang, F. (2011). Intrinsic Optical Properties of Vanadium Dioxide near the Insulator−Metal Transition. *Nano Letters, 11*, 466-470.

41. Pergament, A.L. (2011). Metal-Insulator Transition Temperatures and Excitonic Phases in Vanadium Oxides. *ISRN Condensed matter Physics*, Article ID 605913 (5 pages). doi:10.5402/2011/605913.

42. Granqvist, C.G. (1985). Spectrally Selective Coatings for Energy Efficiency and Solar Applications. *Physica Scripta, 32*, 401-407.

43. Simic-Milosevic, V., Nilius, N., Rust, H.-P. & Freund, H.-J. (2008). Local band gap modulations in non-stoichiometric V_2O_3 films probed by scanning tunneling spectroscopy. *Physical Review B, 77*, 125112 (5 pages).

44. Kana Kana, J.B., Ndjaka, J.M., Owono Ateba, P., Ngom, B.D., Manyala, N., Nemraoui, O., Beye, A.C. & Maaza, M. (2008). Thermochromic VO_2 thin films synthesized by rf-inverted cylindrical magnetron sputtering. *Applied Surface Science, 254*, 3959-3963.

45. Thomas, M.S., DeNatale, J.F. & Hood, P.J. (1997). High–temperature optical properties of thin–film vanadium oxides–VO_2 and V_2O_3. *Materials Research Society Symposium Proceedings, 479*, 161-166.

46. Zhang, Z., Gao, Y., Luo, H., Kang, L., Chen, Z., Du, J., Kanehira, M., Zhang, Y. & Wang, Z.L. (2011). Solution-based fabrication of vanadium dioxide on F:SnO_2 substrates with largely enhanced thermochromism and low-emissivity for energy-saving applications. *Energy & Environmental Science, 4*, 4290-4297.

47. Granqvist, C.G. (1995). *Handbook of Inorganic Electrochromic Materials*. Amsterdam, Holland: Elsevier Science.

48. Gupta, A., Aggarwal, R., Gupta, P., Dutta, T., Narayan, R.J. & Narayan, J. (2009). Semiconductor to metal transition characteristics of VO_2 thin films grown epitaxially on Si (001). *Applied Physics Letters, 95*, 111915 (3 pages).

49. Driscoll, T., Kim, H.-T., Chae, B.-G., Ventra, M.D. & Basov, D.N. (2009). Phase-transition driven memristive system. *Applied Physics Letters, 95*, 043503 (3 pages).

50. de Almeida, L.A.L., Deep, G.S., Lima, A.M.N. & Neff, H. (2000). Thermal dynamics of VO_2 films within the metal–insulator transition: Evidence for chaos near percolation threshold. *Applied Physics Letters, 77*, 4365 (3 pages).

51. Niklaus, F., Decharat, A., Jansson, C. & Stemme, G. (2008). Performance model for uncooled infrared bolometer arrays and performance predictions of bolometers operating at atmospheric pressure. *Infrared Physics & Technology, 51*, 168-177.

52. Rajendra Kumar, R.T., Karunagaran, B., Mangalaraj, D., Narayandass, Sa.K., Manoravi, P., Joseph, M. & Gopal, V. (2003). Pulsed laser deposited vanadium oxide thin films for uncooled infrared detectors. *Sensors and Actuators A: Physical, 107*, 62-67.

53. Cole, B.E., Higashi, R.E. & Wood, R.A. (1998). Monolithic two-dimensional arrays of micromachined microstructures for infrared applications. *Proceedings of the IEEE, 86*, 1679-1686.

54. Landgrebe, A.R., Klingler, R.J. (2001). *Interfaces, Phenomena and Nanostructures in Lithium Batteries: Proceedings*. New Jersey: The Electrochemical Society, Inc.

55. Kiehne, H.A. (2003). *Battery Technology Handbook*. New York: Marcel Dekker, Inc.

56. Walia, S., Balendhran, S., Nili, H., Zhuiykov, S., Rosengarten, G., Wang, Q.H., Bhaskaran, M., Sriram, S., Strano, M.S. & Kalantar-zadeh, K. (2013). Transition metal oxides – Thermoelectric properties. *Progress in Materials Science, 58*, 1443-1489.

57. El Mandouh, Z.S., Selim, M.S. (2000). Physical properties of vanadium pentoxide sol gel films. *Thin Solid Films, 371*, 259-263.

58. Driscoll, T., Kim, H.-T., Chae, B.-G., Kim, B.-J., Lee, Y.-W., Jokerst, N.M., Palit, S., Smith, D.R., Ventra, M.D. & Basov, D.N. (2009). Memory Metamaterials. *Science, 325*, 1518-1521.

59. Driscoll, T., Palit, S., Qazilbash, M.M., Brehm, M., Keilmann, F., Chae, B.-G., Yun, S.-J., Kim, H.-T., Cho, S.Y., Jokerst, N.M., Smith, D.R. & Basov, D.N. (2008). Dynamic tuning of an infrared hybrid-metamaterial resonance using vanadium dioxide. *Applied Physics Letters, 93*, 024101 (3 pages).

60. Dicken, M.J., Aydin, K., Pryce, I.M., Sweatlock, L.A., Boyd, E.M., Walavalkar, S., Ma, J. & Atwater, H.A. (2009). Frequency tunable near-infrared metamaterials based on VO_2 phase transition. *Optics Express, 17*, 18330-18339.

61. Kyoung, J.S., Seo, M.A., Koo, S.M., Park, H.R., Kim, H.S., Kim, B.J., Kim, H.T., Park, N.K., Kim, D.S. & Ahn, K.J. (2011). Active terahertz metamaterials: Nano-slot antennas on VO_2 thin films. *Physica Status Solidi C, 8*, 1227-1230.

62. Hilton, D.J., Prasankumar, R.P., Fourmaux, S., Cavalleri, A., Brassard, D., Khakani, M.A.E., Kieffer, J.C., Taylor, A.J. & Averitt, R.D. (2007). Enhanced Photosusceptibility near T_c for the Light-Induced Insulator-to-Metal Phase Transition in Vanadium Dioxide. *Physical Review Letters, 99*, 226401 (4 pages).

63. Baldassarre, L., Perucchi, A., Nicoletti, D., Toschi, A., Sangiovanni, G., Held, K., Capone, M., Ortolani, M., Malavasi, L., Marsi, M., Metcalf, P., Postorino, P. & Lupi, S. (2008). Quasiparticle evolution and pseudogap formation in V_2O_3: An infrared spectroscopy study. *Physical Review B, 77*, 113107 (4 pages).

64. Perucchi, A., Baldassarre, L., Postorino, P. & Lupi, S. (2009). Optical properties across the insulator to metal transitions in vanadium oxide compounds. *Journal of Physics: Condensed Matter, 21*, 323202 (17 pages).

65. Losurdoa, M., Barreca, D., Bruno, G. & Tondello, E. (2001). Spectroscopic ellipsometry investigation of V_2O_5 nanocrystalline thin films. *Thin Solid Films, 384*, 58-64.

66. Mott, N.F. (1964). Electrons in transition metals. *Advances in Physics, 13*, 325-422.

67. Gunnarsson, O. (1976). Band model for magnetism of transition metals in the spin-density-functional formalism. *Journal of Physics F: Metal Physics, 6*, 587-606.

68. Aurelian, C., Julien, G., Pierre, B., Jean-Christophe, O., Corinne, C. & Alain, C. (2010). Exploiting the Semiconductor-Metal Phase Transition of VO_2 Materials: a Novel Direction towards Tuneable Devices and Systems for RF-Microwave Applications. In: Mukherjee, M. (Ed.), *Advanced Microwave and Millimeter Wave Technologies Semiconductor Devices Circuits and Systems*, pages 35-56. Vukovar, Croatia: In-Tech.

69. Levine, I.N. (1999). *Quantum Chemistry*. Upper Saddle River, New Jersey: Prentice-Hall.

70. Ohno, K., Esfarjani, K. & Kawazoe, Y. (1999). *Computational Materials Science*. Berlin: Springer.

71. Szabo, A., Ostlund, N.S. (1989). *Modern Quantum Chemistry*. New York: Dover Publications.

72. Lamsal, C., Mishra, D.R. & Ravindra, N.M. (2014). Equilibrium configuration of $(H_2O)_n$, for n = 1-3. *Nanomaterials and Energy, 3*, 129 -138.

73. Foresman, J.B., Frisch, Æ. (1999). *Exploring Chemistry with Electronic Structure Methods*. Pennsylvania: Gaussian, Inc. Pittsburgh.

74. Thijssen, J. (2001). *Computational Physics*. Cambridge: Cambridge University Press.

75. Thomas, L.H. (1927). The calculation of atomic fields. *Mathematical Proceedings of the Cambridge Philosophical Society, 23*, 542-548.

76. Fermi, E. (1927). Un Metodo Statistico per la Determinazione di alcune Prioprietà dell'Atomo. *Rend. Accad. Naz. Lincei 6*, 602-607.

77. Hohenberg, P., Kohn, W. (1964). Inhomogeneous Electron Gas. *Physical Review, 136*, B864-B871.

78. Sholl, D., Steckel, J.A. (2011). *Density Functional Theory: A Practical Introduction*. Hoboken, New Jersey: John Wiley & Sons, Inc.

79. Torrent, M., March 30 - April 5 (2008). *International School on Vibrational Spectroscopies: A Hands-on Introduction to ABINIT.* Queretaro, Mexico.

80. Martin, R.M. (2004). *Electronic Structure: Basic Theory and Practical Methods*. Cambridge: Cambridge University Press.

81. Hamann, D.R., Schlüter, M. & Chiang, C. (1979). Norm-Conserving Pseudopotentials. *Physical Review Letters, 43,* 1494-1497.

82. Kohanoff, J. (2006). *Electronic Structure Calculations for Solids and Molecules: Theory and Computational Methods*. Cambridge: Cambridge University Press.

83. Vanderbilt, D. (1990). Soft self-consistent pseudopotentials in a generalized eigenvalue formalism. *Physical Review B, 41*, 7892-7895.

84. Blöchl, P.E. (1994). Projector augmented-wave method. *Physical Review B, 50,* 17953-17979.

85. Kresse, G., Joubert, D. (1999). From ultrasoft pseudopotentials to the projector augmented-wave method. *Physical Review B, 59*, 1758-1775.

86. Monkhorst, H.J., Pack, J.D. (1976). Special points for Brillouin-zone integrations. *Physical Review B, 13*, 5188-5192.

87. Mermin, N.D. (1965). Thermal Properties of the Inhomogeneous Electron Gas. *Physical Review, 137*, A1441-A1443.

88. Gonze, X., Amadon, B., Anglade, P.M., Beuken, J.M., Bottin, F., Boulanger, P., Bruneval, F., Caliste, D., Caracas, R., Côté, M., Deutsch, T., Genovese, L., Ghosez, P., Giantomassi, M., Goedecker, S., Hamann, D.R., Hermet, P., Jollet, F., Jomard, G., Leroux, S., Mancini, M., Mazevet, S., Oliveira, M.J.T., Onida, G., Pouillon, Y., Rangel, T., Rignanese, G.M., Sangalli, D., Shaltaf, R., Torrent, M., Verstraete, M.J., Zerah, G. & Zwanziger, J.W. (2009). ABINIT: First-principles approach to material and nanosystem properties. *Computer Physics Communications, 180*, 2582-2615.

89. Gonze, X. (2005). A brief introduction to the ABINIT software package. *Zeitschrift für Kristallographie, 220,* 558-562.

90. Pulay, P. (1980). Convergence acceleration of iterative sequences. the case of scf iteration. *Chemical Physics Letters, 73*, 393-398.

91. http://www.abinit.org. (accessed on 11/27/2014).

92. Holzwarth, N.A.W., Tackett, A.R. & Matthews, G.E. (2001). A Projector Augmented Wave (PAW) code for electronic structure calculations, Part I: atompaw for generating atom-centered functions. *Computer Physics Communications, 135,* 329-347.

93. http://users.wfu.edu/natalie/papers/pwpaw/man.html. (accessed on 11/27/2014).

94. Stewart, G. (2012). *Electronic Band Structure of Bulk and Monolayer V_2O_5*. Case Western Reserve University, Cleveland.

95. Perdew, J.P., Wang, Y. (1992). Accurate and simple analytic representation of the electron-gas correlation energy. *Physical Review B, 45,* 13244-13249.

96. Longo, J.M., Kierkegaard, P., Ballhausen, C.J., Ragnarsson, U., Rasmussen, S.E., Sunde, E. & Sørensen, N.A. (1970). A Refinement of the Structure of VO_2. *Acta Chemica Scandinavica, 24*, 420-426.

97. Eyert, V. (2002). The metal-insulator transitions of VO_2: A band theoretical approach. *Annalen der Physik, 11,* 650-704.

98. Kokalj, A. (1999). XCrySDen—a new program for displaying crystalline structures and electron densities. *Journal of Molecular Graphics and Modelling, 17*, 176-179.

99. Schwingenschlögl, U. (2003). *The Interplay of Structural and Electronic Properties in Transition Metal Oxides*. University of Augsburg, 86135 Augsburg, Germany.

100. Enjalbert, R., Galy, J. (1986). A refinement of the structure of V_2O_5. *Acta Crystallographica Section C, 42*, 1467-1469.

101. Aroyo, M.I., Perez-Mato, J.M., Orobengoa, D., Tasci, E., De La Flor, G. & Kirov, A. (2011). Crystallography online: Bilbao crystallographic server. *Bulgarian Chemical Communications, 43,* 183-197.

102. Aroyo Mois, I., Perez-Mato Juan, M., Capillas, C., Kroumova, E., Ivantchev, S., Madariaga, G., Kirov, A. & Wondratschek, H. (2006). Bilbao Crystallographic Server: I. Databases and crystallographic computing programs. *Zeitschrift für Kristallographie, 221,* 15-27.

103. Aroyo, M.I., Kirov, A., Capillas, C., Perez-Mato, J.M. & Wondratschek, H. (2006). Bilbao Crystallographic Server. II. Representations of crystallographic point groups and space groups. *Acta Crystallographica Section A, 62,* 115-128.

104. http://www.cryst.ehu.es/cgi-bin/cryst/programs/nph-wp-list. (accessed on 11/27/2014).

105. Eyert, V., Höck, K.H. (1998). Electronic structure of V_2O_5: Role of octahedral deformations. *Physical Review B, 57*, 12727-12737.

106. Madsen, G.K.H., Singh, D.J. (2006). BoltzTraP. A code for calculating band-structure dependent quantities. *Computer Physics Communications, 175*, 67-71.

107. Reshak, A.H., Khan, S.A. & Auluck, S. (2014). Thermoelectric properties of a single graphene sheet and its derivatives. *Journal of Materials Chemistry C, 2*, 2346-2352.

108. Hoffmann, R. (1988). *Solids and surfaces: a chemist's view of bonding in extended structures*. Germany: VCH Publishers.

109. Izi̯umov, Yu.A., Syromyatnikov, V.N. (1990). *Phase Transitions and Crystal Symmetry*. New York: Springer.

110. Yu, P., Cardona, M. (2010). *Fundamentals of Semiconductors: Physics and Materials Properties*. New York: Springer.

111. Zimmermann, R., Claessen, R., Reinert, F., Steiner, P. & Hüfner, S. (1998). Strong hybridization in vanadium oxides: evidence from photoemission and absorption spectroscopy. *Journal of Physics: Condensed Matter, 10*, 5697-5716.

112. Jakub, G., Robert, G., Małgorzata, W. & Jürgen, H. (2009). Relative stability of low-index V_2O_5 surfaces: a density functional investigation. *Journal of Physics: Condensed Matter, 21*, 095008 (8 pages).

113. Yu, C., Santos, J.R., Ferreira, I., Termentzidis, K., Pokropivny, A., Xiong, S.Y., Cortona, P. & Volz, S. (2012). Thermoelectric transport in V_2O_5 thin films. *Journal of Physics: Conference Series, 395*, 012016 (6 pages).

114. Parker, J.C., Lam, D.J., Xu, Y.-N. & Ching, W.Y. (1990). Optical properties of vanadium pentoxide determined from ellipsometry and band-structure calculations. *Physical Review B, 42*, 5289-5293.

115. Mokerov, V.G., Makarov, V.L., Tulvinskii, V.B. & Begishev, A.R. (1976). Optical properties of vanadium pentoxide in the region of photon energies from 2 eV to 14 eV. *Optics and Spectroscopy, 40*, 58-61.

116. Lamsal, C., Ravindra, N.M. (2014). Vanadium Oxides for Energy and Security Applications. In: Dwivedi, Y., Rai S.B. & Singh, J.P. (Eds.), *Spectroscopic Techniques for Security, Forensic and Environmental Applications*, pages 195-220. Hauppauge, New York: Nova Science Publishers.

117. Yu, B., Chen, D., Li, Y. & Jia, Y. (2012). Predictions of high-pressure structural, electronic and thermodynamic properties of α-Si_3N_4. *Acta Metallurgica Sinica (English Letters), 25*, 131-140.

118. Qazilbash, M.M., Schafgans, A.A., Burch, K.S., Yun, S.J., Chae, B.G., Kim, B.J., Kim, H.T. & Basov, D.N. (2008). Electrodynamics of the vanadium oxides VO_2 and V_2O_3. *Physical Review B, 77*, 115121 (10 pages).

119. Continenza, A., Massidda, S. & Posternak, M. (1999). Self-energy corrections in VO_2 within a model GW scheme. *Physical Review B, 60*, 15699-15704.

120. Kozhevnikov, A.V., Anisimov, V.I. & Korotin, M.A. (2007). Calculation of the electronic structure of the vanadium dioxide VO_2 in the monoclinic low-temperature phase M_1 using the generalized transition state method. *The Physics of Metals and Metallography, 104*, 215-220.

121. Mattheiss, L.F. (1994). Band properties of metallic corundum-phase V_2O_3. *Journal of Physics: Condensed Matter, 6*, 6477-6484.

122. Ezhov, S.Y., Anisimov, V.I., Khomskii, D.I. & Sawatzky, G.A. (1999). Orbital Occupation, Local Spin, and Exchange Interactions in V_2O_3. *Physical Review Letters, 83*, 4136-4139.

123. Saha-Dasgupta, T., Andersen, O.K., Nuss, J., Poteryaev, A.I., Georges, A. & Lichtenstein, A.I. (2009). Electronic structure of V_2O_3: Wannier orbitals from LDA-NMTO calculations. *arXiv:0907.2841*.

124. Thomas, G.A., Rapkine, D.H., Carter, S.A. & Millis, A.J. (1994). Observation of the Gap and Kinetic Energy in a Correlated Insulator. *Physical Review Letters, 73*, 1529-1532.

125. Held, K., Keller, G., Eyert, V., Vollhardt, D. & Anisimov, V.I. (2001). Mott-Hubbard Metal-Insulator Transition in Paramagnetic V_2O_3: An LDA+DMFT (QMC) Study. *Physical Review Letters, 86*, 5345-5348.

126. Xu, B., Verstraete, M.J. (2013). First principles explanation of the positive Seebeck coefficient of lithium. *arXiv:1311.6805*.

127. Reshak, A.H. (2014). $Fe_2MnSi_xGe_{1-x}$: influence thermoelectric properties of varying the germanium content. *RSC Advances, 4*, 39565-39571.

128. Ernst, A., Sandratskii, L.M., Bouhassoune, M., Henk, J. & Lüders, M. (2005). Weakly Dispersive Band near the Fermi Level of GaMnAs Due to Mn Interstitials. *Physical Review Letters, 95*, 237207 (4 pages).

129. Sotojima, K., Suzuki, R.O., Amezawa, K. & Tomii, Y. (2007). Thermoelectric Properties and Phase Transition of $(Zn_xCu_{2-x})V_2O_7$. *Journal of the Japan Society of Powder and Powder Metallurgy, 54*, 356-361.

130. Berglund, C.N., Guggenheim, H.J. (1969). Electronic Properties of VO_2 near the Semiconductor-Metal Transition. *Physical Review, 185*, 1022-1033.

131. Austin, I.G., Turner, C.E. (1969). The nature of the metallic state in V_2O_3 and related oxides. *Philosophical Magazine, 19*, 939-949.

132. Santos, R., Loureiro, J., Nogueira, A., Elangovan, E., Pinto, J.V., Veiga, J.P., Busani, T., Fortunato, E., Martins, R. & Ferreira, I. (2013). Thermoelectric properties of V_2O_5 thin films deposited by thermal evaporation. *Applied Surface Science, 282*, 590-594.

133. Chumakov, Y., Xiong, S.Y., Santos, J.R., Ferreira, I., Termentzidis, K., Pokropivny, A., Cortona, P. & Volz, S. (2013). Ab Initio Calculations and Measurements of Thermoelectric Properties of V_2O_5 Films. *Journal of Electronic Materials, 42*, 1597-1603.

134. Surnev, S., Ramsey, M.G. & Netzer, F.P. (2003). Vanadium oxide surface studies. *Progress in Surface Science, 73*, 117-165.

135. Scanlon, D.O., Walsh, A., Morgan, B.J. & Watson, G.W. (2008). An ab initio study of reduction of V_2O_5 through the formation of oxygen vacancies and Li intercalation. *The Journal of Physical Chemistry C, 112*, 9903-9911.

136. Cardona, M. (1970). Optical Properties and Electronic Density of States. *Journal of Research of the National Bureau of Standards-A. Physics and Chemistry, 74A*, 253-265.

137. Cardona, M. (1965). Infrared Dielectric Constant and Ultraviolet Optical Properties of Solids with Diamond, Zinc Blende, Wurtzite, and Rocksalt Structure. *Journal of Applied Physics, 36*, 2181-2186.

138. Penn, D.R. (1962). Wave-Number-Dependent Dielectric Function of Semiconductors. *Physical Review, 128*, 2093-2097.

139. Van Vechten, J.A. (1969). Quantum Dielectric Theory of Electronegativity in Covalent Systems. I. Electronic Dielectric Constant. *Physical Review, 182*, 891-905.

140. Phillips, J.C. (1973). *Bonds and bands in semiconductors*. New York: Academic.

141. Verleur, H.W., Barker, A.S. & Berglund, C.N. (1968). Optical Properties of VO_2 between 0.25 and 5 eV. *Physical Review, 172*, 788-798.

142. Zhuze, V.P., Andreev, A.A. & Shelykh, A.I. (1969). The Hall Effect in V_2O_3 Single Crystals in the Metallic Conductivity Region. *Soviet Physics - Solid State, 10*, 2914-2916.

143. Andrianov, G.O., Aronov, A.G., Smirnova, T.V. & Chudnovskii, F.A. (1973). The optical absorption by the frenkel exciton in V_2O_3. *Physica Status Solidi B, 60*, 79-84.

144. Fujiwara, H. (2007). *Spectroscopic Ellipsometry: Principles and Applications*. New Jersey: John Wiley & Sons, Inc.

145. Guang-Huaa, L., Xiao-Yan, D. & Chun-Hai, W. (2011). Electronic and Optical Properties of Monoclinic and Rhombohedral Vanadium Sesquioxide. *Chinese Journal of Structural Chemistry, 30*, 638-643.

146. Shin, S., Suga, S., Taniguchi, M., Fujisawa, M., Kanzaki, H., Fujimori, A., Daimon, H., Ueda, Y., Kosuge, K. & Kachi, S. (1990). Vacuum-ultraviolet reflectance and photoemission study of the metal-insulator phase transitions in VO_2, V_6O_{13}, and V_2O_3. *Physical Review B, 41*, 4993-5009.

147. Ravindra, N.M., Weeks, R.A. & Kinser, D.L. (1987). Optical properties of GeO_2. *Physical Review B, 36*, 6132-6134.

148. Breckenridge, R.A., Robert W. Shaw, J. & Sher, A. (1974). Improved calculations of the complex dielectric constant of semiconductors. *Physical Review B, 10*, 2483-2489.

149. Grimes, R.D., Cowley, E.R. (1975). A Model Dielectric Function for Semiconductors. *Canadian Journal of Physics, 53*, 2549-2554.

150. Ravindra, N.M., Narayan, J. (1986). Optical properties of amorphous silicon and silicon dioxide. *Journal of Applied Physics, 60*, 1139 (8 pages).

151. Ravindra, N.M., Bhardwaj, R.P., Kumar, K.S. & Shrivastava, V.K. (1981). Model based studies of some optical and electronic properties of narrow and wide gap materials. *Infrared Physics, 21*, 369-381.

152. Kumar, A., Ravindra, N.M. (1982). Effective charges and ionicity in alkali halides: An analysis. *Physical Review B, 25*, 2889-2892.

153. Jackson, J.D. (1978). *Classical Electrodynamics*. New York: Wiley.

154. Ravindra, N.M., Ganapathy, P. & Choi, J. (2007). Energy gap–refractive index relations in semiconductors – An overview. *Infrared Physics & Technology, 50*, 21-29.

155. Goodenough, J.B. (1971). The two components of the crystallographic transition in VO_2. *Journal of Solid State Chemistry, 3*, 490-500.

156. Guo, Q., Kim, D.Y., Street, S.C. & Goodman, D.W. (1999). Ordered binary oxide films of V_2O_3 (0001) on Al_2O_3. *Journal of Vacuum Science & Technology A, 17*, 1887-1892.

157. Phillips, J.C. (1968). Dielectric Definition of Electronegativity. *Physical Review Letters, 20*, 550-553.

158. Rao, K.J., Pecquenard, B., Gies, A., Levasseur, A. & Etourneau, J. (2006). Structural and electrochemical behaviour of sputtered vanadium oxide films: oxygen non-stoichiometry and lithium ion sequestration. *Bulletin of Materials Science, 29*, 535-546.

159. Malati, M.A. (1999). *Experimental Inorganic/Physical Chemistry: An Investigative, Integrated Approach to Practical Project Work*. England: Woodhead Publishing.

160. Donnay, J.D.H. (1963). *Crystal data, determinative tables. Second Edition*. Buffalo: American Crystallographic Association.

161. A. S. Barker, J., Verleur, H.W. & Guggenheim, H.J. (1966). Infrared Optical Properties of Vanadium Dioxide Above and Below the Transition Temperature. *Physical Review Letters, 17*, 1286-1289.

162. Zhuze, V.P., Lukirskii, D.P. & Startsev, G.P. (1971). Reflectivity of the metallic phase of V_2O_3. *Soviet Physics - Solid State, 13*, 260-261.

163. Neuberger, M. (1971). *Data Compilation on Vanadium Oxides*. Culver City, California : Hughes Aircraft Company.

164. Kennedy, T.N., Hakim, R. & Mackenzie, J.D. (1967). Preparation and properties of crystalline and amorphous vanadium pentoxide. *Materials Research Bulletin, 2*, 193-201.

165. Kenny, N., Kannewurf, C.R. & Whitmore, D.H. (1966). Optical absorption coefficients of vanadium pentoxide single crystals. *Journal of Physics and Chemistry of Solids, 27*, 1237-1246.

166. Phillip, H.R., Ehrenreich, H. (1962). Optical Properties of Ag and Cu. *Physical Review, 128*, 1622-1629.

167. Smith, D.Y. (1985). *Handbook of Optical Constants of Solids*. Orlando, Florida: Academic Press.

168. Niklaus, F., Vieider, C. & Jakobsen, H. (2008). MEMS-based uncooled infrared bolometer arrays: a review. *Proceedings of SPIE, 6836*, 68360D (15 pages).

169. Rogalski, A. (2011). *Infrared detectors*. Boca Raton, Florida: CRC Press.

170. Naoum, J.A., Rahardjo, J., Taffese, Y., Chagny, M., Birdsley, J., Woo, J.C. & Morris, A. (2003). *Dynamic Infrared System Level Fault Isolation*. Santa Clara, California: ASM International.

171. Art, J. (2006). Photon Detectors for Confocal Microscopy. In: Pawley, J.B. (Ed.), *Handbook of Biological Confocal Microscopy*. New York: Springer.

172. Hyseni, G., Caka, N. & Hyseni, K. (2010). Infrared Thermal Detectors Parameters: Semiconductor Bolometers Versus Pyroelectrics. *WSEAS Transactions on Circuits and Systems, 9*, 238-247.

173. Stotlar, S.C. (2000). Infrared detector. In: Waynant, R., Ediger, M. (Eds.), *Electro-Optics Handbook*, pages 17.11-17.24. New York: McGraw-Hill.

174. Bhan, R.K., Saxena, R.S., Jalwania, C.R. & Lomash, S.K. (2009). Uncooled Infrared Microbolometer Arrays and their Characterisation Techniques. *Applied Optics, 59*, 580-589.

175. Yeh, P. (1988). *Optical waves in layered media*. New York: Wiley.

176. Hebb, J.P., Jensen, K.F. (1996). The Effect of Multilayer Patterns on Temperature Uniformity during Rapid Thermal Processing. *Journal of The Electrochemical Society, 143*, 1142-1151.

177. Howell, J.R., Siegel, R. & Menguc, M.P. (1992). *Thermal Radiation Heat Transfer*. Washington D. C.: Hemisphere Publishing Corporation.

178. Ravindra, N.M., Ravindra, K., Mahendra, S., Sopori, B. & Fiory, A.T. (2003). Modeling and simulation of emissivity of silicon-related materials and structures. *Journal of Electronic Materials, 32*, 1052-1058.

179. Hebb, J. (1997). *Pattern Effects in Rapid Thermal Processing*. Massachusetts Institute of Technology, Cambridge.

180. Rogalski, A. (2003). Infrared detectors: status and trends. *Progress in Quantum Electronics, 27*, 59-210.

181. Fieldhouse, N., Pursel, S.M., Horn, M.W. & Bharadwaja, S.S.N. (2009). Electrical properties of vanadium oxide thin films for bolometer applications: processed by pulse dc sputtering. *Journal of Physics D: Applied Physics, 42*, 055408 (6 pages).

182. Melnik, V., Khatsevych, I., Kladko, V., Kuchuk, A., Nikirin, V. & Romanyuk, B. (2012). Low-temperature method for thermochromic high ordered VO_2 phase formation. *Materials Letters, 68*, 215-217.

183. Lamsal, C., Ravindra, N.M. (2014). Simulation of spectral emissivity of vanadium oxides (VO_x)-based microbolometer structures. *Emerging Materials Research, 3,* 194-202.

184. http://refractiveindex.info/?group=METALS&material=Aluminium. (accessed on 11/20/2013).

185. Partlow, D.P., Gurkovich, S.R., Radford, K.C. & Denes, L.J. (1991). Switchable vanadium oxide films by a sol-gel process. *Journal of Applied Physics, 70,* 443-452.

186. Folks, W.R., Ginn, J., Shelton, D., Tharp, J. & Boreman, G. (2008). Spectroscopic ellipsometry of materials for infrared micro-device fabrication. *Physica Status Solidi C, 5,* 1113-1116.

187. Rogalski, A. (2002). Comparison of photon and thermal detector performance. In: Henini, M., Razeghi, M. (Eds.), *Handbook of Infra-red Detection Technologies*, pages 5-81. New York: Elsevier Science Inc.

188. http://www.semiwafer.com/products/silicon.htm. (accessed on 11/19/2013).

189. Lamsal, C., Ravindra, N.M. (2013). Optical properties of Vanadium oxides-An Analysis. *Journal of Materials Science, 48,* 6341-6351.

190. Richwine, R., Balcerak, R., Rapach, C., Freyvogel, K. & Sood, A. (2006). A comprehensive model for bolometer element and uncooled array design and imaging sensor performance prediction. *Proceedings of SPIE, 6294*, 62940F (11 pages).